



























## Strong Lensing and Cluster Evolution (SLICE) with JWST: Early Results, Lens Models, and High-Redshift Detections

CATHERINE CERNY <sup>1</sup>, GUILLAUME MAHLER <sup>2</sup>, KEREN SHARON <sup>1</sup>, MATHILDE JAUZAC <sup>3,4,5,6</sup>, GOURAV KHULLAR <sup>7</sup>,  
BENJAMIN BEAUCHESNE <sup>8</sup>, JOSE M. DIEGO <sup>9</sup>, DAVID J. LAGATTUTA <sup>3,4</sup>, MARCEAU LIMOUSIN,<sup>10</sup>  
NENCY R. PATEL <sup>3,4</sup>, JOHAN RICHARD <sup>11</sup>, CARLA CORNIL-BAÏOTTO <sup>12</sup>, MICHAEL D. GLADDERS <sup>13,14</sup>,  
STEPHANE WERNER <sup>3,4</sup>, JESSICA E. DOPPEL <sup>3,4</sup>, BENJAMIN FLOYD <sup>15</sup>, ANTHONY H. GONZALEZ <sup>16</sup>,  
RICHARD J. MASSEY <sup>3,4</sup>, MIREIA MONTES <sup>17</sup>, MATTHEW B. BAYLISS <sup>18</sup>, LINDSEY E. BLEEM <sup>19,20</sup>,  
REBECCA E. A. CANNING <sup>15</sup>, ALASTAIR C. EDGE <sup>3,4</sup>, MICHAEL McDONALD <sup>21</sup>, PRIYAMVADA NATARAJAN <sup>22,23</sup>,  
ANTHONY A. STARK <sup>9</sup>,<sup>24</sup> AND RAVEN GASSIS <sup>18</sup>

<sup>1</sup>Department of Astronomy, University of Michigan 1085 South University Avenue Ann Arbor, MI 48109, USA

<sup>2</sup>STAR Institute, Quartier Agora - Allée du six Août, 19c B-4000 Liège, Belgium

<sup>3</sup>Centre for Extragalactic Astronomy, Department of Physics, Durham University, South Road, Durham DH1 3LE, UK

<sup>4</sup>Institute for Computational Cosmology, Durham University, South Road, Durham DH1 3LE, UK

<sup>5</sup>Astrophysics Research Centre, University of KwaZulu-Natal, Westville Campus, Durban 4041, South Africa

<sup>6</sup>School of Mathematics, Statistics & Computer Science, University of KwaZulu-Natal, Westville Campus, Durban 4041, South Africa

<sup>7</sup>Department of Astronomy, University of Washington, Physics-Astronomy Building, Box 351580, Seattle, WA 98195-1700, USA

<sup>8</sup>Institute of Physics, Laboratory of Astrophysics, Ecole Polytechnique Fédérale de Lausanne (EPFL), Observatoire de Sauverny, 1290 Versoix, Switzerland

<sup>9</sup>Instituto de Física de Cantabria (CSIC-UC). Avda. Los Castros s/n. 39005 Santander, Spain

<sup>10</sup>Aix Marseille Univ, CNRS, CNES, LAM, Marseille, France

<sup>11</sup>Univ Lyon, Univ Lyon1, ENS de Lyon, CNRS, Centre de Recherche Astrophysique de Lyon UMR5574, 69230 Saint-Genis-Laval, France

<sup>12</sup>Instituto de Física y Astronomía, Universidad de Valparaíso, Gran Bretaña 1111, Playa Ancha, Valparaíso 2360102, Chile

<sup>13</sup>Kavli Institute for Cosmological Physics, University of Chicago, 5640 South Ellis Avenue, Chicago, IL 60637, USA

<sup>14</sup>Department of Astronomy and Astrophysics, University of Chicago, 5640 South Ellis Avenue, Chicago, IL 60637, USA

<sup>15</sup>Institute of Cosmology and Gravitation, University of Portsmouth, Burnaby Road, Portsmouth PO1 3FX, UK

<sup>16</sup>Department of Astronomy, 211 Bryant Space Science Center, University of Florida, Gainesville, FL USA 32611-2055

<sup>17</sup>Institute of Space Sciences (ICE, CSIC), Campus UAB, Carrer de Can Magrans, s/n, 08193 Barcelona, Spain.

<sup>18</sup>Department of Physics, University of Cincinnati, Cincinnati, OH 45221, USA

<sup>19</sup>High-Energy Physics Division, Argonne National Laboratory, 9700 South Cass Avenue., Lemont, IL, 60439, USA

<sup>20</sup>Kavli Institute for Cosmological Physics, University of Chicago, 5640 South Ellis Avenue, Chicago, IL, 60637, USA

<sup>21</sup>Massachusetts Institute of Technology, 77 Massachusetts Ave, Cambridge, MA 02139, USA

<sup>22</sup>Department of Astronomy, Yale University, New Haven, CT 06511, USA

<sup>23</sup>Department of Physics, Yale University, New Haven, CT 06511, USA

<sup>24</sup>Center for Astrophysics — Harvard & Smithsonian, 60 Garden Street, Cambridge, MA 02138, USA

### ABSTRACT

We leverage JWST’s superb resolution to derive strong lensing mass maps of 14 clusters, spanning a redshift range of  $z \sim 0.25 - 1.06$  and a mass range of  $M_{500} \sim 2 - 12 \times 10^{14} M_{\odot}$ , from the Strong Lensing and Cluster Evolution (SLICE) JWST program. These clusters represent a small subsample of the first clusters observed in the SLICE program that are chosen based on the detection of new multiple image constraints in the SLICE-JWST NIRCcam/F150W2 and F322W2 imaging. These constraints include new lensed dusty galaxies and new substructures in previously identified lensed background galaxies. Four clusters have never been modeled before. For the remaining 10 clusters, we present updated models based on JWST and HST imaging and, where available, ground-based spectroscopy. We model the global mass profile for each cluster and report the mass enclosed within 200 and 500 kpc. We report the number of new systems identified in the JWST imaging, which in one cluster is as high as 19 new systems. The addition of new lensing systems and constraints from substructure clumps in lensed galaxies improves the ability of strong lensing models to accurately reproduce the interior mass distribution of each cluster. We also report the discovery of a candidate transient in a lensed

image of the galaxy cluster SPT-CL J0516-5755. All lens models and their associated products are available for download at the [Strong Lensing Cluster Atlas Data Base](#), which is hosted at Laboratoire d’Astrophysique de Marseille.

*Keywords:* Galaxy clusters; Strong gravitational lensing

## 1. INTRODUCTION

Clusters of galaxies are home to the largest gravitationally-bound concentrations of mass in the Universe. Their deep potentials make them well-suited to explore the co-evolution and the assembly history of their constituents: dark matter (DM), intracluster plasma (or intracluster gas), galaxies, and free-floating stars (also known as intracluster light).

The exact nature of dark matter, the elusive but vital component of the Universe’s total mass budget, is not yet understood. As it is yet to be directly detected, the uncertainty surrounding its nature has left space for several models to develop beyond the current cosmological concordance model of the Universe which considers cold DM,  $\Lambda$ -CDM (Weinberg et al. 2013; Abbott et al. 2018; Planck Collaboration et al. 2020; Perivolaropoulos & Skara 2022). Galaxy clusters are excellent laboratories in which to test these theories, and confront observations with model predictions for DM properties that are imprinted on the DM distribution, and its spatial correlation with baryonic mass. Doing so requires studying the mass distributions in galaxy clusters across cosmic time, which in turn requires high resolution mapping of the mass of galaxy clusters at different redshifts, mass ranges, and densities.

As dark and observable matter are inextricably linked, the evolution of the distribution of luminous matter across cosmic time can be used as an indirect probe of the evolution of structures and substructures of DM (Natarajan et al. 2017). Adding information from gravitational lensing, and strong lensing (SL) in particular, which relies on observations of background galaxies behind the cluster of interest, provides a more direct probe of the innermost parts of clusters as it measures the total (dark and baryonic) mass distribution at the smallest spatial scales (e.g. a few kiloparsecs in the cluster plane) in cluster cores (Natarajan et al. 2024).

The high resolution and sensitivity of space-based imaging with the Hubble Space Telescope (HST) revolutionized SL science (Kneib & Natarajan 2011). A prime example is the Hubble Frontier Fields program (Lotz et al. 2017), which, through investment of hundreds of HST orbits, ground- and space-based spectroscopy, and the entire SL community effort, brought cluster SL accuracy and precision to a new level (John-

son et al. 2014; Richard et al. 2014; Sharon & Johnson 2015; Jauzac et al. 2015; Diego et al. 2016; Limousin et al. 2016; Prieue et al. 2017; Meneghetti et al. 2017; Remolina González et al. 2018). Other cluster surveys with HST, as well as targeted observations of single clusters, demonstrated the power of SL to probe structures at different mass ranges, from the most massive clusters down to groups and even individual galaxies, and to use SL clusters as calibrated cosmic telescopes to magnify and study the Universe behind them (Zheng et al. 2012; Coe et al. 2013; Zitrin et al. 2014; Rigby et al. 2017; Salmon et al. 2018; Sharon et al. 2022).

SL science has taken yet another step forward in the era of JWST, owing to JWST’s sensitivity, wavelength coverage, and resolution at long wavelengths which enabled the discovery of new multiple images with remarkable precision (e.g., Furtak et al. 2022; Mahler et al. 2023). The increased number of constraints resulted in high-resolution mass estimates for galaxy clusters (Furtak et al. 2024). Results from the first years of strong-lensing-enhanced JWST observations remarkably showcase its utility in probing the mass distribution in foreground structures (Pascale et al. 2022; Furtak et al. 2023; Rihtaršič et al. 2024, SMACS+more), discover and study galaxies at the highest redshifts (Atek et al. 2023; Adamo et al. 2024; Bradač et al. 2024; Mowla et al. 2024), and probe star forming regions and stellar clumps at cosmic noon at spatial scales smaller than a hundred parsecs (Claeyssens et al. 2023; Forbes & Romanowsky 2023; Meena et al. 2023; Rivera-Thorsen et al. 2024; Claeyssens et al. 2025; Rigby et al. 2025).

In this paper, we introduce the Strong Lensing and Cluster Evolution program (SLICE; Mahler et al., in prep), a large Cycle-3 JWST SURVEY program (#PID: 5594, PI: Mahler) designed to track the evolution of both the luminous and dark components of galaxy clusters over 8 Gyrs of cosmic time from  $z \sim 0.2$  to  $z = 1.9$ . The program is obtaining NIRCcam imaging of targets drawn from a parent list of 182 clusters, selected primarily for their mass as determined from Sunyaev-Zel’dovich (SZ) effect and X-ray mass proxies, and has at the time of publication observed a total of 100 clusters.

Through observations of clusters selected by mass to be on the same evolutionary track, SLICE aims to study (1) the buildup of the stellar content in the brightest

cluster galaxies (BCGs) and the intra-cluster light; and (2) the distribution of DM in clusters. The unique sensitivity and resolution of JWST in the infrared reveals the old stellar populations, resolving numerous globular star clusters embedded in the intra-cluster light (e.g., [Diego et al. 2023a](#); [Martis et al. 2024](#)), in addition to tidal fronts and other structures in the intra-cluster light ([Montes & Trujillo 2022](#)). The mapping of DM is to be measured primarily via SL modeling, but can also be inferred in non-SL clusters from the distribution of globular clusters, which are good tracers of the underlying DM density ([Lee et al. 2010](#); [Ko et al. 2017](#)). The combination of these two science goals will reveal the co-evolution of luminous and dark matter in the densest nodes of the cosmic web. By design, the program benefits from ancillary imaging data from space (HST for all targets, X-ray for a subsample) and ground-based spectroscopy for many fields.

We present SL models of 14 clusters from SLICE, a first step in achieving the ultimate science goals of this program. These clusters were chosen from SL clusters observed in the first few months of SLICE observations, and span almost the entire range of redshifts, mass, and Einstein radii of the parent sample. Four clusters have never been modeled in the literature using SL techniques, while the remaining clusters have published lens models based on HST imaging and other available data. We thus take the opportunity to revisit and update these models with new constraints or new lensing substructure features that are newly identified in JWST. Most of the new constraints were not visible in HST imaging, either because they are too red (e.g., dusty or high redshift galaxies), or too faint to be robustly identified at the depth of the archival data. The models developed in this work will be made available to the community at (the [Strong Lensing Cluster Atlas Data Base](#)), hosted at Laboratoire d’Astrophysique de Marseille.

The paper is organized as follows. Section 2 presents the observations and data reduction of JWST and HST observations used to create the SL mass models, and Chandra X-ray imaging of some of the clusters, used for interpretation of the results. Section 3 presents the lens models for each cluster, and Section 4 details the findings for the number counts of the lensing features examined in this paper. In Section 5, we discuss how these models will be used in future SLICE analyses and introduce upcoming work that will be completed once the full SLICE sample has been observed.

We assume a standard  $\Lambda$ CDM cosmology with  $\Omega_M = 0.3$ ,  $\Omega_\Lambda = 0.7$ , and  $H_0 = 70 \text{ km s}^{-1} \text{ Mpc}^{-1}$ . All magnitudes are measured in the AB system unless stated otherwise.

## 2. OBSERVATIONS

### 2.1. JWST SLICE Imaging

The SLICE JWST SURVEY mode program (PID: 5594; PI: Mahler) consists of NIRCcam imaging using the filters F150W2 and F322W2, which are extra-wide filters in the short wavelength and long wavelength channel, respectively, and which together cover the wavelength range between 1 to 4 micrometers. The program is designed as a large survey with 182 possible targets, with 100 observed at the time of the publication of this paper. The observations are run in the Shallow 4 mode with only Module B active to reduce the volume of the data products that are downloaded from the spacecraft. An IntramoduleX 3 dithering pattern is employed to remove any chip gaps, and an additional 3 point dithering pattern is employed using small-grid-dither to improve PSF sampling at shorter wavelengths. The observing time is calculated such that a  $S/N \sim 3$  is achieved for a point source at 29 magnitude, which equates to an equivalent exposure time of 1836 s in both the F150W2 and the F322W2 bands. This exposure time is consistent across all images in the SLICE program. Both the F150W2 and the F322W2 bands are observed simultaneously. JWST observations for the clusters studied in this paper are presented in Table 1 along with basic information about each cluster, including their redshifts and a measurement for  $M_{500}$  that is drawn from various literature references, where  $M_{500}$  is defined as the mass within a radius of  $R_{500}$  that has an overdensity of 500 times the critical mass density of the universe at the cluster redshift.

We follow the procedure described in [Rigby et al. \(2023a\)](#) for NIRCcam data reduction (as used for the JWST ERS program TEMPLATES), which we describe briefly below. We use Level 1b products from MAST using an STScI-adapted custom Python script. For data reduction, we use scripts modified from the default JWST Version (v1.15.1) and the CRDS calibration reference data system pipeline mapping (CRDS, pmap) 1303. We process Level 2A data products to apply a custom de-stripping algorithm to correct for 1/f noise and jumps between amplifiers. A complete description of this algorithm will be provided in the forthcoming survey paper (Mahler et al., in prep). We then run the de-stripped images through the same modified pipeline, to generate Level 3 F150W2 and F322W2 dithered science-

**Table 1.** SLICE JWST Observations

| Name               | $\alpha$ (J2000) | $\delta$ (J2000) | $z$    | $M_{500}$ ( $10^{14} M_{\odot}$ ) | Obs. number | Obs. date  |
|--------------------|------------------|------------------|--------|-----------------------------------|-------------|------------|
| Abell 68           | 9.267227487      | 9.153556343      | 0.2546 | 5.76 <sup>c</sup>                 | 16          | 2024-11-26 |
| RXC J0232.2–4420   | 38.0701090       | -44.3541290      | 0.2836 | 11.30 <sup>a</sup>                | 24          | 2024-10-23 |
| SMACS J2031.8–4036 | 307.9669300      | -40.6197000      | 0.3416 | 9.44 <sup>a</sup>                 | 37          | 2024-10-14 |
| MACS J0027.8+2616  | 6.9662000        | 26.2742000       | 0.365  | 11.70 <sup>d</sup>                | 39          | 2024-08-21 |
| RXC J2211.7–0349   | 332.9307646      | -3.82922895      | 0.397  | 12.31 <sup>c</sup>                | 52          | 2024-11-18 |
| MACS J0553.4–3342  | 88.3512360       | -33.71225900     | 0.412  | 11.33 <sup>a</sup>                | 55          | 2024-10-30 |
| MACS J0358.8–2955  | 59.7201370       | -29.92988500     | 0.425  | 8.81 <sup>a</sup>                 | 58          | 2024-10-23 |
| MACS J1621.4+3810  | 245.3500000      | 38.16740000      | 0.4631 | 14.48 <sup>d</sup>                | 71          | 2024-08-19 |
| RCS2 032727–132623 | 51.8632708       | -13.43938060     | 0.564  | 5.53 <sup>b</sup>                 | 86          | 2024-09-30 |
| MACS J2129.4–0741  | 322.3544372      | -7.70892166      | 0.589  | 7.06 <sup>c</sup>                 | 89          | 2024-10-03 |
| PSZ1 G091.83+26.11 | 277.7835360      | 62.24809379      | 0.822  | 7.43 <sup>c</sup>                 | 118         | 2024-09-08 |
| RX J0152.7–1357    | 28.17764473      | -13.95911996     | 0.8269 | 3.47 <sup>b</sup>                 | 119         | 2024-08-26 |
| SPT-CL J0516–5755  | 79.2397540       | -57.91668800     | 0.9656 | 3.42 <sup>a</sup>                 | 139         | 2024-08-29 |
| SPT-CL J2011–5228  | 302.7786200      | -52.47247800     | 1.064  | 3.10 <sup>a</sup>                 | 149         | 2024-09-06 |

NOTE—Summary of JWST observations from the SLICE program (PID: 5594; PI: Mahler). The exposure time for all JWST images in both the NIRCcam/F150W2 and NIRCcam/F322W2 filters is 1836 seconds. The name of the cluster is given in the first column, and the R.A.,  $\alpha$ , and Decl.,  $\delta$ , are given in degrees in the second and third columns. The cluster redshift is listed in the fourth column. The  $M_{500}$  mass is given in column five and the superscript indicates the reference used in our cluster selection, as follows: <sup>a</sup> Bocquet et al. 2019, <sup>b</sup> Hilton et al. 2021, <sup>c</sup> Planck Collaboration et al. 2016a, <sup>d</sup> Repp & Ebeling 2018 converting the X-ray flux using Equation (2) from the formula presented in Anderson et al. 2015.  $M_{500}$  is defined as the mass within a radius of  $R_{500}$  that has an overdensity of 500 times the critical mass density of the universe at the cluster redshift. The SLICE program visit ID is listed in the sixth column, and the observation date for the exposure is given in the seventh column.

ready mosaics. The filters are WCS-matched to Gaia as per the specifications of the default pipeline; HST data are aligned to JWST imaging within uncertainties. For more details on the various steps and systematics involved in this process, please refer to the complete description provided in Rigby et al. (2023a).

## 2.2. HST Archival Imaging

Archival HST images for all the clusters presented in this paper were obtained from MAST. For SLICE targets that were previously observed as part of HST treasury programs (ReIonization Lensing Cluster Survey – RELICS, Coe et al. 2019; Cluster Lensing And Supernova survey with Hubble – CLASH, Postman et al. 2012), we used the reduced data that were made available to the community by these projects. For all other targets, we reduced the HST imaging data to match the footprint, pixel scale, and WCS solution of the new JWST data, using standard procedures as part of `Astrodrizzle`. We combined the calibrated sub-exposures taken with each filter (`_flt` for WFC3-IR, and `_flc` files for UVIS and ACS) using a Gaussian kernel with a drop size `final_pixfrac=0.8` and

`final_refimage` set to the NIRCcam F150W2 exposure. If needed, images were further aligned to better match the WCS solution of the NIRCcam data using `tweakreg` and `tweakback`. A complete list of the HST images used in this paper is presented in Table 2.

## 2.3. Chandra X-rays Imaging

We retrieved archival X-rays observations from the *Chandra X-rays Observatory* for a sub-sample of the clusters. These observations used the Advanced CCD Imaging Spectrometer (ACIS) and are composed of observations obtained with the ACIS-I or ACIS-S configuration. Due to the limited number of counts for specific clusters, we included data obtained in FAINT mode in addition to the more robust VFAINT one. We reduced the data with the routine implemented in the CIAO software environment (Fruscione et al. 2006, version 4.15). In particular, we used the WAVDETECT source-detection routine (Freeman et al. 2002) to automatically remove the X-ray point sources and create counts maps in the [0.5, 7] keV band from the diffuse X-ray emission. We additionally employ the `csmooth` routine, which is a *Chandra*-focused adaptation of the



**Table 2.** Archival HST Observations

| Name               | Band        | PID   | Program Type             | Exp. time [s] | Obs. date  |
|--------------------|-------------|-------|--------------------------|---------------|------------|
| Abell 68           | ACS/F814W   | 11591 | GO                       | 4880          | 2010-11-14 |
|                    | WFC3/F110W  | 11591 | GO                       | 2612          | 2010-10-18 |
|                    | WFC3/F160W  | 11591 | GO                       | 2412          | 2010-10-18 |
| RXC J0232.2–4420   | ACS/F606W   | 14096 | GO/Treasury <sup>1</sup> | 2075          | 2016-07-05 |
|                    | ACS/F606W   | 14096 | GO/Treasury <sup>1</sup> | 2075          | 2016-08-14 |
|                    | ACS/F814W   | 14096 | GO/Treasury <sup>1</sup> | 2246          | 2016-07-05 |
| SMACS J2031.8–4036 | ACS/F606W   | 12166 | SNAP                     | 1200          | 2010-09-17 |
|                    | ACS/F814W   | 12884 | SNAP                     | 1440          | 2012-11-14 |
|                    | WFC3/F110W  | 12166 | SNAP                     | 706           | 2012-06-21 |
|                    | WFC3/F140W  | 12166 | SNAP                     | 706           | 2012-06-21 |
| MACS J0027.8+2616  | ACS/F606W   | 12166 | SNAP                     | 1200          | 2010-10-02 |
|                    | ACS/F775W   | 9770  | GO                       | 14370         | 2004-01-17 |
| RXC J2211.7–0349   | ACS/F606W   | 12166 | SNAP                     | 1200          | 2011-11-19 |
|                    | ACS/F814W   | 14096 | GO/Treasury <sup>1</sup> | 2101          | 2015-11-25 |
| MACS J0553.4–3342  | ACS/F435W   | 12362 | GO                       | 4452          | 2012-01-05 |
|                    | ACS/F606W   | 12362 | GO                       | 2092          | 2012-01-05 |
|                    | ACS/F814W   | 12362 | GO                       | 4572          | 2012-01-05 |
| MACS J0358.8–2955  | ACS/F435W   | 12313 | GO                       | 4500          | 2011-02-19 |
|                    | ACS/F606W   | 12313 | GO                       | 2120          | 2011-02-19 |
|                    | ACS/F814W   | 12313 | GO                       | 4620          | 2011-02-19 |
| MACS J1621.4+3810  | ACS/F606W   | 12166 | SNAP                     | 1200          | 2011-07-21 |
|                    | ACS/F814W   | 12166 | SNAP                     | 1440          | 2012-09-08 |
|                    | WFC3/F110W  | 12884 | SNAP                     | 706           | 2012-10-12 |
|                    | WFC3/F140W  | 12884 | SNAP                     | 706           | 2012-10-12 |
| RCS2 032727–132623 | ACS/F814W   | 12371 | GO                       | 1080          | 2011-06-28 |
|                    | WFC3/F125W  | 12267 | GO                       | 862           | 2011-03-01 |
|                    | WFC3/F160W  | 12267 | GO                       | 862           | 2011-03-01 |
| MACS J2129.4–0741  | ACS/F606W   | 12100 | GO/Treasury <sup>2</sup> | 3728          | 2011-05-15 |
|                    | ACS/F814W   | 10493 | GO                       | 2168          | 2005-06-18 |
| PSZ1 G091.83+26.11 | ACS/F606W   | 15132 | SNAP                     | 1200          | 2018-08-27 |
|                    | ACS/F814W   | 14098 | SNAP                     | 1200          | 2016-07-24 |
| RX J0152.7–1357    | ACS/F625W   | 9290  | GTO/ACS                  | 4750          | 2002-11-10 |
|                    | ACS/F160W   | 14096 | GO/Treasury <sup>1</sup> | 1209          | 2017-11-26 |
| SPT-CL J0516–5755  | ACS/F606W   | 13412 | SNAP                     | 2320          | 2014-02-27 |
| SPT-CL J2011–5228  | UVIS1/F606W | 14630 | GO                       | 2690          | 2017-03-18 |
|                    | UVIS2/F606W | 14630 | GO                       | 2676          | 2017-03-22 |

NOTE—Summary of primary archival HST observations that were used in this work. The name of the cluster is given in the first column. The camera and filter are listed in the second column, the PID for each observation is given in the third column, followed by program type: General Observer (GO), Snapshot (SNAP), Large Treasury (GO/Treasury) and Guaranteed Time Observations allocated to the ACS team (GTO). Treasury programs are marked with a superscript 1, referring to RELICS (Coe et al. 2019), or superscript 2, referring to CLASH (Postman et al. 2012). Finally, the exposure time is given in the fifth column, and the observation date in the sixth column. The list is not exhaustive: more data are available in the archive for many of the fields.

**Table 3.** Archival *Chandra* Observations

| Cluster            | Obs. ID | Exp. time [ks] | Obs. date  |
|--------------------|---------|----------------|------------|
| RXCJ0232.2–4420    | 4993    | 23.40          | 2004-06-08 |
| MACS J0027.8+2616  | 3249    | 9.98           | 2002-06-26 |
|                    | 14012   | 21.69          | 2012-09-24 |
| MACS J0553.4–3342  | 5813    | 9.94           | 2005-01-08 |
|                    | 12244   | 74.06          | 2011-06-23 |
| MACS J0358.8–2955  | 11719   | 9.65           | 2009-19-18 |
|                    | 12300   | 29.66          | 2010-11-26 |
|                    | 13194   | 19.97          | 2010-11-28 |
| MACS J1621.4+3810  | 3254    | 9.85           | 2002-10-18 |
|                    | 3594    | 19.73          | 2003-08-22 |
|                    | 6109    | 37.55          | 2004-12-11 |
|                    | 6172    | 29.75          | 2004-12-25 |
|                    | 9379    | 29.91          | 2008-10-17 |
| MACS J2129.4–0741  | 10785   | 29.75          | 2008-10-18 |
|                    | 3199    | 19.86          | 2002-12-23 |
| PSZ1 G091.83+26.11 | 3595    | 19.87          | 2003-10-18 |
|                    | 18285   | 22.7           | 2016-06-19 |
| RX J0152.7-1357    | 914     | 36.48          | 2000-09-08 |
|                    | 21703   | 39.56          | 2019-09-25 |
|                    | 22856   | 19.28          | 2019-09-26 |

NOTE—Summary of archival *Chandra* X-ray observations, available only for 8 clusters.

ASMOOTH routine (Ebeling et al. 2006), to smooth the X-ray maps for the purpose of visual presentation. A complete list of the X-ray imaging used in this paper is given in Table 3.

### 3. STRONG LENSING MASS MODELING

In this section, we present strong lens models that are designed to recover the mass within the core of the observed galaxy clusters using the positions of multiply-imaged galaxies as constraints. These lens models are constructed primarily using *Lenstool* (Jullo et al. 2007), a parametric MCMC modeling software which is described in more detail below. We also present lens models created using the hybrid modeling technique *WSLAP+* (Diego et al. 2005, 2007) for the galaxy clusters RCS2 032727–132623 (hereafter RCS 0327) and PSZ1 G091.83+26.11, which each have a large amount of lensed substructure visible in the JWST imaging that enable the use of free-form methods like *WSLAP+*. We discuss the use of these two techniques in Section 3.4.9 and Section 3.4.11.

The parameters for the best-fit *Lenstool* models for each cluster are listed in Table 6. The properties of

all multiple image systems for each cluster in this section are listed in Table 7. A false-color image displaying the critical curves and multiple image systems for each cluster is shown in Figure 1.

Regardless of the algorithm used, all strong lens modeling techniques attempt to find a foreground mass distribution that satisfies the lens equation everywhere in the field, and reproduces the observed locations of multiple images of each background source. The multiple images are therefore used as constraints in the lens modeling process. Multiple images are identified in the imaging data, usually by eye, owing to their similarity to each other. Since lensing is wavelength-invariant, counter images should have the same colors (unless they are contaminated by foreground sources or obscured by dust). The morphology of two counter images should be the same, after accounting for their different distortions, magnifications, and parity. Finally, the parity (e.g., mirroring) should be consistent with expectation from strong lensing geometry. Spectroscopy may solidify the identification of arc candidates as counter-images of each other. In a few cases, multiple images of the same background source were identified spectroscopically in integral field unit (IFU) observations of the entire lensing field, such as VLT/MUSE (Bacon et al. 2010). These identifications may or may not have an optical counterpart at the depth of the JWST/HST imaging. The superior resolution of space-based imaging allows for identification and mapping of structure within multiple images, and mapping this substructure from one image to another. Substructure is most often in the form of emission clumps, but can also be distinct dust lanes, spiral arms, or other features. Where identified, the substructure can be used to increase the number of constraints. Table 7 tabulates the multiple images that were identified in each of the clusters presented in this paper. Where available, we list the spectroscopic, photometric or model-optimized redshift, and multiple clumps within each image.

#### 3.1. *Lenstool*

*Lenstool* is a parametric strong lens modeling algorithm, which uses MCMC formalism to explore the parameter space, identify the best fit set of parameters, and estimate statistical uncertainties on parameters and modeling outputs. We refer the reader to Jullo et al. (2007) for a full description of *Lenstool*. In short, the algorithm assumes that the foreground lens is comprised of a combination of mass halos, each described by a set of parameters. Some examples of parameterized mass halos include NFW, isothermal, and the most commonly used for clusters is the pseudo-isothermal el-

lensoidal mass distribution (dPIE; [Elíasdóttir et al. 2007](#), also referred to in the literature as PIEMD). Lensing constraints come from the positions and redshifts of sets of multiple images of the same lensed source. Where spectroscopic redshift is not available, one can leave the redshift as a free parameter. Photometric redshifts or other information can be used to guide the posterior. The goodness of fit criterion is the image-plane scatter between the observed and predicted images of lensed sources (image-plane minimization), or the source-plane scatter between sets of predicted source locations of the same system ([Jullo et al. 2007](#)). Unless otherwise noted, **Lenstool** models in this work assume the dPIE distribution, which has seven parameters: centroid  $x$ ,  $y$ ; ellipticity  $e$ ; position angle  $\theta$ ; core radius  $r_{core}$ ; cut radius  $r_{cut}$  and normalization  $\sigma_0$ . Clusters are typically represented with one or more cluster-scale halos, supplemented with a number of galaxy-scale halos. Most of the parameters of cluster-scale halos are allowed to vary, with the exception of the cut radius, which for clusters is far outside the projected radius where it can be constrained by the lensing observables. If fixing the cut radius, each cluster-scale halo adds six free parameters to the lens model. To keep the number of overall optimized parameters manageable, it is common to assume that galaxy-scale halos of cluster-member galaxies have similar locations, ellipticities, and position angles as the stellar mass distribution of the galaxies they represent, and that their mass and slope parameters can be linked to the luminosity of each galaxy through parameterized scaling relations. This scaling adds two free parameters to the model.

Lens modeling is typically done iteratively, starting with a simple lens model and the most obvious sets of multiple images. Preliminary lens models can be used to assist in the identification and confirmation of further lensed systems, which in turn are included as constraints in the next iteration. With more constraints, the complexity and flexibility of the model can be increased. The process continues until the model converges on a stable solution, where newly identified systems are reliably predicted by the model and/or adding complexity does not significantly improve the goodness of fit or change the model output that is being sought (e.g., projected mass density, magnification, time delay, etc.). Modeling choices such as the number of halos are continuously evaluated, especially when new evidence is obtained, such as newly measured spectroscopic redshifts.

### 3.2. WSLAP+

This code was first described in [Diego et al. \(2005\)](#) and later expanded in [Diego et al. \(2007\)](#) to include

weak lensing measurements as additional constraints. A further development is presented in [Sendra et al. \(2014\)](#) where the code migrated from its native free-form nature to a hybrid type of modeling where prominent cluster member galaxies are added into the lens model with a mass distribution that matches the observed light distribution.

WSLAP+ places Gaussians in a predetermined grid of positions in the lens plane. Each Gaussian contributes to the deflection field an amount that is proportional to its mass. This mass is optimized by the algorithm. A contribution from member galaxies is also pre-computed adopting a fiducial mass for them, that is later also optimized. A joint solution for the masses of the Gaussians, renormalization of the mass of the member galaxies, and unknown position of the lensed galaxies in the source plane is obtained by solving a system of linear equations.

$$\Phi = \Gamma X, \quad (1)$$

where  $\Phi$  is an array containing the observed positions of the arcs,  $\Gamma$  is a known matrix, and  $X$  is the vector with all the unknowns: masses in the Gaussian decomposition ( $M$ ), multiplicative factors for the fiducial mass of the member galaxies ( $C$ ), and source positions ( $\beta_x$  and  $\beta_y$ ). The solution is obtained using a quadratic programming optimization algorithm with the constraint  $X > 0$ ; we refer the reader to [Diego et al. \(2007\)](#) for full details on the optimization algorithm.

### 3.3. Selection of Cluster-Member Galaxies

Cluster-member galaxies were selected photometrically using the red-sequence technique [Gladders & Yee \(2000\)](#). We generated a photometry catalog with Source Extractor ([Bertin & Arnouts 1996a](#)) in two filters that bracket the  $4000\text{\AA}$  break feature in typical elliptical galaxies at the cluster redshift. Galaxies were identified as cluster members based on their color with respect to the red sequence in a color-magnitude diagram. Where available, we used spectroscopic information to refine the selection. In most clusters, we used archival HST data for both filters; the specific filter selection changes based on the availability of archival data and the cluster redshift (see cluster-by-cluster descriptions in [Section 3.4](#)). The exception is SPT-CL J0516–5755, for which only one archival HST filter is available. For this cluster, we used the F150W2 as the red filter, as the  $4000\text{\AA}$  break feature in this filter is comfortably red of F606W at the cluster redshift ( $z = 0.9656$ ).

### 3.4. Cluster Models

In the following sections, we present details for each of the 14 clusters modeled in this paper. Images of the clusters and the strong lensing constraints are shown in Figure 1. The cluster best-fit parameters for each of the potentials and parameters in the `Lenstool` models are given in Table 6, and the lensing constraints are described in Table 7.

In the description for the model of each cluster, the number of systems refers to the number of unique lensed sources. The number of images is the total number of multiple images, and is generally a sum of the number of multiple images of each system over all the systems in the field. Where clumps within a lensed source (e.g. Figure 2) are used to constrain the model, the number of SL constraints includes multiple images of the individual clumps. Otherwise, the number of SL constraints equals the number of images used in the model. Candidate systems and arcs are not included in the count if they were not used as lensing constraints, but are shown in the figures and tables for reference.

All the lens models presented here are publicly available at the Strong Lensing Cluster Atlas Data Base<sup>1</sup>, which contains mass maps (e.g. shear, convergence, amplification), as well as parameter files used for the lens modeling (e.g. lists of constraints, cluster member catalogs).

#### 3.4.1. *Abell 68*

Abell 68 (A68), located at  $z = 0.2546$ , is optimized with a total of 12 systems (36 images and 42 lensing constraints), where 5 systems have spectroscopic redshifts and 7 unknown redshifts are optimized within the model. A total of 206 cluster member galaxies are included in the model, and are fitted with a scaling relation optimizing 2 parameters. The model uses 4 potentials to optimize the mass of the cluster. The final model has an rms of  $0''.47$ , and the mass enclosed within 200 kpc and 500 kpc is  $\sim 1.50 \times 10^{14} M_{\odot}$  and  $\sim 4.59 \times 10^{14} M_{\odot}$ , respectively. We provide a detailed description of the cluster modeling in the following paragraph.

A68 contains a wealth of lensed galaxies that are scattered between the two ends of its bimodal light distribution. We update the model presented in Richard et al. (2007) by doubling the number of constraints present in the model (from 21 to 42), which we accomplish by confirming candidates from Richard et al. (2007), such as the candidate system C10 and the candidate lensing images C2c and C23c, which are designated in this paper as Systems #6 and #4, respectively. We add

a total of 9 new systems into the model. The resolution of the JWST imaging also reveals a great deal of substructure in the main lensed dusty galaxy in this cluster, which is here designated as System 1. We are able to identify at least two different multiply-imaged clumps within both the dual radial images and the third counter-image of this galaxy, which we incorporate into the model as constraints. This increases the total number of lensing constraints present within a single lensed image. We utilize the spectroscopic redshift measurements presented in Richard et al. (2007) for the five previously-identified systems in this model. Reproducing all of the lensing constraints across the breadth of the cluster requires the inclusion of three cluster-scale dark matter halos into the model: one located at the BCG, one located in the northern portion of the cluster, and one located near the second-brightest galaxy in the cluster. We also separately optimize the parameters of the galaxy located next to the first image of System #1, as well as the BCG. The model redshift predictions for the sources used as constraints in the model are under  $z \sim 4$  in all cases, save for System #7, which has a best-fit optimized redshift of  $5.890_{-0.68}^{+0.01}$ . A complete list of the arcs and model redshifts is given in Table 7.

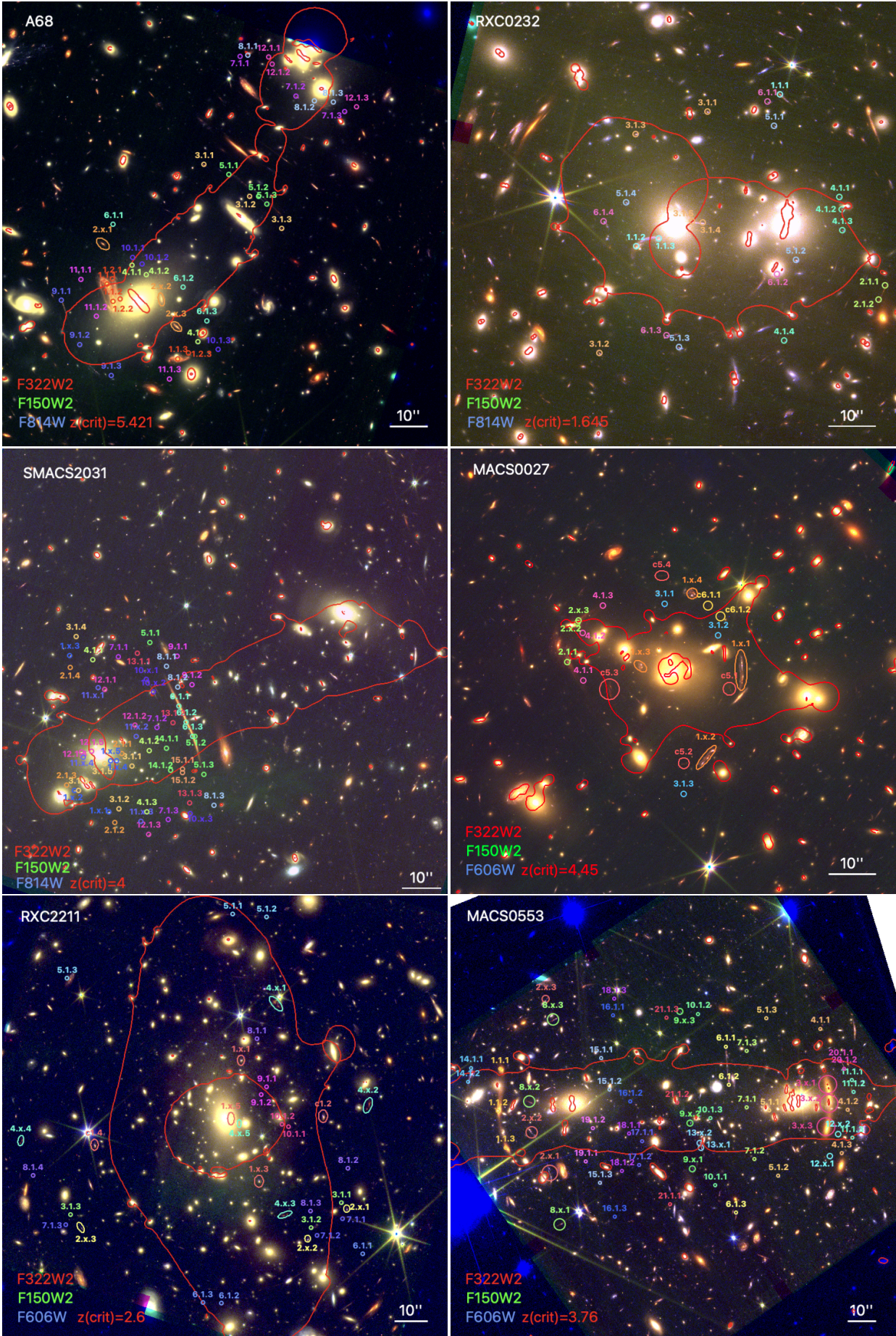
#### 3.4.2. *RXC J0232.2–4420*

RXC J0232.2–4420 (RXC0232), located at  $z = 0.2836$ , is optimized with a total of 7 systems (26 multiple images and 26 lensing constraints), where 2 systems have spectroscopic redshifts and 5 redshifts are optimized within the model. A total of 115 cluster member galaxies are included in the model, and are fitted with a scaling relation optimizing 2 parameters. The model uses 5 potentials to describe the mass of the cluster. The final model has an rms of  $0''.40$ , and the mass enclosed within 200 kpc and 500 kpc is  $\sim 1.85 \times 10^{14} M_{\odot}$  and  $\sim 4.51 \times 10^{14} M_{\odot}$ , respectively. We provide a detailed description of the cluster modeling in the following paragraph.

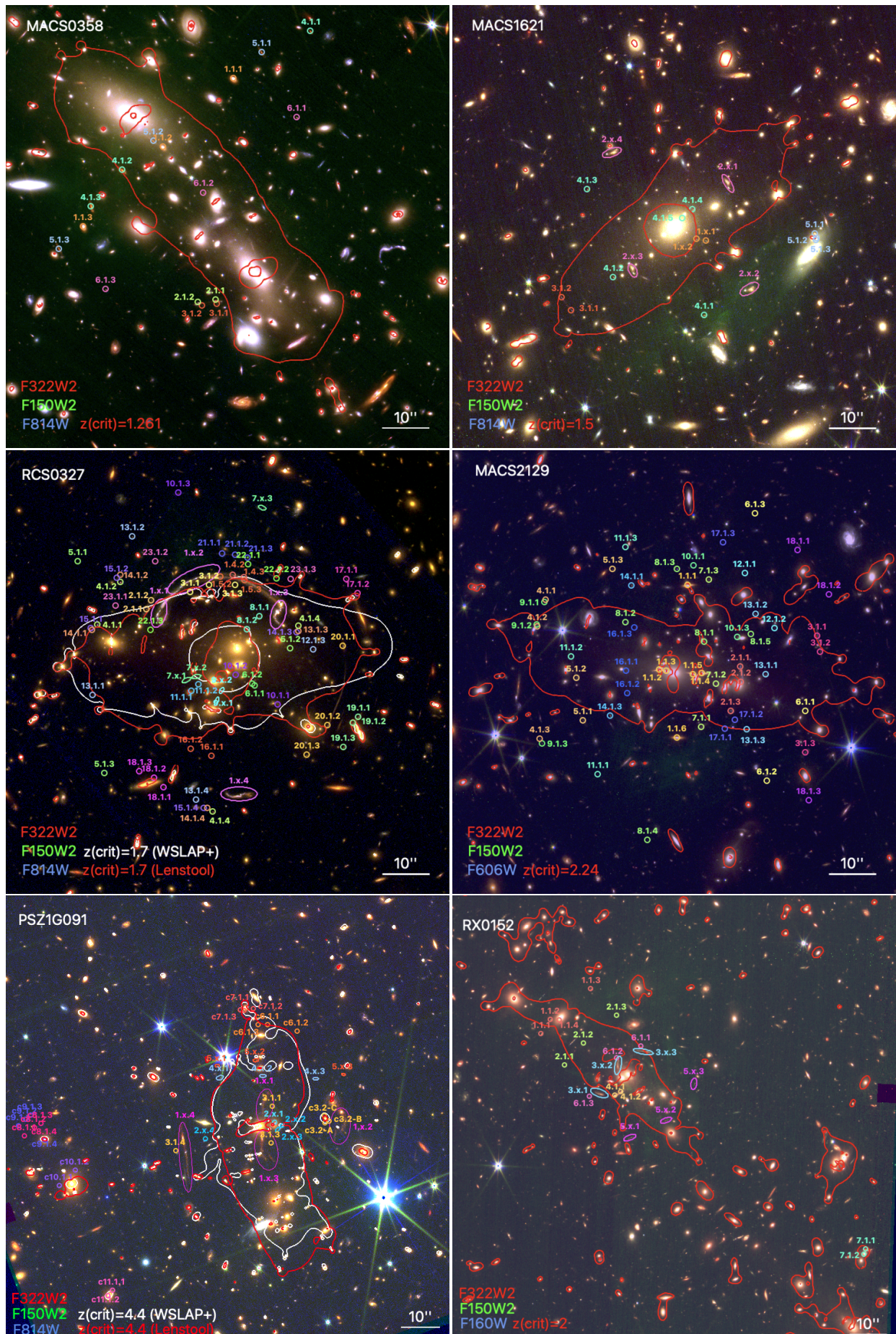
RXC0232, part of the RELICS cluster program (Coe et al. 2019), displays a bimodal light distribution with two BCGs (BCG<sub>A</sub> and BCG<sub>B</sub>) separated by  $24''$  along the East-West direction. Both the X-rays and radio contours are centered on BCG<sub>A</sub> in the East (Kale et al. 2019). We report six multiply imaged systems around these two BCGs (two radial systems), one of them being at a spectroscopic redshift  $z_{spec} = 1.645$  (Mainali 2019). We report one system at a spectroscopic redshift  $z_{spec} = 1.467$  (Mainali 2019) located further East, just outside the JWST field of view but observed thanks to the HST imaging. It is located around a group of three galaxies. The mass model includes two large scale

<sup>1</sup> The Strong Lensing Cluster Atlas Data Base is hosted at Laboratoire d’Astrophysique de Marseille.

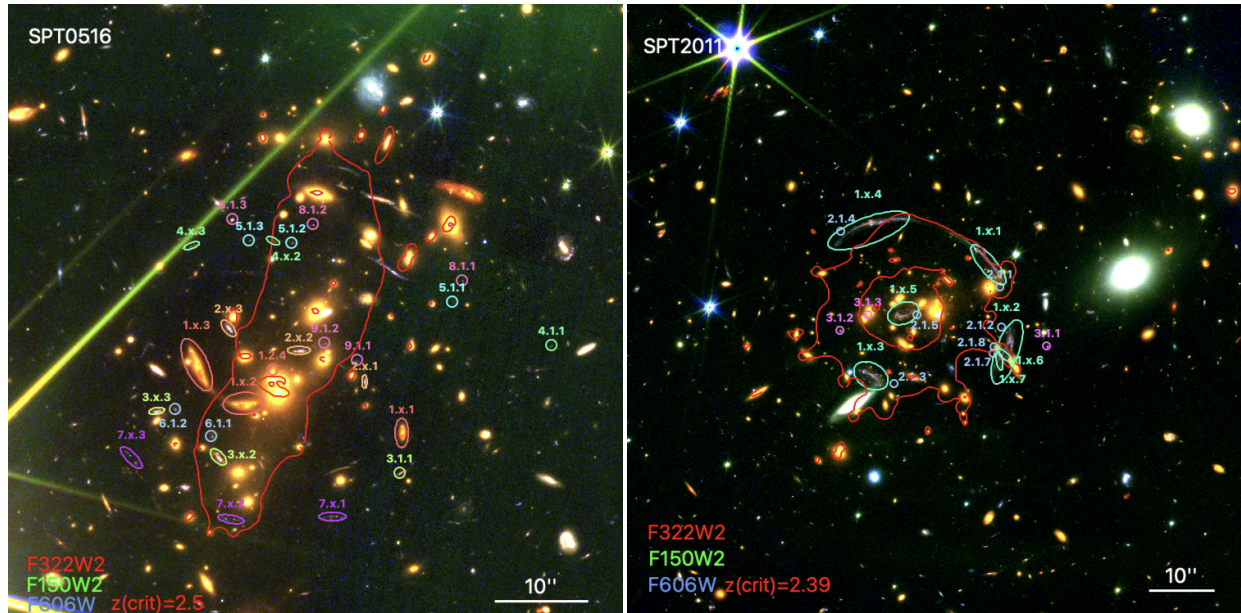


Figure 1. *continued*



Figure 1. *continued*





**Figure 1.** False color images of all clusters modeled in this paper. All images are oriented North up and East to the left. The color composites are rendered from the two JWST-SLICE NIRCcam bands, and one of the available archival HST bands in the blue channel as listed in the bottom left of each panel. We overplot the best-fit critical curves for a source at the redshift listed in each panel. Lens models constructed with `Lenstool` have their critical curves plotted in red, while lens models constructed with `WSLAP+` have their critical curves plotted in white. Sets of multiple images of lensed sources are color-coded and labeled. To reduce clutter, we label crowded individual clumps as ‘[System#].x.[Image#]’, where x refers to the clumps. Where applicable, candidate systems are labeled using the letter c, e.g. c1.1.1 indicates a candidate multiple image system that is not included in the optimization of the lens model. Two systems in PSZ1 G091.83+26.11 are outside the field of view, but are included in the model. See [Table 7](#) for a complete list of all the images and clumps for the systems in each cluster.

DM halos coincident with each BCG. The two BCGs are also optimized individually. A group scale DM halo is included as well to include the Eastern galaxy group. The central peak of the X-ray imaging is aligned with the center of the mass peak of the cluster (see [Table 3](#) for the X-ray observation details and [Figure 5](#) for the X-ray contours in cyan and projected mass contours in black). The model optimizes the fits for the redshifts of 5 systems. The best-fit optimization of the redshift for System #2 is  $5.902^{+0.06}_{-1.07}$ , while the other four systems have optimized redshifts under  $z \sim 3$ . A complete list of the arcs and model redshifts is given in [Table 7](#).

### 3.4.3. *SMACS J2031.8–4036*

SMACS J2031.8–4036 (SMACS2031), located at  $z = 0.3416$ , is optimized with a total of 15 systems (53 multiple images and 67 lensing constraints), where 13 systems have spectroscopic redshifts and 2 redshifts are optimized within the model. A total of 165 cluster member galaxies are included in the model, and are fitted with a scaling relation optimizing 2 parameters. The model uses 3 potentials to describe the mass of the cluster. The final model has an rms of  $0''.40$ , and the mass enclosed within 200 kpc and 500 kpc is  $\sim 1.38 \times 10^{14} M_{\odot}$

and  $\sim 4.47 \times 10^{14} M_{\odot}$ , respectively. We provide a detailed description of the cluster modeling in the following paragraphs.

The SLICE model of SMACS2031 is based on (and updates) the model presented in [Richard et al. \(2021\)](#) as part of the MUSE Cluster Atlas, a project targeting massive galaxy clusters with a combination of MUSE spectroscopy and HST imaging. Based on the HST data, SMACS2031 appears to be undergoing a major merger, with two distinct BCGs separated by  $72''$ . The apparent merger axis is oriented at a position angle of 60 degrees West of North. As a Cluster Atlas member, SMACS2031 has significant spectroscopic coverage, though only over its Eastern half, as the Western portion was not targeted by the survey. The [Richard et al. \(2021\)](#) model identified 13 multiply-imaged sources (consisting of 46 multiple images), however, due to the relatively shallow HST data, several of these systems are not detected in imaging, but only as emission line features in MUSE. In contrast, SLICE JWST imaging reveals clear continuum emission (in both F150W2 and F332W2) for all 13 systems, improving the centroiding precision of each image by up to  $\sim 0.5''$ . The improved resolution of JWST also reveals complex morphologies in many of



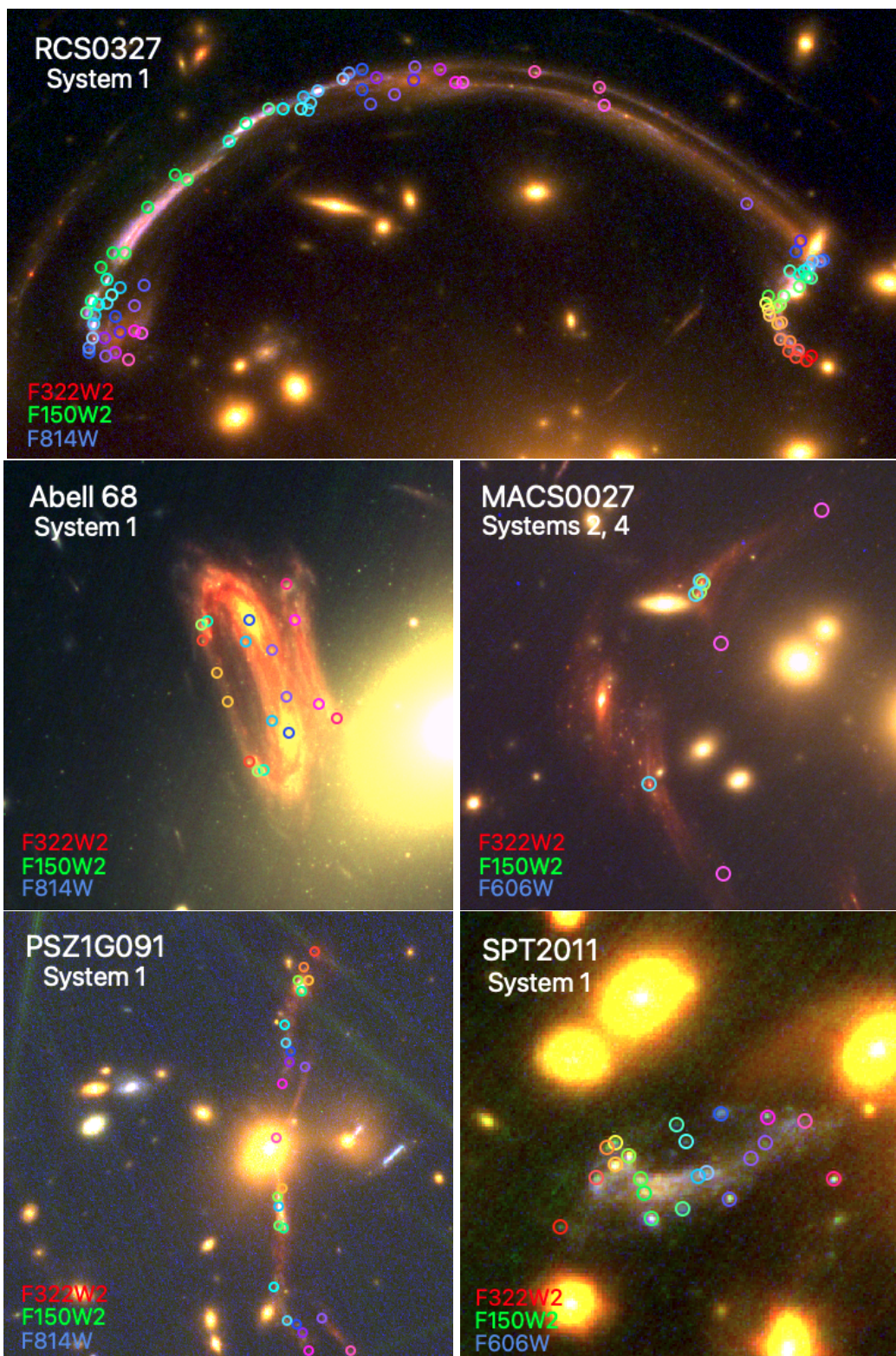


**Figure 2.** Snapshots of five lensed images from the SLICE program, including the primary tangential arc from System #1 in RCS0327 (top), System #1 in Abell 68 (middle left), Systems #2 and #4 from MACS0027 (middle right), System #1 in PSZ1G091 (bottom left), and the radial arc from System #1 in SPT2011 (bottom right). Constraints identified in the process of constructing the lens models are color-coded, but are not labeled for visual clarity. Some constraints shown in this figure include candidate clumps that were not used in the construction of the final lens model presented in this paper. Complete constraint information is provided in Table 7. The large number of identified emission knots in these lensed galaxies is possible due to the high-resolution infrared imaging capabilities of JWST. Each additional constraint imposes more precise limits on the modeled mass distribution of these clusters, increasing the potential of lens modeling to explore the fundamental properties of clusters.



the lensed systems, with Systems #1, #10, and #11 each having identifiable clumps in their continuum appearances, allowing us to use each of these clumps as a distinct model constraint.

In addition to confirming and updating the positions of existing lensed systems, we also identify two new, faint, arc-like objects (which we label as Systems #14 and #15) in the Eastern half of the cluster. Although we also detect several long, extended arc structures around the Western half of SMACS2031, these arcs have a distinctly smooth appearance with no obvious counter-images, making it difficult to know if they are merging pairs or simply distorted single-image galaxies. Therefore, at present we do not include any of the Western arcs as constraints, but this can be revisited with deeper imaging and/or spectroscopic follow-up.

Using these constraints, we construct a new lens model that includes three cluster and galaxy-scale mass halos in the model (see Table 6) – two to represent the cluster-scale halos of the Eastern and Western components of SMACS2031, and a third galaxy-scale halo to account for the Eastern BCG. Our model is then complemented with 165 smaller-scale halos to account for cluster member galaxies. We specifically model the Eastern BCG separately from other galaxies (see Section 3.1) because it lies close to individual lensed galaxies and could bias the fit.

After optimizing the model, we find a best-fit with a rms of  $0''.40$ . The best-fit position of the Eastern large-scale cluster halo is nearly colinear with the BCG, while the Western halo is offset by  $\sim 12''$  to the South (similar to the results of the Richard et al. 2021 model). However, the JWST imaging of the Eastern BCG reveals that the galaxy has a significant diffuse/shell-like appearance, suggesting that it has recently been disrupted, and possibly offering clues as to the nature of the cluster halo offset. The lack of constraints around the Western BCG make it difficult to obtain a proper centroid, which may also account for this offset. The model optimizes the redshifts of 2 systems, #14 and #15. The best-fit optimization of System #15 is  $6.893^{+0.08}_{-0.20}$ , while System #14 is under  $z \sim 2$ . A complete list of the arcs and model redshifts is given in Table 7.

#### 3.4.4. MACSJ0027.8+2616

MACSJ0027.8+2616 (MACS0027), located at  $z = 0.365$ , is optimized with a total of 4 systems (19 multiple images and 31 lensing constraints), where 2 systems have spectroscopic redshifts and 2 redshifts are optimized within the model. A total of 170 cluster member galaxies are included in the model, and are fitted with a scaling relation optimizing 2 parameters. The

model uses 1 potential to describe the mass of the cluster. The final model has an rms of  $0''.44$ , and the mass enclosed within 200 kpc and 500 kpc is  $\sim 1.73 \times 10^{14} M_{\odot}$  and  $\sim 5.09 \times 10^{14} M_{\odot}$ , respectively. We provide a detailed description of the cluster modeling in the following paragraphs.

We present here the first published lens model for MACS0027. The cluster was first reported in Repp & Ebeling (2018) as part of the HST SNAPshot surveys (PID: 12166; PI: Ebeling). We identify four multiple image systems, of which two systems have spectroscopic redshifts from MUSE. System #1 consists of four multiple images arranged in an Einstein-cross configuration, with a spectroscopic redshift measurement of  $z_{spec} = 3.127$ . MUSE also reveals a total of five images with a spectroscopic redshift of  $z_{spec} = 4.45$ . Inspection of the JWST imaging shows that three of these images share the same color and morphology, and are spatially arranged in a configuration consistent with expectations from lensing. We label these three images as System #3. The other two sources at this redshift do not share the morphology or colors of System #3, but according to the best-fit lens model, they may be counter-images of each other. We thus label these two sources as candidate System #7, though we do not use it in the lens model. The five MUSE sources are likely associated with two different galaxies at the same redshift, separated by  $\sim 30$  kpc in the source plane. We discuss these sources further in Section 4.4.

Systems #1 and #2 have a large amount of substructure that is only visible in the JWST imaging, and we use these substructure components as additional constraints in the model.

We visually identify a radial arc near the BCG, but do not associate it with any system due to the difficulty in securing a reliable spectroscopic redshift for it. We also identify two candidate systems, #5 and #6, as shown in Figure 1. For our final model, we only include Systems #1, #2, #3 and #4, while keeping Systems #5, #6 and #7 as candidates. We note that apart from these systems, there are several individually-lensed arcs found in JWST imaging that have no obvious counter images at the depth of the available data.

The central peak of the X-ray imaging is generally aligned with the center of the mass peak of the cluster (see Table 3 for the X-ray observation details and Figure 5 for the X-ray contours in cyan and projected mass contours in black). The model optimizes the fits for the redshifts of 2 systems. The best-fit optimization of the redshift for System #2 varies depending on the substructure clump used to perform the fit, where the first clump, #2.1, has an optimized model redshift of

$5.639_{-0.54}^{+0.21}$ , while the second clump, #2.2, has an optimized redshift of  $3.573_{-0.33}^{+1.71}$ . The second system, #4, has an optimized redshift of  $4.411_{-0.33}^{+0.17}$ . A complete list of the arcs and model redshifts is given in Table 7.

### 3.4.5. *RXC J2211.7–0349*

RXC J2211.7–0349 (RXC2211), located at  $z = 0.397$ , is optimized with a total of 10 systems (32 multiple images and 45 lensing constraints), where 1 system has a spectroscopic redshift and the remaining 9 redshifts are optimized within the model. A total of 197 cluster member galaxies are included in the model, and are fitted with a scaling relation optimizing 2 parameters. The model uses 5 potentials to describe the mass of the cluster. The final model has an rms of  $0''.80$ , and the mass enclosed within 200 kpc and 500 kpc is  $\sim 2.81 \times 10^{14} M_{\odot}$  and  $\sim 7.04 \times 10^{14} M_{\odot}$ , respectively. We provide a detailed description of the cluster modeling in the following paragraphs.

We update the lens model of RXC2211 that was first presented in Cerny et al. (2018), based on HST observations from the ReIonization Lensing Cluster Survey (RELICS; Coe et al. 2019). The original model consisted of three different multiple image systems, oriented mainly around the BCG of the cluster. The JWST-SLICE imaging allow us to add seven new multiple image systems to this model. The substructure in all ten systems of this model is clearly resolved, which allows us to use the clumps in five systems as additional constraints in the model.

Systems #1, #2, and #3 correspond to the identifications in Cerny et al. (2018). Systems #4, #5, #6, #7, #8, #9, and #10 are new identifications that are only visible in the JWST imaging. We use the spectroscopic redshift measurement of  $z_{spec} = 1.501$  from Cerny et al. (2018) for System #1, and allow the model to optimize the redshifts of the other constraints. System #4 has an optimized redshift of  $z \sim 5.4$ , while System #5 has an optimized redshift of  $5.750_{-0.41}^{+1.20}$ ; other optimized systems have redshifts of  $z \sim 3$ . Systems #9 and #10, which have an optimized model redshift of  $z \sim 2$ , are located very close to the critical curve, providing a tight constraint on its location. We also identify a candidate lensed galaxy, System #11, in the south-west part of the cluster, though we do not include it in the final model as its predicted configuration yields additional counter-images that cannot be reliably identified in the JWST imaging. System #4 is a very dusty red galaxy that is bright in the JWST imaging.

The new constraints give definition to the elongated, angularly-warped projected mass distribution, which is slightly tilted toward the west at both the north and

south ends. The complexity of the underlying mass distribution is reflected by the need for two large cluster-scale dark matter halos at the center of the cluster to accurately reproduce the positions of the multiple image systems. An additional two galaxy-scale cluster member halos are also placed near the second and seventh brightest galaxies in the cluster core to successfully reproduce the multiple images. Halo 3 adds a significant clump of mass to the west part of the cluster, indicating the presence of possible dark matter substructure. Further improvements to this model rely on the acquisition of more spectroscopic redshifts, especially for the new systems identified with JWST.

### 3.4.6. *MACS J0553.4–3342*

MACS J0553.4–3342 (MACS0553), located at  $z = 0.412$ , is optimized with a total of 21 systems (57 multiple images and 102 lensing constraints), where 4 systems have a spectroscopic redshift and the remaining 17 redshifts are optimized within the model. A total of 197 cluster member galaxies are included in the model, and are fitted with a scaling relation optimizing 2 parameters. The model uses 2 potentials to describe the mass of the cluster. The final model has an rms of  $0''.67$ , and the mass enclosed within 200 kpc and 500 kpc is  $\sim 1.84 \times 10^{14} M_{\odot}$  and  $\sim 6.14 \times 10^{14} M_{\odot}$ , respectively. We provide a detailed description of the cluster modeling in the following paragraphs.

We update the lens model that was originally presented in Ebeling et al. (2017) and used the HST observations from the ReIonization Lensing Cluster Survey (RELICS; Coe et al. 2019). The original model consisted of 10 different multiple image systems covering two main subclusters. The JWST-SLICE imaging allows us to add 11 new multiple image systems to this model. The substructure in 6 systems of this model is clearly resolved, which allows us to use a total of 102 clumps in the 21 systems as constraints in the model.

Systems #1 through #10 correspond to the identifications in Ebeling et al. (2017). Systems #11 through #21 are new identifications that are only fully confirmed using the JWST imaging. All systems are comprised of 3 images-folds. We use the spectroscopic redshift measurements of Systems #1 and #5, and make use of additional VLT/MUSE observations from the Kaleidoscope survey (PID: 0104.A-0801; PI: A. Edge) to confirm Lyman- $\alpha$  emission from Systems #5, #10 and #13. We let the model optimize the redshifts of the other systems.

The new constraints confirm the very elongated and strongly bimodal mass distribution of the previous model presented in Ebeling et al. (2017), and do not require additional complexity. The central peak of the

X-ray imaging is aligned with the western peak of the mass distribution, which contains a larger fraction of mass than the eastern portion of the cluster (see [Table 3](#) for the X-ray observation details and [Figure 5](#) for the X-ray contours in cyan and projected mass contours in black). The model optimizes the fits for the redshifts of 17 systems. System #6 has an optimized redshift of  $4.249_{-0.06}^{+0.07}$ , System #8 has a redshift of  $5.664_{-0.12}^{+0.15}$ , System #12 has a redshift of  $7.219_{-0.09}^{+0.27}$ , System #16 has a redshift of  $4.570_{-0.03}^{+0.04}$ , and the remaining systems are under  $z \sim 4$ . A complete list of the arcs and model redshifts is given in [Table 7](#).

#### 3.4.7. *MACS J0358.8–2955*

MACS J0358.8–2955 (MACS0358), located at  $z = 0.425$ , is optimized with a total of 6 systems (16 images and 16 lensing constraints), where 3 systems have a spectroscopic redshift and the remaining 3 redshifts are optimized within the model. A total of 256 cluster member galaxies are included in the model, and are fitted with a scaling relation optimizing 2 parameters. The model uses 2 potentials to describe the mass of the cluster. The final model has an rms of  $0''.21$ , and the mass enclosed within 200 kpc and 500 kpc is  $\sim 2.20 \times 10^{14} M_{\odot}$  and  $\sim 6.17 \times 10^{14} M_{\odot}$ , respectively. We provide a detailed description of the cluster modeling in the following paragraph.

MACS0358, a RELICS (Coe et al. 2019) cluster, displays a bimodal light distribution elongated in the North-East/South-West direction. A BCG is dominating the North-East light clump, whereas the South-West one is dominated by two galaxies with comparable magnitudes. Its 3D geometry and merger history have been investigated by Hsu et al. (2013), suggesting a complex merger of at least three sub-clusters. These authors constructed a mass model using 3 multiple image systems. We report here 6 multiple image systems, and adopt the spectroscopic redshift measurement of three of the sources from Hsu et al. (2013). The mass model is comprised of two large scale DM halos associated with each light concentration, on top of which we add 256 cluster members. The best-fit mass model has an rms of  $0''.21$  and our results are in agreement with the former model proposed by Hsu et al. (2013).

The peak of the X-ray imaging is located slightly south of the north-most peak of the mass model (see [Table 3](#) for the X-ray observation details and [Figure 5](#) for the X-ray contours in cyan and projected mass contours in black). The model optimizes the redshifts of 3 systems, all of which are under  $z \sim 3$ .

#### 3.4.8. *MACS J1621.4+3810*

MACS J1621.4+3810 (MACS1621), located at  $z = 0.4631$ , is optimized with a total of 5 systems (16 multiple images and 22 lensing constraints). None of the systems have a spectroscopic redshift at this time. One system (using two clumps) is fixed to its photometric redshift, and the remaining 4 source redshifts are optimized within the model. A total of 150 cluster member galaxies are included in the model, and are fitted with a scaling relation optimizing 2 parameters. The model uses 3 potentials to describe the mass of the cluster. The final model has an rms of  $0''.27$ , and the mass enclosed within 200 kpc and 500 kpc is  $\sim 1.62 \times 10^{14} M_{\odot}$  and  $\sim 3.91 \times 10^{14} M_{\odot}$ , respectively. We provide a detailed description of the cluster modeling in the following paragraphs.

We present a first lens model of the cluster MACS1621, whose discovery was initially reported in Repp & Ebeling (2018). We identified 5 multiple image systems in this field. Systems #1 and #2 are resolved in the JWST-SLICE imaging, with several clumps identified ([Figure 1](#)). The model uses two clumps as constraints for each of these two systems. We could not find any public spectroscopic record of the multiple image systems in this cluster. We thus rely on a photometric redshift measurement for the brightest image, System #2, estimated at  $z = 1.5_{-0.2}^{+0.3}$  using all available HST bands (ACS/F606W, ACS/F814W, WFC3IR/F110W, WFC3IR/F140W), to anchor the model and break mass-redshift degeneracies.

Using the aperture photometric apparent magnitudes (and Gaussian estimated uncertainties) from the arc/clump of interest in available HST and JWST filters, we conduct a Bayesian statistical inference to estimate photometric redshifts. We use the stellar population synthesis modeling package *Prospector* (Johnson et al. 2021) to simultaneously infer physical properties of the system along with its redshift. For our fiducial model, we use a parametric star formation history – delayed  $\tau$  – model, and fit stellar metallicity, dust attenuation (Calzetti et al. 2000), and total mass formed in the galaxy (with TopHat priors) as nuisance parameters (see Khullar et al. (2022) for details on the nominal fitting and modeling prescription used here).

We also note that the bluest photometry samples the Ly $\alpha$ /Ly $\beta$  emission region, and hence we fit an additional free parameter to marginalize the contribution of IGM absorption and Ly-series flux. The expectation from this process was that Lyman and Balmer breaks in galaxy/clump SEDs would allow us to put limits on redshifts, while simultaneously aiding the lens models. Equally importantly, with limited photometry for these sources, it is critical to simultaneously fit mul-

multiple galaxy parameters to respect the age-metallicity-dust degeneracy and the potential for the existence of multiple stellar populations (including emission-line producing stellar regions).

All other source redshifts are set as free parameters in the model. Although still limited by the lack of spectroscopic redshift constraints, the overall simple geometry of the cluster gives us enough confidence in our ability to accurately describe its shape. This assumption is supported by the overlap of the X-ray imaging peak with the projected surface mass density peak of the cluster (see Table 3 for the X-ray observation details and Figure 5 for the X-ray contours in cyan and projected mass contours in black). The model includes one cluster-scale potential, and the BCG is optimized separately. The BCG potential position is fixed to the center of the BCG, and its shape is free to vary. A third galaxy-scale potential at the cluster redshift is included to account for a foreground galaxy, in the proximity of System #5. The optimized redshifts for Systems #1-#4 are all below  $z \sim 4$ .

#### 3.4.9. RCS2 0327–1326

We present two lens models for RCS2 0327–1326 (RCS0327), located at  $z = 0.564$ , using two different algorithms: `Lenstool` and `WSLAP+`.

The field hosts a bright, highly magnified,  $\sim 38''$  giant arc of a  $z = 1.701$  galaxy that has been studied extensively (Sharon et al. 2012; Wuyts et al. 2014; Bordoloi et al. 2016; Lopez et al. 2018). The giant arc in the North of the field is composed of three partial images that merge at two critical curve crossings, and has a full counter image in the South. A fifth demagnified image was detected by Sharon et al. (2012)  $0''.6$  North of the BCG.

*Lenstool model*—We improve upon the HST+MUSE-based model that was used in Lopez et al. (2018) and later work. That model is based on and improve the Sharon et al. (2012) model by adding constraints from two lensed sources and three spectroscopic redshifts from MUSE to the previous model of Sharon et al. (2012). The JWST-SLICE imaging reveals or confirms 19 new lensed sources, including six new radial arcs to add to the one formerly known (Sharon et al. 2012). In addition, we identify and map 42 clumps in the multiple images of the giant arc. We adopt MUSE spectroscopic redshifts from Lopez et al. (2018) for System #7 (S7a/S7b in Sharon et al. 2012) at  $z_{spec} = 2.82624$ ; System #4 at  $z_{spec} = 2.73$ ; and System #5 at  $z_{spec} = 5.2$ . We discover a new radial arc in the MUSE data, labeled as System #6, with a bright Ly- $\alpha$  emission line and CIII placing this arc at  $z_{spec} = 3.518$ . A faint counter-

part appears in the JWST imaging at the same location; the counter image is predicted to be outside of the MUSE field of view. We use all the systems in Table 7 as constraints in the lens model. More arc candidates are visible in the data, and we leave their confirmation and possible use for further refining of the lens model to future work.

The `Lenstool` model optimizes seven DM halos, including two DM cluster-scale halos at the cluster core, one of which constrained to within  $2''$  of the BCG; three galaxy-scale halos—two cluster members within the West end of the giant arc, and one South of the giant arc—are allowed to be solved for separately from the scaling relations, as they are likely contributing a local shear effect on either end of the giant arc. Another small halo is positioned at the location of a small group of galaxies. Finally, a halo in the East is necessary in order to reproduce the faint arc (A in Sharon et al. 2012). The best-fit rms is  $0''.82$ . Due to the large number of constraints along the giant arc, and the equal weights assigned to all the constraints, the model is dominated by the constraints of the giant arc and is thus more tuned to producing accurate results in its vicinity, which could be at the expense of other regions in the field of view. The mass enclosed within 200 kpc and 500 kpc is  $\sim 2.07 \times 10^{14} M_{\odot}$  and  $\sim 5.14 \times 10^{14} M_{\odot}$ , respectively.

*WSLAP+ model*—The large number of knots available for System #1 enables the use of free-form methods such as `WSLAP+`, which require a large number of constraints to build functional models (see Section 3.2). The `WSLAP+` model is derived from the lensed galaxies in the `Lenstool` model described above that have a spectroscopic redshift; any constraints in the `Lenstool` model that do not have this measurement are not included in the `WSLAP+` model. The model contains  $536 + 1 + 2 \times 51$  free parameters. Out of these, 536 of them correspond to the Gaussian functions that are distributed on a multi-resolution grid (derived iteratively starting from a regular grid of  $20 \times 20$  Gaussians). One free parameter accounts for a renormalization factor to the mass of the member galaxies. The mass of these galaxies traces the observed light in the F150W2 filter and it is assumed as a fiducial mass that is later optimized by `WSLAP+`. Finally, the last  $2 \times 51$  free parameters correspond to the  $x$  and  $y$  positions in the source plane of the knots in System #1 and the other lensed galaxies used as constraints. The final solution is obtained after optimizing 200,000 steps ( $\approx 5$  minutes on a laptop), once convergence is achieved. The model contains  $\sim 2.02 \times 10^{14} M_{\odot}$  within 200 kpc from the center and  $\sim 5.34 \times 10^{14} M_{\odot}$  within 500 kpc from the center.



The `Lenstool` and `WSLAP+` models, which are constructed using a subset of the same constraints, result in similar overall mass distributions, particularly within the strong lensing region confined by the tangential critical curve. The difference between the models for both enclosed mass measurements is less than  $\sim 4\%$ . Nevertheless, minor differences between their resulting critical curves are observed (Figure 1). The discrepancy is smaller in regions that are well-constrained in both models, e.g., the critical curve crossing of the giant arc of System #1, which has numerous clumps, and near other arcs with spectroscopic redshift. Notably, while the east and west regions are relatively well constrained in the `Lenstool` model, the lack of spectroscopic redshifts leaves these regions relatively under-constrained for `WSLAP+`. A deep comparison between these two algorithms is beyond the scope of this paper and will be left to future work.

#### 3.4.10. *MACS J2129.4–0741*

MACS J2129.4–0741 (MACS2129), located at  $z = 0.589$ , is optimized with a total of 17 systems (53 multiple images and 53 lensing constraints), where 13 systems have a spectroscopic redshift confirmation (Zitrin et al. 2015; Caminha et al. 2019; Jauzac et al. 2021) and the remaining 4 systems redshifts are optimized within the model. The mass model includes 2 cluster-scale potentials to describe the overall mass distribution of the cluster. Adding to that, a total of 293 cluster member galaxies are fitted with a scaling relation (as described in Section 3.3) optimizing 2 parameters. Five cluster galaxies are also modeled independently due to their proximity to multiple images (all details can be found in Jauzac et al. 2021). Newly identified multiple images do not require the independent modeling of other cluster members. Our mass model is optimized using the `Lenstool` software (Jullo et al. 2007). The masses enclosed within 200 kpc and 500 kpc are  $\sim 1.84 \times 10^{14} M_{\odot}$  and  $\sim 5.32 \times 10^{14} M_{\odot}$ , respectively. We provide a detailed description of the cluster modeling in the following paragraph.

The model presented in this work is based on the model presented in Jauzac et al. (2021) and includes 3 newly identified multiple image systems from the SLICE-JWST imaging (Systems #16, #17 and #18). This elongated cluster presents one dominant elliptical cluster-scale potential. In addition, we relax the BCG potential and four other galaxy potentials near multiple image systems in this central region. One more group-scale potential in the North-West region of the cluster is added, matching the light distribution of an overdensity of bright cluster galaxies with diffuse emission. This

component is interpreted as an infalling group even if the X-ray imaging does not show a gaseous counterpart at the position of the galaxy group (see Table 3 for the X-ray observation details, and Figure 5 for the X-ray - cyan, and projected mass contours - black). Furthermore, we note that the gas peak in the X-ray distribution coincides with the main lensing mass peak which corresponds to the location of the BCG. This updated mass model is in excellent agreement with the model it is based on, with the rms of the SLICE best-fit mass model at  $0.79''$ , in comparison to  $0.80''$  for the Jauzac et al. (2021) best-fit model rms. The final model is optimizing the redshifts of Systems #5, #16, #17 and #18. System #18 has a best-fit optimized redshift of  $5.528_{-0.19}^{+0.47}$ . The other systems have optimized redshifts below 1.7 and, together with error bars, are all reported in Table 7.

#### 3.4.11. *PSZ1 G091.83+26.11*

We use two algorithms to construct preliminary lens models of PSZ1 G091.83+26.11 (PSZ1G09), located at  $z = 0.822$ . We identify in this field a total of 12 systems, of which five are considered secure systems of multiple images and the rest are candidates or galaxy-galaxy lensing features. There are no spectroscopic redshifts available for lensed galaxies in this field at the time of writing.

This is one of the most massive clusters known at  $z > 0.8$  (Planck Collaboration et al. 2016b) and hence deserves special attention. Clusters at this redshift are in an active phase of formation and often in a non-relaxed state. PSZ1G09 shows a bimodal structure both in Sunyaev-Zeldovich maps (Planck Collaboration et al. 2016b; Artis et al. 2022) as well as in the X-rays (Artis et al. 2022), thus suggesting an active merger. This interpretation is supported by radio observations that show prominent radio shock emission in the East side of the cluster (Di Gennaro et al. 2023). To date, no lens model is available in the literature. The JWST observations show a very large galaxy imaged into 4 counter images (System #1). This galaxy has two components, a blue and compact nucleus that is already clearly visible in earlier observations with HST, and a very red extended tail that is barely detectable in previous HST observations, but that is very prominent in F322W2 and possibly harboring copious amounts of dust. This type of blue-red pairs has been observed multiple times with JWST, often corresponding to interacting galaxies at  $z > 3$  (Diego et al. 2023b). Combining HST and JWST photometry, we derive photometric redshifts (as outlined in Section 3.4.8) for all 4 images of System #1 finding the redshift of the two most reliable images to be 4.39

and 4.44. We adopt a redshift of  $z_{phot} = 4.4$  for this system. In the new JWST data we identify 10 additional system candidates. For System #2, composed of two radial arcs and a tangential arc, we derive a photometric redshift of  $z_{phot} = 2.8$ . All the remaining systems lack reliable photometric redshift estimates since they are too faint to be detected in HST observations. Only the multiple image systems with redshift estimates can be used as constraints in the WSLAP+ algorithm.

To provide sufficient constraining power in the East, the WSLAP+ model assumes a redshift  $z \sim 3$  for a third system, System #8. The Lenstool model can use systems without a redshift estimate as constraints by including the redshift as a free parameter to be solved by the model. The Lenstool model uses the secure arcs as constraints. We describe the two models below.

**WSLAP+ model**—We model PSZ1G09 with the hybrid algorithm WSLAP+. We divide the member galaxies in two layers, with the BCG in layer 1 and all the remaining members in layer 2. The smooth component is modeled by a combination of Gaussian functions. A first model is derived on a grid of  $20 \times 20$  points, with a Gaussian centered on each grid point. This solution is used to construct a new grid for the Gaussian centers where more Gaussians (with smaller full-width at half maximums (FWHMs)) are placed in the regions with more mass. The new grid lowers the number of Gaussians (from 400 to 267), and increases the resolution near the regions of higher density. The number of free parameters in the model is then  $267 + 2 + 2 \times 11 = 291$  (267 Gaussians, 2 layers, and the positions in the source plane of 11 lensed galaxies). The bimodal structure of this cluster is evident in both the X-ray imaging and the projected surface mass density map. The X-ray peak is located around the middle of the two mass peaks, lending further evidence to the cluster’s status as an active merger (see Table 3 for the X-ray observation details and Figure 5 for the X-ray contours in cyan and projected mass contours in black). The model has an rms of  $1''.06$ . The mass enclosed within 200 kpc and 500 kpc is  $\sim 1.80 \times 10^{14} M_{\odot}$  and  $\sim 6.30 \times 10^{14} M_{\odot}$ , respectively.

We compute a second WSLAP+ model to explore a secondary mass distribution in the East, using the candidate system #8 as constraint with an assumed redshift of  $z \sim 3$ . From this model, the mass enclosed within 200 kpc and 500 kpc is  $\sim 1.84 \times 10^{14} M_{\odot}$  and  $\sim 7.05 \times 10^{14} M_{\odot}$ , respectively.

**Lenstool model**—The Lenstool model of PSZ1G09 uses the same constraints as the WSLAP+ model for Systems #1 and #2. Since Lenstool can include systems without photometric redshifts as constraints with free red-

shift parameters, we are able to use System #3 to constrain the cluster center, and Systems #4 and #5 to constrain the north part of the cluster core. We used an iterative modeling approach, starting with a lens plane composed of red-sequence-selected cluster-member galaxies and a single cluster-scale halo with broad priors. As expected from the arc geometry of the images of System #1, a single halo model resulted in a poor solution. We iteratively added cluster-scale halos, increasing the model complexity, until no significant improvement was recorded. The best-fit model converged on three cluster-scale halos; two near the main strong lensing core, and one east of the main strong lensing core. The slope and normalization parameters of the east halo were allowed to vary, but its position was fixed to the location of the brightest cluster galaxy,  $\sim 50''$  east of the main strong lensing core, at R.A., Decl. = [277.816360, 62.245004], and we assumed a circular mass distribution. The arc candidates near this halo were not used as constraints in the Lenstool model. We additionally freed some of the parameters of the two galaxies near the radial arcs of System #2, to increase the model flexibility at the center (see Table 6). The best-fit model has an image-plane rms of  $0''.47$ . The mass enclosed within 200 kpc and 500 kpc is  $\sim 1.89 \times 10^{14} M_{\odot}$  and  $\sim 7.61 \times 10^{14} M_{\odot}$ , respectively. It uses 5 systems as strong lensing constraints: System #1 at  $z_{phot} = 4.4$  with four images, each with 18 clumps; System #2 at  $z_{phot} = 2.8$  with five images; Systems #4 (2 clumps) and #5 (3 clumps) with three images each and unknown redshifts; and System #3, which has three secure images at an unknown redshift. The fourth is left as a candidate and not used as constraint since there is more than one possible arc near the location predicted by the lens model from the other three images. Acquiring a reliable redshift measurement (i.e. a spectroscopic measurement) for this system would likely allow the model to identify the correct counter-image from the three possible candidate images.

Figure 1 shows the critical curves of the WSLAP+ model (white) and Lenstool model (black) for a source at  $z = 4.4$ . Although using very different approaches, the two models yield similar critical curves, with the main discrepancies occurring in regions with less constraints. An examination of the mass measurements between the two modeling methods shows that the WSLAP+ model created with the same constraints as Lenstool measures a mass that is  $\sim 5\%$  lower than the Lenstool model within 200 kpc and  $\sim 19\%$  lower within 500 kpc. This difference originates from the lack of reliable constraints in the Eastern half of the cluster. The Lenstool model chooses to place a parametric halo fixed to the BCG of this portion of the cluster, while the WSLAP+ model

created with the same constraints as `Lenstool` cannot constrain a mass halo in this region, and thus does not include one. The second `WSLAP+` model, which is created with different constraints than the `Lenstool` model, elects to place a free-form mass halo around the location of candidate Systems #8 and #9. The agreement between this second model and the `Lenstool` model at 500 kpc is better, with only a  $\sim 9\%$  difference between the two models. This comparison highlights the importance of the Eastern mass component of this cluster in constraining the model. The acquisition of at least one spectroscopic redshift will enable both modeling methods to explore the parameter space in this region more rigorously.

#### 3.4.12. *RX J0152.7–1357*

RX J0152.7–1357 (RX0152), located at  $z = 0.8269$ , is optimized with a total of 9 systems (19 multiple images and 31 lensing constraints), where 1 system has a spectroscopic redshift and the remaining 8 redshifts are optimized within the model. A total of 131 cluster member galaxies are included in the model, and are fitted with a scaling relation optimizing 2 parameters. The model uses 1 cluster-scale potential to describe the mass of the cluster. The final model has an rms of  $0''.45$ , and the mass enclosed within 200 kpc and 500 kpc is  $\sim 1.14 \times 10^{14} M_{\odot}$  and  $\sim 3.44 \times 10^{14} M_{\odot}$ , respectively. We provide a detailed description of the cluster modeling in the following paragraphs.

In this work, we present a new mass model of RX0152 based on the SLICE JWST imaging. This cluster presents three overdensities of galaxies, highlighting a dominant cluster-scale halo and two group-scale halos in the South-West and West of the cluster. These three structures are apparent in the X-ray emission as highlighted by the contours of the X-ray surface brightness in Figure 5. These structures were already reported by a previous lensing analysis presented in Acebron et al. (2019).

Thanks to the new JWST imaging, we identify one new multiple image system located near a cluster member overdensity, South-West of the cluster. This system is barely visible in the reddest band of the RELICS imaging (i.e. WFC3/F160W). It appears clearly in the JWST/F322W2 band as a galaxy-scale lensing feature where only a part of the galaxy disk is multiply imaged. The color and the apparent size of the singly lensed body of the galaxy likely highlight a dusty galaxy at  $z \gtrsim 2$ . We confirm morphologically the six multiply-imaged galaxies used as constrain in Acebron et al. (2019). We could secure more accurate positions of the multiple images thanks to star-forming regions clearly

appearing in the JWST imaging. Two of the lensed galaxies show more than one clump; in total we therefore have 9 systems of multiple images as lensing constraints for our mass model.

Our `Lenstool` model includes 131 halos to account for the cluster members that we identified with a red sequence fitting based on the HST imaging in the ACS/F625W and WFC3/F160W bands. Based on this selection, we measure their position, position angle and ellipticity based on the JWST/F322W2 band. In addition, we add one cluster-scale halo to represent the smooth DM component of the main cluster. We try to add another halo in the South-West to account for the galaxy-group mentioned earlier, but the lack of multiple image systems in this regions leads to an unrealistic mass of this component. Unfortunately, only half of the structure is visible in JWST imaging, limiting our ability to identify new multiply imaged candidates.

Our model is similar to the `Lenstool` model presented in Acebron et al. (2019) in its parameterization, one cluster-scale DM halo and the cluster galaxy-scale components. However, we are not modeling any galaxy outside of the cluster member relation. Indeed, in Acebron et al. (2019), they model one cluster galaxy individually due to its proximity to a multiple image system, System #1. Using the same multiple image system as Acebron et al. (2019), our best-fit model has an RMS of  $0.47''$ , a slightly lower value than the rms of  $0.52''$  reported by Acebron et al. (2019). When including the newly identified multiple image system presented earlier, our best-fit mass model has an rms of  $0.45''$ .

#### 3.4.13. *SPT-CL J0516–5755*

SPT-CL J0516–5755 (SPT0516), located at  $z = 0.9656$ , is optimized with a total of 10 systems (25 multiple images and 53 lensing constraints), where the model is anchored using a photometric redshift estimate for 1 system and the remaining 9 systems are optimized within the model. A total of 247 cluster member galaxies are included in the model, and are fitted with a scaling relation optimizing 2 parameters. The model uses 3 potentials to describe the mass of the cluster. The final model has an rms of  $0''.22$ , and the mass enclosed within 200 kpc and 500 kpc is  $\sim 1.27 \times 10^{14} M_{\odot}$  and  $\sim 3.84 \times 10^{14} M_{\odot}$ , respectively. We provide a detailed description of the cluster modeling in the following paragraphs.

We present the first strong lens model of SPT0516. Archival HST data exist only in F606W for this field. We select cluster-member galaxies by their color in ACS/F606W-NIRCam/F150W2, and magnitudes as measured from the NIRCam/F150W2 band. We iden-

tify 10 lensed sources with high confidence to be used as lensing constraints. The elongated projected mass distribution results in naked cusp lensing configuration for virtually all the systems, with three images of each source. We only identify a central fourth image for System #1, near a cluster member at the cluster core. The most prominent system in the JWST-SLICE imaging is entirely absent from the HST/F606W data – a red dusty galaxy with distinct morphology and obvious dust lane. Interestingly, the Eastern image of this galaxy features an emission clump that is missing from the other images. We discuss this candidate transient in Section 3.4.14.

Unfortunately, no spectroscopic redshifts were measured for lensed galaxies in this field. An attempt to obtain spectroscopy in this field in 2024 October (soon after the JWST observations, and prompted by the discovery of the candidate transient, see Section 3.4.14) failed due to weather conditions. We were awarded time on the Magellan telescope in 2025A (U. of Michigan allocation, PI: Sharon) to obtain spectroscopic redshifts of multiple images in this field, and will revisit the lens model once spectroscopic redshifts are secured.

To compute the model presented here, we anchor the model at the photometric redshift of System #1, and left the redshifts of all the other systems as free parameters in the model. We then test the results of the model against the photometric redshifts of other systems. Photometric redshifts were estimated using *Prospector* (see Section 3.4.8) to fit the photometry of Image #10.1,  $F606W = 27.36 \pm 0.44$  (consistent with no detection),  $F150W2 = 22.65 \pm 0.02$ , and  $F322W2 = 21.08 \pm 0.01$ . Figure 3 shows the fit results. The redshift posterior distribution of System #1 is consistent with  $z_{phot} = 2.0_{-0.4}^{+0.7}$ . Systems #2 and #3 have broader posterior distributions, favoring redshifts  $2 \lesssim z \lesssim 4$ . We produce two models, one assuming that System #1 is at  $z = 2.0$ , and one assuming  $z = 2.5$ . Both models produce satisfactory results in terms of reproducing the lensing observables and low rms. However, the model that assumes  $z_{src1} = 2.0$  predicts redshifts for Systems #2 and #3 that are inconsistent with the photo- $z$  estimates. We therefore adopt the  $z_{src1} = 2.5$  model moving forward, and report the model parameters and lensing outputs from this model in Table 6.

The JWST-SLICE and single-band HST imaging allow us to identify and map substructure in more than half of the systems, multiplexing the number of lens model constraints. As shown in Figure 5, the overall shape of the projected mass distribution is elongated in the North-West/South-East direction. Our final best-fit mass model has a rms of  $0''.22$ . System #4 has an optimized redshift of  $4.980_{-0.40}^{+0.03}$  for clump 1 and  $4.743_{-0.29}^{+0.15}$

for clump 2. The rest of the optimized redshifts for the systems in this cluster are below  $z \sim 4$ .

#### 3.4.14. Candidate Transient in SPT-CL J0516–5755

The most prominent lensed system in this field is System #1, lensed into a set of three full images of a red dusty galaxy appearing South of the BCG, and a fourth partial image clearly seen in the light of a cluster-member galaxy  $1''.8$  North-East of the BCG. Interestingly, in Image #1.3, we identify a point-like emission clump that does not appear in any of the other images. Owing to the low distortion, good resolution, and clear symmetry between the three full images, the identification is unambiguous. The candidate could possibly be a lensed supernova at  $z \sim 2$ , adopting the photometric redshift of its host galaxy. The lens model predicts the time delay between the multiple images of the lensed source. If this is indeed a transient and not a foreground interloper, the model predicts that this is the second image to appear; the first one occurred in Image #1.1 (the Western image)  $\sim 4000$  days prior, and the next appearance will be in Image #1.2 in 560 days. The model is limited by the lack of spectroscopic redshifts, however, estimating the time delays with a model that anchors this source at  $z = 2$  instead of  $z = 2.5$  yields similar results, predicting that the first image occurred  $\sim 4300$  days before the second (current) one, and the third image will appear 530 days after the second image. We therefore predict that a counter image of the candidate transient event will be visible in Image #1.2 of the galaxy in the next two years.

#### 3.4.15. SPT-CL J2011–5228

SPT-CL J2011–5228 (SPT2011), located at  $z = 1.064$ , is optimized with a total of 3 systems (16 multiple images and 100 lensing constraints), where 1 system has a spectroscopic redshift and the remaining 2 systems are optimized within the model. A total of 112 cluster member galaxies are included in the model, and are fitted with a scaling relation optimizing 2 parameters. The model uses 7 potentials to describe the mass of the cluster. The final model has an rms of  $0''.15$ , and the mass enclosed within 200 kpc and 500 kpc is  $\sim 2.51 \times 10^{14} M_{\odot}$  and  $\sim 7.73 \times 10^{14} M_{\odot}$ , respectively. We provide a detailed description of the cluster modeling in the following paragraphs.

The SLICE JWST imaging for this cluster reveals an impressive amount of substructure in the main lensed galaxy system. These clumps appear across five main multiple images, including a radial arc. The resolution of JWST reveals this radial arc in precise detail, showing that it is an almost-exactly mirrored counterpart of the South-most arc. JWST also demonstrates that



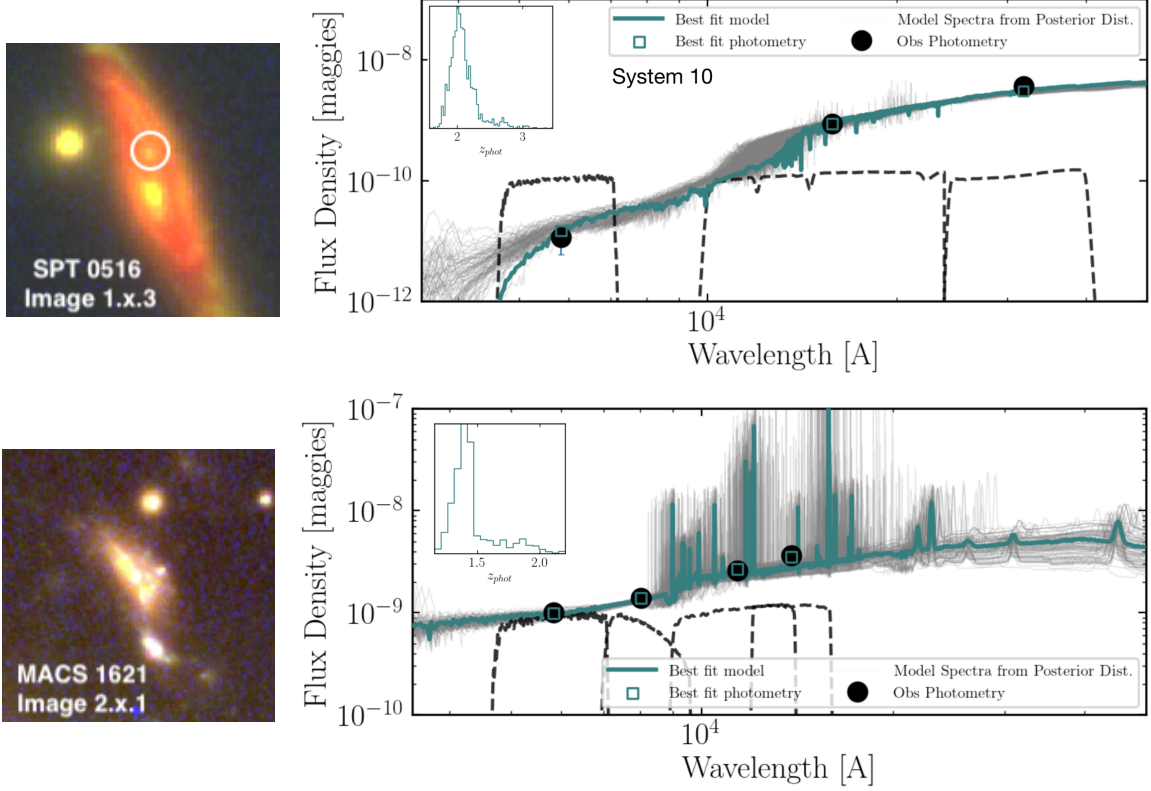


**Figure 3.** *Top:* SED analysis of Image #10.1 in SPT-CL J0516–5755, shown in the postage stamp on the left. The candidate transient is circled in white. The photometry is measured in ACS/F606W, NIRCcam/F150W2, and NIRCcam/F322W2. The best-fit redshift is consistent with  $z_{phot} = 2.0^{+0.7}_{-0.4}$ , as can be seen in the inset. *Bottom:* SED analysis of System #2 in MACS J1621.4+3810, shown in the postage stamp on the left. The photometry is measured in ACS/F606W, ACS/F814W, WFC3IR/F110W, and WFC3IR/F140W. The estimated redshift measurement is set at  $z_{phot} = 1.5^{+0.3}_{-0.2}$ .

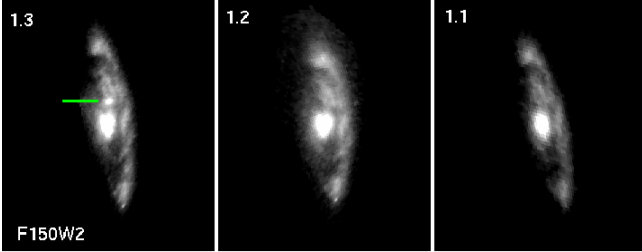


**Figure 4.** Source projection of the three multiple images of System #1 in SPT0516, produced by ray-tracing the NIRCcam/F150W2 image through the best-fit lens model. A green line in the left panel points to the candidate transient, which appears in Image #1.3 of the source, and missing from the two counter images. The host galaxy is assumed to be at  $z_{phot} = 2.5$ . Spectroscopic confirmation is pending. The host galaxy is not visible in the ACS/F606W band, likely due to obscuration by dust. The model predicts that, if indeed a transient, it will reappear in Image #1.2  $\sim$  530 days after its first appearance in Image #1.3.

the South-West image is actually a merging pair that is intersected by the critical curve of the model, with a multiplicity of up to 3 within this image alone depending on the location of the substructure clumps in the

lensed galaxy. To construct a lens model for this cluster, we use the spectroscopic redshift measurement for the main lensing system from Collett et al. (2017). We reproduce the lens model from this paper and add 25 different clumps to the model. These clumps are only clearly resolved in JWST. To reproduce the positions of each of the clumps, a total of two cluster-scale DM halos are required in the *Lenstool* model, with one halo centered on the BCG and the second one located West of the cluster, near the merging pair. This extra halo also partially accounts for the shear effect produced by several large foreground galaxies, which was previously noted in Collett et al. (2017). A third DM halo is also added near the foreground galaxy by image #1.x.3 to account for the shearing effect of this galaxy on this image. Two small cluster member galaxies are located inside the main tangential arc and contribute a small local effect on the shear, so we optimize these galaxies separately. We also optimize the second brightest cluster member galaxy and the two galaxies near the second image of the main system (System #1), as these galaxies are likely contributing to the mass producing the lensing effect. System #2 is spatially associated with System

#1 but has a different multiplicity than the rest of the substructure clumps within the lensed galaxy. We assign its redshift to be the same as the spec-z for System #1 to reproduce the observed lensing constraints. System #3 has an optimized model redshift below  $z \sim 4$ .

#### 4. RESULTS

The clusters presented in this paper represent the first effort in cluster mass modeling from the first few months of observations of the SLICE program, and were not deliberately selected to be a representative subsample. Nevertheless, they span both a wide range of redshifts (from  $z \sim 0.2$  to  $z \sim 1$ ) and masses ( $M_{500} \sim 2 \times 10^{14} M_{\odot}$  to  $M_{500} \sim 12 \times 10^{14} M_{\odot}$ ), which covers nearly the entire range of the parent sample. The lensing properties of the subsample are thus worth considering in aggregate. In this section, we discuss several of the key results from the strong lens models, including the projected surface mass density measurements and the alignment of the mass peaks with the *Chandra* X-ray observations, the identification of new constraints facilitated by inspection of the JWST images, and an estimate of the lensing strength of each cluster.

##### 4.1. Mass

We compute the projected mass within 200 kpc and 500 kpc for each strong lensing cluster, which we report in Table 5. We use the mass enclosed within these distances as our primary metric since it is difficult to use strong lensing models to approximate quantities like  $M_{500}$  without drawing potentially non-physical assumptions about the shape of the overall cluster mass distribution. Strong lensing only constrains the central cluster mass. This limitation can be seen in the projected mass surface density plots shown in Figure 5, where we plot contours of the mass within a uniform box that extends beyond 500 kpc for all clusters. Although we plot these contours across a large region to show the general mass distribution of the cluster, the strong lensing constraints of each cluster are limited to a region that is spatially smaller than 500 kpc from the BCG. This limitation means that the estimation of cluster mass at larger radii carries a high level of uncertainty that we cannot restrict without the introduction of other modeling techniques (i.e. weak lensing). We thus restrict our mass measurements to 200 and 500 kpc (see Table 5 for mass estimates) and leave any inspection of larger radii to future work. We additionally overplot the density contours from the *Chandra* X-ray observations listed in Table 3. These data are available for 8 out of the 14 clusters. In most cases, the center of the X-ray peak aligns well with the center of the mass peak of the cluster, except for PSZ1G091 which displays a noticeable

misalignment that is discussed in Section 3.4.11. We show these data together to emphasize the potential of the SLICE program to make use of multi-wavelength observations when studying the physical and dynamical properties of the observed clusters.

##### 4.2. New Constraints

The new JWST imaging facilitates the discovery of new strong lensing features that could be used to constrain the lens models. These come in three flavors: complete new systems that were not previously identified, discovery of new counter-images of known lensed galaxies or confirmation of suspected candidates, and identification and mapping of previously unresolved features and substructure within arcs, including space-resolution positioning of images previously only detected in MUSE data with no HST counterpart. The number of newly discovered features varies from field to field. While the JWST observations are uniform across the sample, the available archival data and literature range from as little as one frame of HST imaging (e.g., SPT-CL J0516–5755) and no previous lensing analysis, through multi-wavelength HST imaging and MUSE spectroscopy (e.g., clusters observed by treasury programs) and published lensing analysis for clusters that have previously been well studied. New lensed systems are typically either too red or too faint, or both, to have been discovered without JWST (e.g., System #1 in SPT0516). The identification of new clumps benefits from the high spatial resolution of NIRCam. Adding clumps as constraints multiplexes the number of constraints, and adds leverage over the lensing potential as it probes the relative spatial magnification in resolved arcs. An example of the plethora of clumps in some of the most highly extended arcs is shown in Figure 2. Table 7 lists the total number of systems, multiple images, and strong-lensing constraints (i.e., the sum of the multiple images of all the individual clumps) that were used for modeling each cluster. Figure 6 provides a visualization of the number of new and previously-known systems. Where available, we determined the number of pre-JWST strong lensing features from the literature or publicly-available lens models on MAST. For clusters that have not had a public or published lens model, we assessed the pre-JWST identification by a visual inspection of the archival data by two of the authors, at least one of whom was not involved in computing the JWST-based model. We note that the numbers presented in Table 7 and Figure 6 only represent the features that were used to constrain the lens models. In many of our fields, there are additional candidate systems and im-

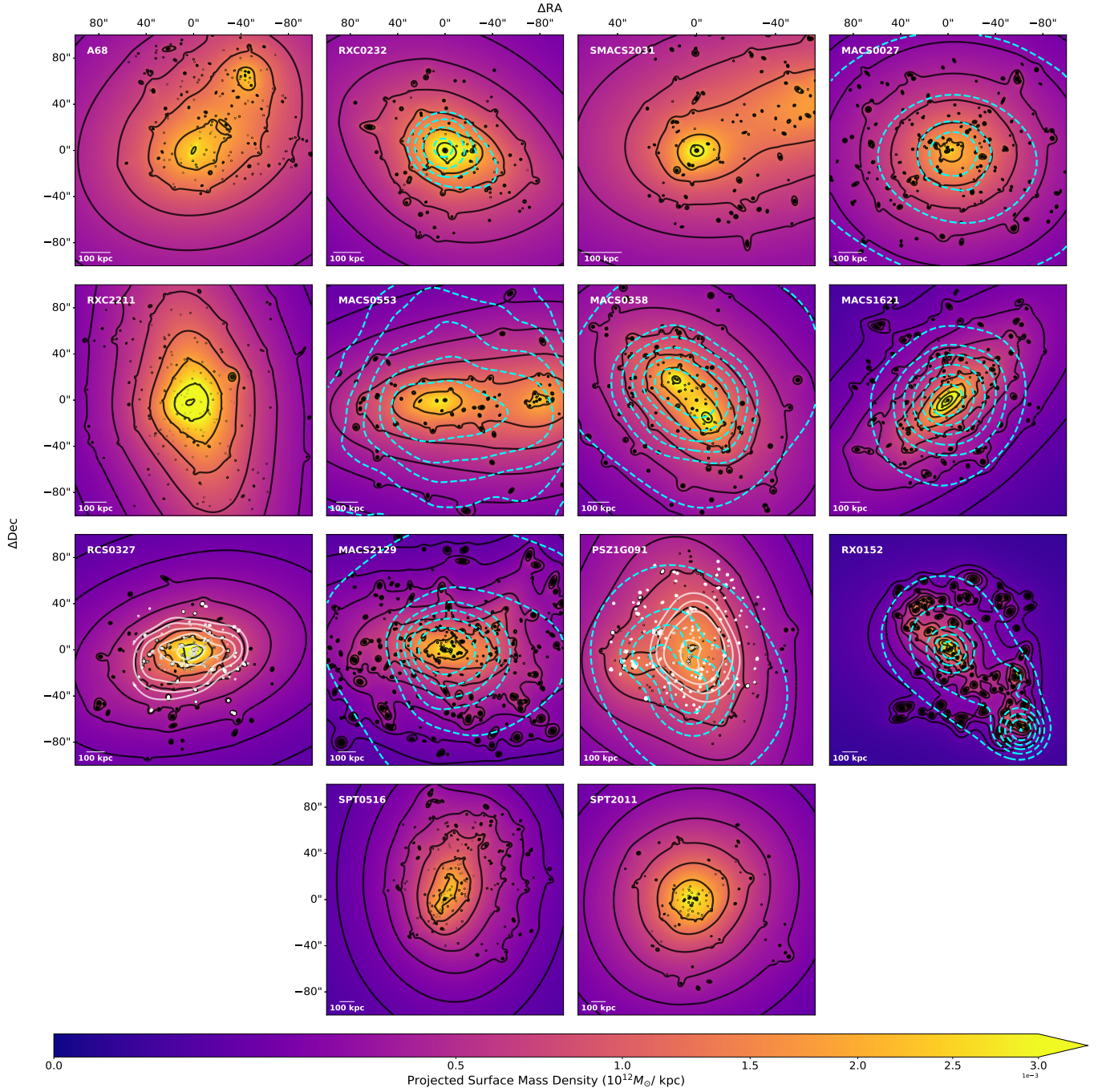


**Figure 5.** The total projected surface mass density of each cluster is measured within a  $200'' \times 200''$  box centered on the reference coordinates for each lens model made with `Lenstool`, which are listed in the second column of [Table 6](#). Logarithmically-spaced contours of the mass measured with `Lenstool` are plotted in black lines between the lower and upper limits of the mass scale given in the colorbar. Mass contours for the two `WSLAP+` models are shown in white across the lower and upper limits of the same mass scale. Chandra X-ray observations are available for eight out of the fourteen clusters. For the purposes of presentation, we smooth the X-ray map with the `csmooth` routine using adaptive smoothing to  $2.5\sigma$  significance. We convolve the smoothed X-ray map with a Gaussian of standard deviation 5 pixels and overplot logarithmically-spaced contours in cyan dashed lines over the projected mass map. A uniform scale length of 100 kpc is shown in the bottom left corner of each plot.

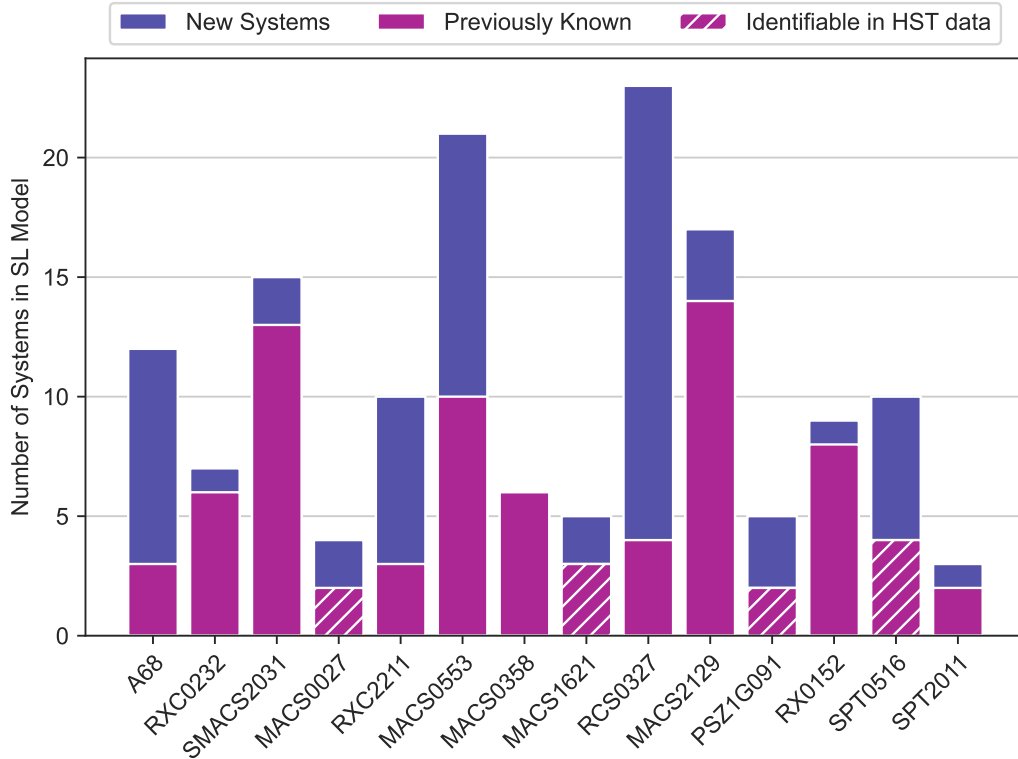


**Figure 6.** The number of systems used to construct the strong lensing models in this paper is broken down to demonstrate the effect of JWST imaging on the identification and use of constraints in the modeling process; this number does not include candidate systems. The total number of systems in the paper is given by the size of the whole bar for each cluster. The bar is then subdivided into the magenta section, which represents lensed systems that were previously identified in other publications for these clusters, while the purple section represents the number of new lensed systems identified in the SLICE-JWST images. Four clusters in this paper do not have published or public strong lensing models available: MACS0027, MACS1621, PSZ1G091, and SPT0516. For these clusters, two of the authors independently inspected the available HST imaging to identify strong lensing systems without the use of JWST. The number of systems identifiable in HST data are shown in the hashed magenta section of each bar.

ages that were observed but not used as constraints (see Section 3.4 for cluster-by-cluster account).

New lensing systems were discovered in most cluster fields. In some, the number of systems used to constrain lens models has more than doubled (notably, RCS0327, MACS0553, A68, and RXC2211). In addition, SPT2011, PSZ1G091, and RCS0327 include dozens of constraints coming from clumps in giant arcs (see Table 4). While the clusters presented in this work are not a representative sample, they span the range of SLICE targets in both redshift and mass. These number counts highlight the added value of JWST imaging and validate our observing strategy for facilitating lensing analyses of the observed clusters. We expect that both the accuracy and precision of the lensing outputs would improve with number of lensing constraints (Johnson & Sharon 2016). In future work, we will conduct a thorough investigation and comparison to expectations from simulations, by en-

forcing a systematic identification of arc candidates and a uniform use of the available clumps in lens models.

#### 4.3. Lensing Strength

One of the most important applications of strong lensing models is their use in studying the background universe. This can be accomplished by computing the magnification of lensed sources out of the lens models. In the era of JWST, this is a particularly relevant quantity to be used to discover and characterize high-redshift galaxies. We examine this quantity for the 14 clusters in this paper following the method used by Fox et al. (2022), where we define the ‘lensing strength’  $\mathcal{A}_{|\mu|\geq 3}$  of a cluster based on the size of the area in the image plane where a source at a redshift  $z_s$  is magnified by a factor  $\mu \geq 3$ . This threshold is chosen as a useful break-point that describes a source that has been magnified enough for identification and study while still remaining spatially close to the strong lensing constraints at the cen-



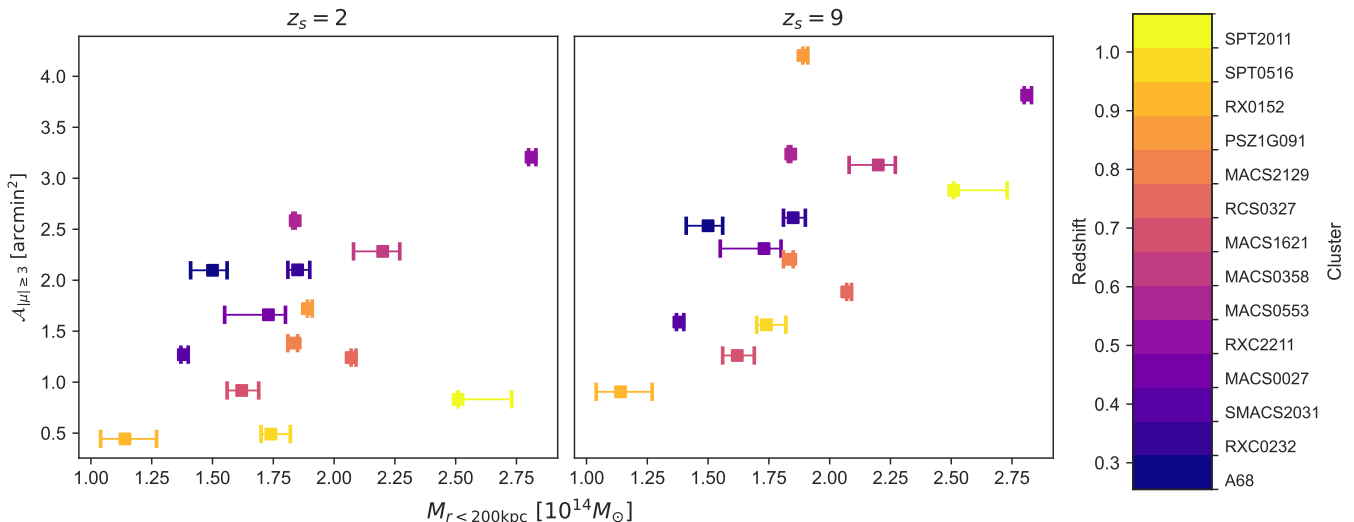


**Figure 7.** The lensing strength of each cluster, defined as the area in arcmin<sup>2</sup> at which a source has an absolute magnification greater than 3, is shown for a source at  $z = 2$  in the left-hand plot, and  $z = 9$  in the right-hand plot. It is plotted relative to the projected surface mass enclosed within 200 kpc. Each point is color-coded to correspond to a specific cluster, where the names are given on the right-hand side of the colorbar. The left-hand side of the colorbar shows the approximate redshift of the clusters, where the range of redshifts within the colorbar fully covers the upper and lower limits of the redshifts for the clusters.

ter of the cluster. Indeed, lower magnification factors further away from the cluster may not be as reliable in strong lensing models. Additionally, a source magnified by this factor can be included in studies of the high- $z$  luminosity function (see e.g. Salmon et al. 2018; Atek et al. 2023) but remains within an acceptable range of the strong lensing area to have a reliable magnification measurement (see e.g. magnification map uncertainties in Cerny et al. 2018). We choose to measure the lensing strength for a source at  $z_s = 2$ , a common redshift for lensed galaxies used as constraints in strong lensing models, and at  $z_s = 9$ , a common target redshift for high- $z$  galaxy searches. This also eases comparison among clusters, as it minimizes the impact of the distance between the lens and the observer.

We compute the lensing strength of every cluster and plot this quantity relative to the mass enclosed within 200 kpc as shown in Figure 7. Generally, all clusters see an increase in lensing strength for a source at  $z_s = 9$  relative to a source at  $z_s = 2$ . This is to be expected. PSZ1G091 is the most extreme example of this behavior, but we note that this jump in lensing area arises due to the addition of the cluster’s Eastern mass clump at high redshift. The presence of this clump more than doubles the amplification area, as shown in the figure. However, this measurement is derived from a model without spectroscopic redshifts, and should thus be treated as preliminary until the lens model can be more precisely constrained. The sharp increase does seem to point to a potential trend, in that clusters at lower redshifts see

only a minimal increase in lensing strength, while clusters at high redshifts experience a larger shift, potentially because a cluster at  $z \gtrsim 0.9$  is more limited in its potential to magnify sources at  $z \sim 2$ . This trend can also be seen in the lensing strength histogram reported in Figure 8. This demonstrates that most of the cluster lensing strength to amplify sources at  $z_s = 9$  is more evenly distributed, in comparison with the more concentrated area that amplifies a source at  $z_s = 2$ .

#### 4.4. High redshift detections with SLICE

The detection of high redshift overdensities in the background of galaxy clusters is of particular interest in clusters with strong lensing, since background galaxies can appear brighter and bigger thanks to lensing effects. However, systems can also be identified as overdensities due to multiple image systems. Lensing models are needed to identify objects that are detected multiple times to separate lensed images from candidates for proto-clusters of galaxies, which can be verified with the use of spectroscopic identifications (Zheng et al. 2014; Caputi et al. 2021; Laporte et al. 2022; Noirot et al. 2023; Morishita et al. 2023).

In the field of MACSJ0027.8+2616, a galaxy at redshift 4.45 was identified more than five times in the MUSE data cube. Of these detections, four are visible in the JWST images but their geometrical configuration does not resemble that of a lensed system. For this reason, we considered this system as a galaxy proto-cluster candidate. However, our mass model of MACS0027 predicts that three of these detections are multiple images

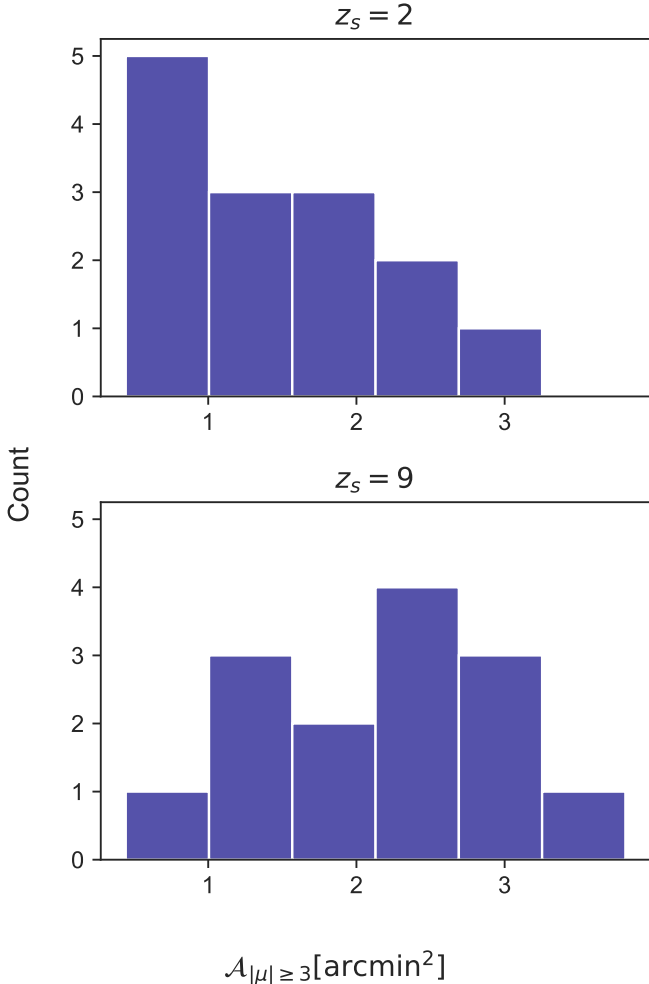


**Figure 8.** A histogram of the lensing strength for a source at  $z = 2$  (top panel) and a source at  $z = 9$  (bottom panel) for all clusters studied in the paper, divided into 6 equally spaced bins. The lensing strength increases for a source at  $z_s = 9$  relative to a source at  $z_s = 2$ , and the distribution of lensing strength at a higher redshift is also more uniform than for a source at  $z_s = 2$ .

(shown as System #30 in the model), while the other candidates do not show any signs of multiplicity. With the information available at the moment, it is thus unclear if these are multiple image systems or a proto-cluster candidate. Further investigation is needed. The large area covered by the SLICE program is particularly suited for the morphological analysis of proto-cluster candidates. Indeed, some other clusters studied in this paper show similar overdensities of relatively high redshift galaxies. However, assessing whether these overdensities appear due to multiple images or because they are associated with a proto-cluster candidate is very difficult without complementary observations (e.g., spectroscopic follow-up or additional multi-band imaging).

At intermediate redshifts, beyond the cluster lenses, typically during the so-called cosmic noon ( $z \sim 1-3$ ), SLICE provides exquisite spatially resolved imaging at parsec and dozens-of-parsec scales of magnified clumpy galaxies. Notably, the high sensitivity of NIRCcam reveals dusty arcs that are too faint to be detected in the HST WFC3/IR channel (e.g., in SPT0516), and that benefit from ongoing spectroscopy follow-up. Strong lensing provides the only way to access the internal physical scales that are important to characterize the individual star-forming regions at these redshifts (typical clump sizes of  $10 - 10^2$  parsecs and stellar masses of  $\sim 10^5 - 10^9 M_\odot$ ; see [Claeyssens et al. 2023](#); [Rigby et al. 2023b](#)). Despite significant advancements with JWST, the formation mechanisms and contributions of stellar clumps to galaxy mass build-up remain debated (e.g., [Mowla et al. 2022](#); [Claeyssens et al. 2024](#); [Lahén et al. 2024](#); [Pfeffer et al. 2025](#)). Current and upcoming mass modeling efforts will produce the necessary underlying lens models to support the investigation of spatially resolved properties of high redshift galaxies.

Additionally, the imaging from the SLICE program has identified a promising lensed SN candidate in SPT0516, located in a dusty galaxy that is too faint to be observed in ACS/F606W, but revealed in NIRCcam/F150W and F322W. Further investigation is needed to confirm the nature of this object, which could be a new target of choice for time-delay cosmography for precise measurements of  $H_0$ , independent of distance ladder (e.g., [Kelly et al. 2023](#); [Pascale et al. 2024](#)). Notably, only four lensed SNe have been confirmed to date, compared to about 300 lensed quasars (e.g., [Birrer et al. 2024](#), for a review).

## 5. DISCUSSION AND CONCLUSIONS

The JWST SLICE program is designed to observe the co-evolution of luminous and dark matter in galaxy clusters across cosmic time, spanning a period of 8 Gyrs ( $0.2 < z < 1.9$ ), for structures more massive than  $M_{500} > 2 \times 10^{14} M_\odot$ . This work features a randomly-sampled selection of 14 strong lensing clusters from this program that span a representative range of both redshift and mass, and presents the first results for the properties of these clusters from the collaboration’s strong lensing modeling efforts. In nearly every cluster, the use of JWST imaging adds to the number of lensed sources used to build the strong lensing model (see [Figure 6](#)). This increase can be as low as 1 additional system and

**Table 4.** Cluster Statistics Table

| Cluster            | # Systems | # Images | # SL Constraints | # Tangential Arcs | # Radial Arcs | # $z_{spec}$ | Model RMS (") |
|--------------------|-----------|----------|------------------|-------------------|---------------|--------------|---------------|
| Abell 68           | 12        | 36       | 42               | 36                | 0             | 5            | 0''.47        |
| RXC J0232.2–4420   | 7         | 26       | 26               | 18                | 4             | 2            | 0''.40        |
| SMACS J2031.8–4036 | 15        | 53       | 67               | 49                | 4             | 13           | 0''.40        |
| MACS J0027.8+2616  | 4         | 19       | 31               | 19                | 0             | 2            | 0''.44        |
| RXC J2211.7–0349   | 10        | 32       | 45               | 28                | 4             | 1            | 0''.80        |
| MACS J0553.4–3342  | 21        | 57       | 102              | 57                | 0             | 4            | 0''.67        |
| MACS J0358.8–2955  | 6         | 16       | 16               | 16                | 0             | 2            | 0''.21        |
| MACS J1621.4+3810  | 5         | 16       | 22               | 12                | 4             | 0            | 0''.27        |
| RCS2 032727–132623 | 23        | 61       | 184              | 47                | 14            | 5            | 0''.82        |
| MACS J2129.4–0741  | 17        | 53       | 53               | 38                | 4             | 13           | 0''.79        |
| PSZ1 G091.83+26.11 | 5         | 17       | 89               | 15                | 2             | 0            | 0''.41        |
| RX J0152.7–1357    | 9         | 19       | 31               | 19                | 0             | 1            | 0''.45        |
| SPT-CL J0516–5755  | 10        | 25       | 53               | 25                | 0             | 0            | 0''.22        |
| SPT-CL J2011–5228  | 3         | 16       | 100              | 14                | 2             | 1            | 0''.15        |

NOTE—Number counts for various properties of the lens model presented in this paper. The number of systems gives the total number of lensed sources within the model, the number of images gives the multiplicity of the lensed sources, and the number of strong lensing constraints gives the total number of lensed objects (i.e. lensed galaxy images including clumps) that were used to constrain the strong lensing model.

**Table 5.** Cluster Mass Table ( $10^{14} M_{\odot}$  with  $2\sigma$  uncertainty)

| Cluster            | M(<200kpc)             | M(<500 kpc)            | $R_E$ (")<br>$z = 2$ | $R_E$ (")<br>$z = 9$ |
|--------------------|------------------------|------------------------|----------------------|----------------------|
| Abell 68           | $1.50^{+0.06}_{-0.09}$ | $4.59^{+0.17}_{-0.30}$ | 15.99                | 26.12                |
| RXC J0232.2–4420   | $1.85^{+0.05}_{-0.04}$ | $4.51^{+0.21}_{-0.21}$ | 25.30                | 30.50                |
| SMACS J2031.8–4036 | $1.38^{+0.02}_{-0.01}$ | $4.47^{+0.21}_{-0.10}$ | 22.84                | 28.29                |
| MACS J0027.8+2616  | $1.73^{+0.07}_{-0.18}$ | $5.09^{+0.37}_{-0.84}$ | 9.92                 | 22.36                |
| RXC J2211.7–0349   | $2.81^{+0.02}_{-0.01}$ | $7.04^{+0.11}_{-0.08}$ | 43.60                | 52.13                |
| MACS J0553.4–3342  | $1.84^{+0.00}_{-0.01}$ | $6.14^{+0.01}_{-0.02}$ | 32.15                | 39.37                |
| MACS J0358.8–2955  | $2.15^{+0.14}_{-0.03}$ | $5.99^{+1.38}_{-0.11}$ | 28.21                | 35.03                |
| MACS J1621.4+3810  | $1.62^{+0.07}_{-0.06}$ | $3.91^{+0.26}_{-0.29}$ | 21.30                | 26.52                |
| RCS2 032727–132623 | $2.07^{+0.02}_{-0.00}$ | $5.14^{+0.16}_{-0.02}$ | 23.59                | 31.98                |
| MACS J2129.4–0741  | $1.84^{+0.01}_{-0.03}$ | $5.32^{+0.10}_{-0.19}$ | 20.80                | 29.77                |
| PSZ1 G091.83+26.11 | $1.89^{+0.02}_{-0.00}$ | $7.61^{+0.21}_{-0.12}$ | 4.50                 | 23.21                |
| RX J0152.7–1357    | $1.14^{+0.13}_{-0.10}$ | $3.44^{+0.40}_{-0.42}$ | 11.23                | 17.00                |
| SPT-CL J0516–5755  | $1.74^{+0.08}_{-0.04}$ | $5.10^{+0.42}_{-0.18}$ | 6.81                 | 22.36                |
| SPT-CL J2011–5228  | $2.51^{+0.22}_{-0.0}$  | $7.73^{+1.75}_{-0.00}$ | 6.22                 | 33.38                |

NOTE—Mass estimates summary from all strong lensing models, describing the mass enclosed within 200 kpc and within 500 kpc, are provided in the first two columns. The second two columns provide a measurement of the cluster’s Einstein radius  $R_E$  at two different redshifts. The mass estimate is calculated starting from the reference coordinates listed in Column 2 of Table 6.

as large as 15 additional systems. It appears to be uncorrelated to cluster redshift or mass. JWST imaging

is particularly useful for revealing red, dusty galaxies, as well as very faint systems, both of which are essen-

tially invisible in HST imaging (Pérez-González et al. 2023). Of the 15 models presented in this paper for the 14 clusters studied, 4 describe clusters that have not been previously published in the literature: MACS0027, MACS1621, PSZ1G09, and SPT0516. The constraints used to create these models depend on JWST imaging to confirm counter-images of lensed galaxies that appear very faint in HST as well as to identify red and dusty galaxies that only appear with JWST.

The process used to construct the lens models presented in this paper varies by cluster, even when using the same modeling algorithm. The main objective was to create a basic strong lens model for each cluster that could reproduce the observed JWST multiple image constraints, and constrain the clusters’ total mass distribution. The amount of lensed substructure used as constraints, availability of spectroscopic redshifts, and reliability of photometric redshifts varies from cluster to cluster. These models should thus be treated as preliminary results from the SLICE program, and may be updated in future work. We provide candidate lensing systems and substructure clumps for several of the clusters studied in this paper in Table 7. These candidates are not used in this paper because they have a marginal effect on the derivation of the global mass and magnification results we discuss in Section 4, but studies of questions like the magnification and source-plane reconstruction of lensed galaxies, substructure statistics, and the dark matter distributions of these clusters may benefit from their use. We thus include them here as a reference for future work.

In general, the use of SLICE JWST images improves the ability of the strong lensing models to reproduce the observed constraints, as seen in the lower rms values reported for all models in this paper compared to previous literature. Although the difference in rms is sometimes quite small ( $0''.01$  for MACSJ2129.4–0741, for instance), the inclusion of new lensed systems into the model (3 new systems in the aforementioned cluster) places tighter constraints on the global mass distribution, and can thus be treated as an overall improvement. In the four clusters studied in this paper where no lens models had previously been published, the specific contribution of JWST is to provide identifications of multiple image systems that are crucial to creating the strong lensing model. For example, inspection of archival imaging for these clusters yielded identifications for less than half the systems used in the final lens model presented in this paper, with the exception of MACS1621. Each of these clusters contains a red, dusty galaxy that was used as a constraint in the model, and which is crucial

to resolving the shape of the overall mass distribution of the cluster.

Additionally, the ability of JWST to resolve complex morphology within the multiple images aids in the construction of the lens models. For instance, inspection of HST imaging for SPT2011 seems to indicate that a single lensed image is produced in the South-East (Image #1.x.2 in Figure 1). However, examination of the SLICE JWST imaging reveals that this image is actually a merging pair, with a multiplicity of up to 3 spread across the intersecting critical curve, depending on the location of the substructure clumps in the lensed galaxy. The JWST imaging is also well-suited to resolving images of radial arcs that may appear within a cluster’s lensing configuration. Radial arcs are a relatively uncommon strong lensing feature that lie at or near the center of a cluster’s mass potential. That means they are often obscured by the light of surrounding cluster member galaxies and the BCG (Bartelmann 2010a,b), making their identification reliant on spectroscopic follow-up. However, inspection of the # Radial Arcs column of Table 4 shows clearly that the wavelength range covered by the SLICE-JWST imaging is able to either directly identify radial arcs through visual inspection, or lend compelling evidence to the presence of a radial arc, i.e. by revealing continuum emission separate from the BCG and cluster member galaxies at the location of a predicted multiple image.

Beyond the cluster lenses, the SLICE program provides exquisite spatially resolved imaging of the clumpy inter stellar medium (ISM) of high redshift lensed galaxies. This is complemented by ongoing spectroscopic follow-up, as in the case of SPT0516, which will be observed on the Magellan telescope in 2025A (U. of Michigan allocation, PI: Sharon). Combined with other facilities in the submillimeter and mid-infrared, e.g. ALMA and MIRI (Umehata et al. 2025; Rigby et al. 2025), SLICE has the potential to bring new constraints on the physical properties governing the star formation activity in high redshift giant molecular clouds during cosmic noon and beyond, a key epoch for galaxy evolution (Madau & Dickinson 2014; Weaver et al. 2023; Lucia et al. 2025).

This paper presents early results from the first clusters observed in the SLICE-JWST program. At the time of this paper’s release, the SLICE sample covers a total of 100 galaxy clusters, spread across a broad range of redshifts and masses. This wealth of data is designed to probe the co-evolution of luminous and dark matter across cosmic time by studying a variety of cluster properties, from dark matter and ISM distributions, to globular cluster populations, proto-cluster discoveries, and



studies of the background universe. This paper thus marks the first step toward the future science that will be accomplished using the full SLICE-JWST sample, including providing constraints on cluster mass distributions and identifying new lensed galaxies. Since observations are still ongoing, a complete breakdown of the SLICE program, including a presentation of the whole observed cluster sample, together with statistical analyses of various cluster properties, such as lensed galaxy substructure counts, will be presented in the forthcoming survey paper (Mahler et al., in prep). This paper will be released once observations have concluded.

This work is based on observations made with the NASA/ESA/CSA James Webb Space Telescope. These observations are associated with program JWST-GO-5594. This research is based on observations made with the NASA/ESA Hubble Space Telescope. These observations are associated with programs 9290, 9770, 10493, 11591, 12100, 12166, 12267, 12313, 12362, 12371, 12884, 13412, 14096, 14098, 14630, and 15132. New and archival data presented in this paper were obtained from the Mikulski Archive for Space Telescopes (MAST) at the Space Telescope Science Institute, which is operated by the Association of Universities for Research in Astronomy, Inc., under NASA contract NAS5-26555 and NASA contract NAS5-03127 for JWST.

Support for program JWST-GO-5594 was provided by NASA through a grant from the Space Telescope Science Institute, which is operated by the Association of Universities for Research in Astronomy, Inc., under NASA contract NAS5-03127. MJ, DL, NP, SW, JD, AE are supported by the United Kingdom Research and Innovation (UKRI) Future Leaders Fellowship ‘Using Cosmic Beasts to uncover the Nature of Dark Matter’ (grant number MR/X006069/1). ML acknowledges the Centre National de la Recherche Scientifique (CNRS) and the Centre National des Etudes Spatiales (CNES) for support. This work was performed using facilities offered by CeSAM (Centre de donnéeS Astrophysique de Marseille). J.M.D. acknowledges support from project PID2022-138896NB-C51 (MCIU/AEI/MINECO/FEDER, UE) Ministerio de Ciencia, Investigación y Universidades. MM acknowledges support from grant RYC2022-036949-I financed by the MICIU/AEI/10.13039/501100011033 and by ESF+ and program Unidad de Excelencia María de Maeztu CEX2020-001058-M. AS acknowledges support from NSF Astronomy grant 2109035.

*Facilities:* JWST(NIRCam), HST(ACS, WFC3), VLT(MUSE)

*Software:* astropy (Astropy Collaboration et al. 2013), Source Extractor (Bertin & Arnouts 1996b) Lenstool(Jullo et al. 2007) SAOImageDS9, Astrodrizzle, CIAO, Matlab, IDL, IRAF

## APPENDIX

### A. APPENDIX INFORMATION

Table 6. Best Fit Parameters

| Cluster   | REF.                | Object                | $\Delta\alpha$ (")        | $\Delta\delta$ (")        | $\epsilon$              | $\theta$ (°)                | $r_{\text{core}}$ (")    | $r_{\text{cut}}$ (") | $\sigma$ (km s <sup>-1</sup> ) |
|-----------|---------------------|-----------------------|---------------------------|---------------------------|-------------------------|-----------------------------|--------------------------|----------------------|--------------------------------|
| Abell 68  | 9.278516,           | DM H1                 | $0.51^{+1.10}_{-0.46}$    | $-2.66^{+0.30}_{-0.85}$   | $0.350^{+0.10}_{-0.03}$ | $27.800^{+4.26}_{-0.14}$    | $17.924^{+1.75}_{-0.89}$ | [364]                | $866^{+37}_{-28}$              |
|           | 9.156716            | BCG H2                | [0]                       | [0]                       | $0.452^{+0.10}_{-0.06}$ | $35.087^{+11.52}_{-10.84}$  | $0.145^{+1.54}_{-0.03}$  | $24^{+1}_{-11}$      | $238^{+57}_{-2}$               |
|           |                     | DM H3                 | $-43.992^{+0.60}_{-0.71}$ | $65.994^{+0.69}_{-1.23}$  | $0.048^{+0.02}_{-0.03}$ | $6.3^{+35.7}_{-37.8}$       | $14.354^{+0.89}_{-2.21}$ | $81^{+5}_{-29}$      | $754^{+15}_{-29}$              |
|           |                     | Gal. H4               | [27.370]                  | [22.0897]                 | $0.577^{+0.02}_{-0.18}$ | $34.251^{+6.09}_{-10.32}$   | $26.887^{+3.13}_{-2.06}$ | $41^{+13}_{-6}$      | $550^{+53}_{-3}$               |
|           |                     | L <sub>*</sub> Gal.   | -                         | -                         | -                       | -                           | [0.03]                   | $21^{+2}_{-5}$       | $153^{+1}_{-12}$               |
| RXC0232   | 38.077317,          | DM H1                 | $-0.188^{+0.78}_{-0.08}$  | $-1.483^{+0.23}_{-0.29}$  | $0.291^{+0.05}_{-0.00}$ | $131.735^{+0.95}_{-2.99}$   | $10.274^{+0.01}_{-1.98}$ | [347]                | $815^{+6}_{-44}$               |
|           | -44.346666          | BCG <sub>A</sub> H2   | [0]                       | [0]                       | [0.114]                 | [-42.0]                     | [0.213]                  | [71]                 | $340^{+3}_{-21}$               |
|           |                     | DM H3                 | $-21.556^{+0.39}_{-0.83}$ | $-2.436^{+0.35}_{-0.01}$  | $0.829^{+0.03}_{-0.08}$ | $160.770^{+1.09}_{-0.92}$   | $20.125^{+0.39}_{-5.53}$ | [347]                | $600^{+3}_{-31}$               |
|           |                     | BCG <sub>B</sub> H4   | [23.888]                  | [0.072]                   | [0.278]                 | [22.4]                      | [0.05]                   | $28^{+24}_{-5}$      | $244^{+13}_{-25}$              |
|           |                     | DM H5                 | [-63.836]                 | [20.239]                  | $0.499^{+0.04}_{-0.34}$ | $173.495^{+1.33}_{-162.80}$ | [0.021]                  | $10^{+31}_{-2}$      | $234^{+6}_{-26}$               |
|           | L <sub>*</sub> Gal. | -                     | -                         | -                         | -                       | [0.03]                      | $29^{+5}_{-2}$           | $148^{+9}_{-7}$      |                                |
| SMACS2031 | 307.971920,         | DM H1                 | $0.575^{+0.07}_{-0.06}$   | $-0.459^{+0.11}_{-0.06}$  | $0.270^{+0.02}_{-0.01}$ | $4.634^{+2.17}_{-0.22}$     | $6.718^{+0.11}_{-0.30}$  | [210]                | $637^{+13}_{-12}$              |
|           | -40.625216          | DM H2                 | $-61.398^{+0.00}_{-0.79}$ | $24.192^{+0.53}_{-0.09}$  | $0.561^{+0.03}_{-0.05}$ | $7.746^{+0.90}_{-3.67}$     | $22.159^{+2.18}_{-0.75}$ | [210]                | $983^{+30}_{-2}$               |
|           |                     | Gal. H3               | [0.07]                    | [-0.054]                  | [0.092]                 | [-0.4]                      | [0.057]                  | $29^{+1}_{-14}$      | $245^{+4}_{-2}$                |
|           |                     | L <sub>*</sub> Galaxy | -                         | -                         | -                       | -                           | [0.03]                   | $5^{+6}_{-0.4}$      | $194^{+6}_{-49}$               |
| MACS0027  | 6.940790,           | DM H1                 | $3.830^{+0.33}_{-0.59}$   | $-2.721^{+0.07}_{-0.41}$  | $0.123^{+0.03}_{-0.01}$ | $1.456^{+0.28}_{-0.76}$     | $24.219^{+1.59}_{-2.70}$ | [197.05]             | $1199^{+33}_{-77}$             |
|           | 26.2740340          | L <sub>*</sub> Gal.   | -                         | -                         | -                       | -                           | [0.03]                   | $3^{+4}_{-1}$        | $258^{+58}_{-62}$              |
| RXC2211   | 332.941368,         | DM H1                 | $-3.521^{+0.60}_{-0.01}$  | $-1.021^{+0.16}_{-0.99}$  | $0.743^{+0.01}_{-0.02}$ | $99.234^{+1.01}_{-0.15}$    | $24.921^{+1.84}_{-0.23}$ | [270]                | $1330^{+42}_{-1}$              |
|           | -3.828952           | DM H2                 | $5.922^{+0.34}_{-1.12}$   | $-2.359^{+0.29}_{-0.10}$  | $0.242^{+0.06}_{-0.00}$ | $13.834^{+7.55}_{-1.79}$    | $7.628^{+0.78}_{-0.26}$  | $59^{+4}_{-7}$       | $875^{+26}_{-5}$               |
|           |                     | Gal. H3               | [32.762]                  | [20.185]                  | $0.200^{+0.04}_{-0.03}$ | $83.332^{+31.95}_{-4.87}$   | $1.240^{+0.43}_{-0.92}$  | $7^{+1}_{-1}$        | $421^{+10}_{-85}$              |
|           |                     | Gal. H4               | [33.093]                  | [-28.094]                 | $0.126^{+0.09}_{-0.01}$ | $46.929^{+39.08}_{-7.21}$   | $4.784^{+1.67}_{-0.49}$  | $16^{+1}_{-2}$       | $128^{+16}_{-21}$              |
|           |                     | Gal. H5               | [42.565]                  | [10.534]                  | $0.383^{+0.12}_{-0.05}$ | $80.970^{+1.38}_{-40.30}$   | $4.498^{+2.38}_{-2.46}$  | $8^{+9}_{-1}$        | $47^{+44}_{-23}$               |
|           | L <sub>*</sub> Gal. | -                     | -                         | -                         | -                       | [0.03]                      | $14^{+1}_{-8}$           | $81^{+9}_{-19}$      |                                |
| MACS0553  | 88.357332,          | DM H1                 | $-7.108^{+0.11}_{-0.16}$  | $-2.082^{+0.04}_{-0.03}$  | $0.618^{+0.00}_{-0.01}$ | $4.392^{+0.08}_{-0.09}$     | $15.592^{+0.13}_{-0.14}$ | [178]                | $1091^{+2}_{-3}$               |
|           | -33.707728          | DM H2                 | $83.608^{+0.23}_{-0.10}$  | $-1.221^{+0.09}_{-0.07}$  | $0.258^{+0.01}_{-0.01}$ | $20.031^{+0.49}_{-0.66}$    | $19.249^{+0.09}_{-0.24}$ | [178]                | $956^{+3}_{-2}$                |
|           |                     | L <sub>*</sub> Gal.   | -                         | -                         | -                       | -                           | [0.03]                   | $6^{+0.13}_{-0.13}$  | $205^{+1}_{-1}$                |
| MACS0358  | 59.719446,          | DM H1                 | $-7.319^{+7.19}_{-0.86}$  | $-11.643^{+8.59}_{-8.82}$ | $0.377^{+0.20}_{-0.22}$ | $123.149^{+18.17}_{-69.03}$ | $9.506^{+25.36}_{-6.59}$ | [266]                | $758^{+197}_{-94}$             |
|           | -29.930547          | DM H2                 | $18.042^{+6.60}_{-1.00}$  | $16.892^{+4.04}_{-0.71}$  | $0.342^{+0.47}_{-0.18}$ | $149.137^{+9.01}_{-5.91}$   | $10.112^{+8.03}_{-0.07}$ | [266]                | $797^{+25}_{-188}$             |
|           |                     | L <sub>*</sub> Gal.   | -                         | -                         | -                       | -                           | [0.03]                   | $16^{+8}_{-2}$       | $138^{+60}_{-47}$              |
| MACS1621  | 245.3531358,        | DM H1                 | $0.866^{+0.33}_{-0.73}$   | $-0.955^{+0.67}_{-0.27}$  | $0.702^{+0.06}_{-0.04}$ | $42.607^{+0.73}_{-0.72}$    | $4.013^{+2.05}_{-0.08}$  | [247]                | $943^{+13}_{-19}$              |
|           | 38.1691253          | Gal. H2               | [0.0334]                  | [0.003]                   | $0.241^{+0.18}_{-0.16}$ | $53.732^{+0.54}_{-18.78}$   | $0.076^{+1.45}_{-0.47}$  | [19]                 | $164^{+286}_{-39}$             |
|           |                     | Gal. H3               | [28.768]                  | [-5.684]                  | $0.391^{+0.48}_{-0.17}$ | [47.286]                    | $1.479^{+0.01}_{-1.22}$  | [47]                 | $82^{+73}_{-58}$               |
|           |                     | L <sub>*</sub> Gal.   | -                         | -                         | -                       | -                           | [0.02]                   | $17^{+1}_{-8}$       | $179^{+24}_{-5}$               |
| RCS0327   | 51.863234,          | DM H1                 | $2.930^{+0.46}_{-0.04}$   | $-4.042^{+0.12}_{-0.10}$  | $0.455^{+0.01}_{-0.01}$ | $13.577^{+0.58}_{-0.11}$    | $13.199^{+0.00}_{-0.76}$ | [224]                | $1062^{+12}_{-2}$              |
|           | -13.439644          | DM H2                 | $-0.278^{+0.39}_{-0.20}$  | $0.767^{+0.08}_{-0.41}$   | $0.570^{+0.01}_{-0.05}$ | $166.598^{+1.62}_{-5.02}$   | $4.241^{+0.90}_{-0.57}$  | $20^{+7}_{-1}$       | $581^{+23}_{-22}$              |
|           |                     | Gal. H3               | [9.342]                   | [9.270]                   | [0.539]                 | [63.30]                     | [0.01]                   | [2]                  | $27^{+10}_{-10}$               |
|           |                     | Gal. H4               | $19.804^{+0.65}_{-0.02}$  | $1.912^{+0.48}_{-1.55}$   | $0.817^{+0.07}_{-0.01}$ | $56.672^{+6.59}_{-1.47}$    | $0.629^{+0.11}_{-0.42}$  | $64^{+10}_{-8}$      | $229^{+20}_{-2}$               |
|           |                     | Gal. H5               | [-0.802]                  | [11.236]                  | [0.335]                 | [7.700]                     | $0.315^{+0.36}_{-0.17}$  | $4^{+7}_{-0.4}$      | $171^{+6}_{-22}$               |
|           |                     | Gal. H6               | [-10.7924]                | [3.9450]                  | [0]                     | [0]                         | $4.806^{+2.35}_{-0.56}$  | $38^{+4}_{-23}$      | $198^{+18}_{-72}$              |
|           |                     | Gal. H7               | [8.606]                   | [7.557]                   | [0.223]                 | [163.436]                   | $0.053^{+0.12}_{-0.02}$  | $2^{+4.0}_{-0.1}$    | $101^{+1}_{-28}$               |
|           | L <sub>*</sub> Gal. | -                     | -                         | -                         | -                       | [0.02]                      | $3^{+0.1}_{-1.0}$        | $201^{+28}_{-4}$     |                                |
| MACS2129  | 322.35878,          | DM H1                 | $0.955^{+0.63}_{-0.22}$   | $0.281^{+0.09}_{-0.62}$   | $0.626^{+0.03}_{-0.00}$ | $170.640^{+0.07}_{-1.34}$   | $15.153^{+0.45}_{-0.84}$ | [146]                | $1111^{+16}_{-14}$             |
|           | -7.6909965          | BCG H2                | [-0.071]                  | [-0.208]                  | [0.315]                 | [5.3]                       | [0]                      | $7^{+2}_{-5}$        | $295^{+49}_{-4}$               |
|           |                     | Gal. H3               | [-2.925]                  | [0.809]                   | [0.441]                 | [70]                        | [0.1]                    | $1^{+8}_{-1}$        | $212^{+27}_{-44}$              |
|           |                     | Gal. H4               | [4.531]                   | [-1.278]                  | [0.273]                 | [-31.6]                     | [0.113]                  | $5^{+2}_{-1}$        | $177^{+28}_{-10}$              |
|           |                     | Gal. H5               | [14.417]                  | [7.235]                   | [0.467]                 | [4.6]                       | [0.113]                  | $1^{+4}_{-1}$        | $337^{+21}_{-74}$              |
|           |                     | DM H6                 | $-42.358^{+0.12}_{-2.29}$ | $20.359^{+1.21}_{-1.02}$  | $0.798^{+0.01}_{-0.30}$ | $61.872^{+4.42}_{-5.98}$    | $18.086^{+4.49}_{-2.94}$ | [75]                 | $565^{+21}_{-43}$              |
|           |                     | Gal. H7               | [5.922]                   | [6.840]                   | [0.394]                 | [88.5]                      | [0.113]                  | $10^{+3}_{-1}$       | $227^{+17}_{-5}$               |

Table 6 continued

Table 6 (continued)

| Cluster | REF.        | Object  | $\Delta\alpha$ (")                        | $\Delta\delta$ (")                        | $\epsilon$                              | $\theta$ (°)                                | $r_{\text{core}}$ (")                    | $r_{\text{cut}}$ (")            | $\sigma$ (km s <sup>-1</sup> )      |
|---------|-------------|---------|---|---|---|---|--|---------------------------------|-------------------------------------|
|         |             | L* Gal. | –   | –   | –                                       | –   | [0.02]                                   | 11 <sup>+1</sup> <sub>-1</sub>  | 253 <sup>+2</sup> <sub>-20</sub>    |
| PSZ1G09 | 277.787803, | DM H1   | -10.363 <sup>+0.95</sup> <sub>-0.98</sub> | 7.942 <sup>+0.97</sup> <sub>-0.49</sub>   | 0.530 <sup>+0.02</sup> <sub>-0.06</sub> | 103.759 <sup>+1.29</sup> <sub>-0.01</sub>   | 26.313 <sup>+0.04</sup> <sub>-0.34</sub> | [192]                           | 1102 <sup>+34</sup> <sub>-3</sub>   |
|         | 62.249099   | BCG H2  | [0.]                                      | [0.]                                      | 0.364 <sup>+0.05</sup> <sub>-0.09</sub> | 35.860 <sup>+9.34</sup> <sub>-1.15</sub>    | 0.213 <sup>+0.04</sup> <sub>-0.07</sub>  | 7 <sup>+1</sup> <sub>-1</sub>   | 210 <sup>+6</sup> <sub>-11</sub>    |
|         |             | DM H3   | [-47.869]                                 | [14.742]                                  | [0.]                                    | [0.]  | 19.389 <sup>+0.89</sup> <sub>-5.20</sub> | [192]                           | 879 <sup>+1</sup> <sub>-104</sub>   |
|         |             | DM H4   | 3.432 <sup>+0.44</sup> <sub>-0.14</sub>   | -10.522 <sup>+0.36</sup> <sub>-1.00</sub> | 0.711 <sup>+0.05</sup> <sub>-0.04</sub> | 113.380 <sup>+1.65</sup> <sub>-1.02</sub>   | 14.865 <sup>+1.31</sup> <sub>-0.41</sub> | [192]                           | 692 <sup>+30</sup> <sub>-21</sub>   |
|         |             | Gal. H5 | [3.487]                                   | [0.417]                                   | 0.105 <sup>+0.01</sup> <sub>-0.02</sub> | 89.580 <sup>+58.24</sup> <sub>-5.96</sub>   | 0.024 <sup>+0.10</sup> <sub>-0.01</sub>  | 1 <sup>+0</sup> <sub>-0</sub>   | 157 <sup>+41</sup> <sub>-53</sub>   |
|         |             | L* .    | –   | –   | –                                       | –   | [0.02]                                   | 10 <sup>+1</sup> <sub>-0</sub>  | 83 <sup>+8</sup> <sub>-2</sub>      |
| RX0152  | 28.1829389, | DM H1   | 4.767 <sup>+1.06</sup> <sub>-1.99</sub>   | 7.623 <sup>+0.35</sup> <sub>-2.08</sub>   | 0.494 <sup>+0.21</sup> <sub>-0.06</sub> | -18.949 <sup>+11.16</sup> <sub>-20.95</sub> | 6.626 <sup>+3.98</sup> <sub>-5.39</sub>  | [197]                           | 538 <sup>+148</sup> <sub>-109</sub> |
|         | -13.9554946 | L* Gal. | –   | –   | –                                       | –   | [0.02]                                   | 18 <sup>+1</sup> <sub>-2</sub>  | 356 <sup>+19</sup> <sub>-43</sub>   |
| SPT0516 | 79.246251,  | DM H1   | 5.365 <sup>+0.10</sup> <sub>-0.33</sub>   | 12.963 <sup>+0.51</sup> <sub>-0.73</sub>  | 0.352 <sup>+0.00</sup> <sub>-0.06</sub> | 90.517 <sup>+2.12</sup> <sub>-2.82</sub>    | 12.787 <sup>+2.12</sup> <sub>-0.39</sub> | [183]                           | 931 <sup>+57</sup> <sub>-20</sub>   |
|         | -57.918573  | DM H2   | -5.831 <sup>+0.43</sup> <sub>-0.07</sub>  | -7.566 <sup>+0.0</sup> <sub>-1.97</sub>   | 0.513 <sup>+0.12</sup> <sub>-0.02</sub> | 114.768 <sup>+7.58</sup> <sub>-5.56</sub>   | 4.979 <sup>+0.83</sup> <sub>-0.77</sub>  | 43 <sup>+15</sup> <sub>-5</sub> | 424 <sup>+8</sup> <sub>-53</sub>    |
|         |             | Gal. H3 | -0.728 <sup>+0.19</sup> <sub>-0.18</sub>  | 0.099 <sup>+0.32</sup> <sub>-0.04</sub>   | 0.709 <sup>+0.02</sup> <sub>-0.16</sub> | 40.866 <sup>+0.01</sup> <sub>-15.47</sub>   | 0.021 <sup>+0.09</sup> <sub>-0.00</sub>  | 28 <sup>+5</sup> <sub>-0</sub>  | 180 <sup>+7</sup> <sub>-18</sub>    |
|         |             | L* Gal. | –   | –   | –                                       | –   | –  | [0.02]                          | 16 <sup>+1</sup> <sub>-4</sub>      |
| SPT2011 | 302.781449, | DM H1   | 5.037 <sup>+0.70</sup> <sub>-0.34</sub>   | 3.814 <sup>+0.31</sup> <sub>-0.11</sub>   | 0.070 <sup>+0.01</sup> <sub>-0.00</sub> | 57.036 <sup>+0.06</sup> <sub>-7.78</sub>    | 17.269 <sup>+5.36</sup> <sub>-2.04</sub> | [179]                           | 1375 <sup>+209</sup> <sub>-56</sub> |
|         | -52.471004  | DM H2   | -6.768 <sup>+2.18</sup> <sub>-4.61</sub>  | -8.403 <sup>+1.80</sup> <sub>-0.78</sub>  | 0.646 <sup>+0.04</sup> <sub>-0.25</sub> | 46.813 <sup>+10.06</sup> <sub>-4.55</sub>   | 10.340 <sup>+1.83</sup> <sub>-0.45</sub> | 48 <sup>+8</sup> <sub>-2</sub>  | 491 <sup>+76</sup> <sub>-42</sub>   |
|         |             | DM H3   | [-11.234]                                 | [-6.426]                                  | 0.665 <sup>+0.09</sup> <sub>-0.02</sub> | 124.752 <sup>+6.24</sup> <sub>-16.09</sub>  | 8.689 <sup>+0.38</sup> <sub>-0.82</sub>  | 19 <sup>+25</sup> <sub>-6</sub> | 285 <sup>+45</sup> <sub>-11</sub>   |
|         |             | L* Gal. | –   | –   | –                                       | –   | –  | [0.02]                          | 15 <sup>+2</sup> <sub>-1</sub>      |

NOTE—Parameters for the best-fit models of all clusters modeled with `Lenstool`.  $\Delta\alpha$ . and  $\Delta\delta$  are defined in relation to the BCG of the clusters, the coordinates of which are given in the REF. column, where the RA is given in the first row and the Dec. is given in the second row. Position angles are measured north of west, and the ellipticity  $\epsilon$  is defined as  $(a^2 - b^2)/(a^2 + b^2)$ . Error bars correspond to the  $1\sigma$  confidence level. Non-optimized values are indicated by brackets. Cluster names are abbreviated in this table for readability. The designations for individual potentials associated with a cluster-scale dark matter halo (DM), the BCG, or a galaxy-scale mass halo (Gal.) are abbreviated as H1, H2, etc.

Table 7. List of multiple images

| ID       | R.A.<br>J2000 | Decl.<br>J2000 | $z$   | $z_{\text{spec}}$<br>Reference | Notes |
|----------|---------------|----------------|-------|--------------------------------|-------|
| Abell 68 |               |                |       |                                |       |
| 1.1.1    | 9.280833      | 9.157894       | 1.600 | Richard et al. (2007)          |       |
| 1.1.2    | 9.280398      | 9.156651       |       |                                |       |
| 1.1.3    | 9.2755277     | 9.1524037      |       |                                |       |
| 1.2.1    | 9.2804222     | 9.1582902      |       |                                |       |
| 1.2.2    | 9.2798639     | 9.1568091      |       |                                |       |
| 1.2.3    | 9.2747681     | 9.1528177      |       |                                |       |
| 2.1.1    | 9.2811551     | 9.1609147      | 1.583 | Richard et al. (2007)          |       |
| 2.1.2    | 9.2768184     | 9.1568752      |       |                                |       |
| 2.1.3    | 9.2756267     | 9.1547914      |       |                                |       |
| 2.2.1    | 9.2812803     | 9.1610266      |       |                                |       |
| 2.2.2    | 9.2767501     | 9.1566571      |       |                                |       |
| 2.2.3    | 9.2758399     | 9.1550114      |       |                                |       |
| 3.1.1    | 9.2735876     | 9.1667299      | 5.421 | Richard et al. (2007)          |       |
| 3.1.2    | 9.2702008     | 9.1643861      |       |                                |       |
| 3.1.3    | 9.2678101     | 9.1620116      |       |                                |       |

Table 7 continued



Table 7 (continued)

| ID     | R.A.<br>J2000 | Decl.<br>J2000 | $z$                     | $z_{spec}$<br>Reference | Notes |
|--------|---------------|----------------|-------------------------|-------------------------|-------|
| 4.1.1  | 9.2789663     | 9.1593152      | $1.413^{+0.02}_{-0.08}$ |                         |       |
| 4.1.2  | 9.2778949     | 9.1586256      |                         |                         |       |
| 4.1.3  | 9.2740603     | 9.1536464      |                         |                         |       |
| 5.1.1  | 9.2717546     | 9.1659809      | 2.689                   | Richard et al. (2007)   |       |
| 5.1.2  | 9.2695335     | 9.1643621      |                         |                         |       |
| 5.1.3  | 9.2688970     | 9.1638078      |                         |                         |       |
| 6.1.1  | 9.2803624     | 9.1623110      | $2.380^{+0.31}_{-0.03}$ |                         |       |
| 6.1.2  | 9.2751285     | 9.1576863      |                         |                         |       |
| 6.1.3  | 9.2733581     | 9.1552036      |                         |                         |       |
| 7.1.1  | 9.2708859     | 9.1746921      | $5.890^{+0.01}_{-0.68}$ |                         |       |
| 7.1.2  | 9.2667435     | 9.1717768      |                         |                         |       |
| 7.1.3  | 9.2630784     | 9.1706364      |                         |                         |       |
| 8.1.1  | 9.2703232     | 9.1747891      | $2.694^{+0.11}_{-0.22}$ |                         |       |
| 8.1.2  | 9.2652996     | 9.1714227      |                         |                         |       |
| 8.1.3  | 9.2639542     | 9.1713205      |                         |                         |       |
| 9.1.1  | 9.2842303     | 9.1567185      | $3.985^{+0.00}_{-0.51}$ |                         |       |
| 9.1.2  | 9.2828687     | 9.1534580      |                         |                         |       |
| 9.1.3  | 9.2805242     | 9.1511926      |                         |                         |       |
| 10.1.1 | 9.2788946     | 9.1598966      | $2.466^{+0.28}_{-0.15}$ |                         |       |
| 10.1.2 | 9.2782120     | 9.1594081      |                         |                         |       |
| 10.1.3 | 9.2725146     | 9.1530888      |                         |                         |       |
| 11.1.1 | 9.2827857     | 9.1582672      | 3.135                   | Richard et al. (2007)   |       |
| 11.1.2 | 9.2816335     | 9.1555403      |                         |                         |       |
| 11.1.3 | 9.2761537     | 9.1509177      |                         |                         |       |
| 12.1.1 | 9.2687562     | 9.1746462      | $3.639^{+0.51}_{-0.37}$ |                         |       |
| 12.1.2 | 9.2685146     | 9.1741565      |                         |                         |       |
| 12.1.3 | 9.2621883     | 9.1709687      |                         |                         |       |

RXC J0232.2–4420

|       |           |            |                         |  |  |
|-------|-----------|------------|-------------------------|--|--|
| 1.1.1 | 38.068580 | -44.339061 | $1.549^{+0.06}_{-0.06}$ |  |  |
| 1.1.2 | 38.078533 | -44.347577 |                         |  |  |
| 1.1.3 | 38.080421 | -44.348048 |                         |  |  |
| 2.1.1 | 38.059882 | -44.350331 | $5.902^{+0.06}_{-1.07}$ |  |  |
| 2.1.2 | 38.060422 | -44.351186 |                         |  |  |
| 3.1.1 | 38.074925 | -44.346648 | $2.324^{+0.30}_{-0.01}$ |  |  |
| 3.1.2 | 38.075806 | -44.346568 |                         |  |  |
| 3.1.3 | 38.083445 | -44.354338 |                         |  |  |
| 3.1.4 | 38.080452 | -44.341404 |                         |  |  |
| 3.1.5 | 38.074558 | -44.340086 |                         |  |  |

Table 7 continued

Table 7 (continued)

| ID    | R.A.<br>J2000 | Decl.<br>J2000 | $z$                                     | $z_{spec}$<br>Reference | Notes |
|-------|---------------|----------------|---|-------------------------|-------|
| 4.1.1 | 38.063653     | -44.345115     | 1.473 <sup>+0.02</sup> <sub>-0.07</sub> |                         |       |
| 4.1.2 | 38.063474     | -44.345851     |   |                         |       |
| 4.1.3 | 38.063408     | -44.347079     |   |                         |       |
| 4.1.4 | 38.068204     | -44.353601     |   |                         |       |
| 5.1.1 | 38.069032     | -44.340911     | 1.645                                   | Mainali (2019)          |       |
| 5.1.2 | 38.067245     | -44.348830     |   |                         |       |
| 5.1.3 | 38.076868     | -44.353985     |   |                         |       |
| 5.1.4 | 38.081248     | -44.345429     |   |                         |       |
| 6.1.1 | 38.069596     | -44.339507     | 1.749 <sup>+0.12</sup> <sub>-0.00</sub> |                         |       |
| 6.1.2 | 38.068818     | -44.349680     |   |                         |       |
| 6.1.3 | 38.077894     | -44.353268     |   |                         |       |
| 6.1.4 | 38.083099     | -44.346552     |   |                         |       |
| 7.1.1 | 38.102283     | -44.340004     | 1.467                                   | Mainali (2019)          |       |
| 7.1.2 | 38.101758     | -44.341137     |   |                         |       |
| 7.1.3 | 38.102921     | -44.341632     |   |                         |       |
| 7.1.4 | 38.102983     | -44.341092     |   |                         |       |

## SMACS J2031.8–4036

|       |            |            |        |                       |  |        |                       |  |
|-------|------------|------------|--------|-----------------------|--|--------|-----------------------|--|
| 1.1.1 | 307.970430 | -40.625675 | 3.5077 | Richard et al. (2021) |  |        |                       |  |
| 1.1.2 | 307.970811 | -40.625666 |        |                       |  |        |                       |  |
| 1.1.3 | 307.971084 | -40.629384 |        |                       |  |        |                       |  |
| 1.1.4 | 307.974304 | -40.627781 |        |                       |  |        |                       |  |
| 1.1.5 | 307.974701 | -40.618324 |        |                       |  |        |                       |  |
| 1.2.3 | 307.971054 | -40.629326 |        |                       |  |        |                       |  |
| 1.2.4 | 307.974242 | -40.627794 |        |                       |  |        |                       |  |
| 1.3.3 | 307.970980 | -40.629291 |        |                       |  |        |                       |  |
| 1.3.4 | 307.974187 | -40.627789 |        |                       |  |        |                       |  |
| 1.4.1 | 307.970271 | -40.625712 |        |                       |  |        |                       |  |
| 1.4.2 | 307.970890 | -40.625693 |        |                       |  |        |                       |  |
| 1.5.1 | 307.970124 | -40.625734 |        |                       |  |        |                       |  |
| 1.5.2 | 307.970998 | -40.625703 |        |                       |  |        |                       |  |
| 2.1.1 | 307.969785 | -40.625190 |        |                       |  | 3.5077 | Richard et al. (2021) |  |
| 2.1.3 | 307.970456 | -40.630080 |        |                       |  |        |                       |  |
| 2.1.4 | 307.974965 | -40.627433 |        |                       |  |        |                       |  |
| 2.1.5 | 307.974611 | -40.619106 |        |                       |  |        |                       |  |
| 3.1.1 | 307.968870 | -40.626091 | 5.6231 | Richard et al. (2021) |  |        |                       |  |
| 3.1.2 | 307.971415 | -40.625912 |        |                       |  |        |                       |  |
| 3.1.3 | 307.970076 | -40.629100 |        |                       |  |        |                       |  |
| 3.1.4 | 307.973875 | -40.627797 |        |                       |  |        |                       |  |

Table 7 continued

Table 7 (continued)

| ID     | R.A.<br>J2000 | Decl.<br>J2000 | $z$                     | $z_{spec}$<br>Reference | Notes |
|--------|---------------|----------------|-------------------------|-------------------------|-------|
| 3.1.5  | 307.974076    | -40.616935     |                         |                         |       |
| 4.1.1  | 307.967266    | -40.624978     | 3.3400                  | Richard et al. (2021)   |       |
| 4.1.2  | 307.967502    | -40.629310     |                         |                         |       |
| 4.1.3  | 307.972504    | -40.618556     |                         |                         |       |
| 5.1.1  | 307.962191    | -40.626671     | 3.7230                  | Richard et al. (2021)   |       |
| 5.1.2  | 307.962981    | -40.624008     |                         |                         |       |
| 5.1.3  | 307.967191    | -40.617338     |                         |                         |       |
| 6.1.1  | 307.964474    | -40.621845     | 1.4249                  | Richard et al. (2021)   |       |
| 6.1.2  | 307.963829    | -40.622961     |                         |                         |       |
| 6.1.3  | 307.963235    | -40.623975     |                         |                         |       |
| 7.1.1  | 307.970140    | -40.618343     | 5.2397                  | Richard et al. (2021)   |       |
| 7.1.2  | 307.966525    | -40.623373     |                         |                         |       |
| 7.1.3  | 307.965493    | -40.629880     |                         |                         |       |
| 8.1.1  | 307.965651    | -40.619021     | 5.6128                  | Richard et al. (2021)   |       |
| 8.1.2  | 307.964631    | -40.620507     |                         |                         |       |
| 8.1.3  | 307.961211    | -40.628841     |                         |                         |       |
| 9.1.1  | 307.963306    | -40.620319     | 6.4085                  | Richard et al. (2021)   |       |
| 9.1.2  | 307.964655    | -40.618320     |                         |                         |       |
| 10.1.1 | 307.967560    | -40.619973     | 3.8561                  | Richard et al. (2021)   |       |
| 10.1.2 | 307.966840    | -40.620941     |                         |                         |       |
| 10.1.3 | 307.963441    | -40.629438     |                         |                         |       |
| 10.2.1 | 307.967467    | -40.620069     |                         |                         |       |
| 10.2.2 | 307.966874    | -40.620820     |                         |                         |       |
| 11.1.1 | 307.967944    | -40.629967     | 2.2556                  | Richard et al. (2021)   |       |
| 11.1.2 | 307.968403    | -40.623989     |                         |                         |       |
| 11.1.3 | 307.971923    | -40.620533     |                         |                         |       |
| 11.1.4 | 307.973291    | -40.625414     |                         |                         |       |
| 11.2.1 | 307.968026    | -40.629999     |                         |                         |       |
| 11.2.2 | 307.968470    | -40.623994     |                         |                         |       |
| 11.2.3 | 307.972006    | -40.620555     |                         |                         |       |
| 11.2.4 | 307.973504    | -40.625448     |                         |                         |       |
| 12.1.1 | 307.973569    | -40.625071     | 3.4140                  | Richard et al. (2021)   |       |
| 12.1.2 | 307.972630    | -40.625049     |                         |                         |       |
| 12.1.3 | 307.968618    | -40.623199     |                         |                         |       |
| 12.1.4 | 307.971400    | -40.620672     |                         |                         |       |
| 12.1.5 | 307.967336    | -40.630901     |                         |                         |       |
| 13.1.1 | 307.968342    | -40.618096     | 4.7300                  | Richard et al. (2021)   |       |
| 13.1.2 | 307.965065    | -40.623021     |                         |                         |       |
| 13.1.3 | 307.963477    | -40.628684     |                         |                         |       |
| 14.1.1 | 307.965657    | -40.624813     | $1.604^{+0.03}_{-0.04}$ |                         |       |

Table 7 continued



Table 7 (continued)

| ID                | R.A.<br>J2000 | Decl.<br>J2000 | $z$                     | $z_{spec}$<br>Reference | Notes |
|-------------------|---------------|----------------|-------------------------|-------------------------|-------|
| 14.1.2            | 307.965245    | -40.626385     |                         |                         |       |
| 15.1.1            | 307.964186    | -40.626310     | $6.893^{+0.08}_{-0.20}$ |                         |       |
| 15.1.2            | 307.964164    | -40.626570     |                         |                         |       |
| MACS J0027.8+2616 |               |                |                         |                         |       |
| 1.1.1             | 6.936236      | 26.274556      | 3.1267                  | This work, MUSE         |       |
| 1.1.2             | 6.938848      | 26.268583      |                         |                         |       |
| 1.1.3             | 6.942843      | 26.274449      |                         |                         |       |
| 1.1.4             | 6.939522      | 26.278502      |                         |                         |       |
| 1.2.1             | 6.936217      | 26.274369      |                         |                         |       |
| 1.2.2             | 6.938797      | 26.268650      |                         |                         |       |
| 1.2.3             | 6.942850      | 26.274421      |                         |                         |       |
| 1.2.4             | 6.939509      | 26.278536      |                         |                         |       |
| 1.3.1             | 6.936158      | 26.273721      |                         |                         |       |
| 1.3.2             | 6.938467      | 26.268934      |                         |                         |       |
| 1.3.3             | 6.942782      | 26.274284      |                         |                         |       |
| 1.3.4             | 6.939322      | 26.278602      |                         |                         |       |
| 1.4.1             | 6.936253      | 26.274864      |                         |                         |       |
| 1.4.2             | 6.938879      | 26.268495      |                         |                         |       |
| 1.4.3             | 6.942814      | 26.274491      |                         |                         |       |
| 1.4.4             | 6.939490      | 26.278434      |                         |                         |       |
| 1.5.1             | 6.936227      | 26.273358      |                         |                         |       |
| 1.5.2             | 6.938406      | 26.269068      |                         |                         |       |
| 1.5.3             | 6.942842      | 26.274233      |                         |                         |       |
| 1.5.4             | 6.939418      | 26.278711      |                         |                         |       |
| 2.1.1             | 6.947640      | 26.274558      | $5.639^{+0.21}_{-0.54}$ |                         |       |
| 2.1.2             | 6.946998      | 26.276859      |                         |                         |       |
| 2.1.3             | 6.946939      | 26.277012      |                         |                         |       |
| 2.2.2             | 6.946946      | 26.276888      | $3.573^{+1.71}_{-0.33}$ |                         |       |
| 2.2.3             | 6.946902      | 26.276983      |                         |                         |       |
| 3.1.1             | 6.941260      | 26.277969      | 4.45                    | This work, MUSE         |       |
| 3.1.2             | 6.937722      | 26.276142      |                         |                         |       |
| 3.1.3             | 6.940009      | 26.266777      |                         |                         |       |
| 4.1.1             | 6.946621      | 26.273450      | $4.411^{+0.17}_{-0.33}$ |                         |       |
| 4.1.2             | 6.946658      | 26.276252      |                         |                         |       |
| 4.1.3             | 6.945298      | 26.277877      |                         |                         |       |
| c5.1.1            | 6.937108      | 26.273139      | ...                     |                         |       |

Table 7 continued

Table 7 (continued)

| ID               | R.A.<br>J2000 | Decl.<br>J2000 | $z$                     | $z_{spec}$<br>Reference | Notes |
|------------------|---------------|----------------|-------------------------|-------------------------|-------|
| c5.1.2           | 6.940155      | 26.268576      |                         |                         |       |
| c5.1.3           | 6.944855      | 26.272580      |                         |                         |       |
| c5.1.4           | 6.941673      | 26.279653      |                         |                         |       |
| c5.2.1           | 6.937048      | 26.273066      |                         |                         |       |
| c5.2.2           | 6.940033      | 26.268586      |                         |                         |       |
| c5.2.3           | 6.944899      | 26.272698      |                         |                         |       |
| c5.2.4           | 6.941504      | 26.279663      |                         |                         |       |
| c5.3.1           | 6.936962      | 26.272928      |                         |                         |       |
| c5.3.2           | 6.939858      | 26.268637      |                         |                         |       |
| c5.3.3           | 6.944925      | 26.272887      |                         |                         |       |
| c5.3.4           | 6.941269      | 26.279685      |                         |                         |       |
| c6.1.1           | 6.938385      | 26.277879      | ...                     |                         |       |
| c6.1.2           | 6.937572      | 26.277232      |                         |                         |       |
| RXC J2211.7–0349 |               |                |                         |                         |       |
| 1.1.1            | 332.939988    | -3.824111      | 1.051                   | Cerny et al. (2018)     |       |
| 1.1.2            | 332.933020    | -3.828870      |                         |                         |       |
| 1.1.3            | 332.938466    | -3.834306      |                         |                         |       |
| 1.1.4            | 332.952310    | -3.831273      |                         |                         |       |
| 1.1.5            | 332.940787    | -3.829024      |                         |                         |       |
| 1.2.1            | 332.939878    | -3.824069      |                         |                         |       |
| 1.2.2            | 332.933097    | -3.828766      |                         |                         |       |
| 1.2.3            | 332.938458    | -3.834198      |                         |                         |       |
| 1.2.4            | 332.952372    | -3.831187      |                         |                         |       |
| 1.2.5            | 332.940817    | -3.829081      |                         |                         |       |
| 2.1.1            | 332.931052    | -3.836624      | $2.118^{+0.17}_{-0.03}$ |                         |       |
| 2.1.2            | 332.934371    | -3.839186      |                         |                         |       |
| 2.1.3            | 332.953426    | -3.838235      |                         |                         |       |
| 2.2.1            | 332.931118    | -3.836431      | $2.147^{+0.13}_{-0.03}$ |                         |       |
| 2.2.2            | 332.934346    | -3.838963      |                         |                         |       |
| 2.2.3            | 332.953637    | -3.837944      |                         |                         |       |
| 3.1.1            | 332.931464    | -3.836102      | $2.127^{+0.18}_{-0.03}$ |                         |       |
| 3.1.2            | 332.934020    | -3.838213      |                         |                         |       |
| 3.1.3            | 332.954336    | -3.837149      |                         |                         |       |
| 4.1.1            | 332.937135    | -3.819198      | $5.486^{+1.10}_{-0.15}$ |                         |       |
| 4.1.2            | 332.929179    | -3.827742      |                         |                         |       |
| 4.1.3            | 332.936399    | -3.837133      |                         |                         |       |
| 4.1.4            | 332.958469    | -3.830820      |                         |                         |       |
| 4.1.5            | 332.940120    | -3.829443      |                         |                         |       |

Table 7 continued

Table 7 (continued)

| ID                | R.A.<br>J2000 | Decl.<br>J2000 | $z$                                     | $z_{spec}$<br>Reference | Notes |  |
|-------------------|---------------|----------------|---|-------------------------|-------|--|
| 4.2.1             | 332.936857    | -3.819544      | 5.441 <sup>+0.95</sup> <sub>-0.08</sub> |                         |       |  |
| 4.2.2             | 332.929373    | -3.828174      |   |                         |       |  |
| 4.2.3             | 332.936125    | -3.837047      |   |                         |       |  |
| 4.2.4             | 332.958598    | -3.831044      |   |                         |       |  |
| 5.1.1             | 332.940664    | -3.811824      | 5.750 <sup>+1.20</sup> <sub>-0.41</sub> |                         |       |  |
| 5.1.2             | 332.937780    | -3.812058      |   |                         |       |  |
| 5.1.3             | 332.954644    | -3.817226      |   |                         |       |  |
| 6.1.1             | 332.929703    | -3.840415      | 1.854 <sup>+0.16</sup> <sub>-0.05</sub> |                         |       |  |
| 6.1.2             | 332.941603    | -3.844585      |   |                         |       |  |
| 6.1.3             | 332.943154    | -3.844507      |   |                         |       |  |
| 7.1.1             | 332.931384    | -3.837458      | 2.761 <sup>+0.24</sup> <sub>-0.00</sub> |                         |       |  |
| 7.1.2             | 332.933528    | -3.838877      |   |                         |       |  |
| 7.1.3             | 332.954729    | -3.837951      |   |                         |       |  |
| 8.1.1             | 332.938615    | -3.822329      | 3.095 <sup>+0.43</sup> <sub>-0.10</sub> |                         |       |  |
| 8.1.2             | 332.930927    | -3.833218      |   |                         |       |  |
| 8.1.3             | 332.934065    | -3.836824      |   |                         |       |  |
| 8.1.4             | 332.957495    | -3.833822      |   |                         |       |  |
| 9.1.1             | 332.937813    | -3.826374      | 2.179 <sup>+0.17</sup> <sub>-0.17</sub> |                         |       |  |
| 9.1.2             | 332.938254    | -3.827022      |   |                         |       |  |
| 10.1.1            | 332.935926    | -3.829706      | 2.437 <sup>+0.02</sup> <sub>-0.27</sub> |                         |       |  |
| 10.1.2            | 332.936471    | -3.829518      |   |                         |       |  |
| MACS J0553.4–3342 |               |                |   |                         |       |  |
| 1.1.1             | 88.3658619    | -33.7044559    | 1.14                                    | Ebeling et al. (2017)   |       |  |
| 1.1.2             | 88.3661029    | -33.7085889    |   |                         |       |  |
| 1.1.3             | 88.3652219    | -33.7121889    |   |                         |       |  |
| 2.1.1             | 88.3599266    | -33.7154709    | 3.100 <sup>+0.03</sup> <sub>-0.03</sub> |                         |       |  |
| 2.1.2             | 88.3625462    | -33.7103277    |   |                         |       |  |
| 2.1.3             | 88.3607222    | -33.6978757    |   |                         |       |  |
| 2.2.1             | 88.3599012    | -33.7152936    |   |                         |       |  |
| 2.2.2             | 88.3624310    | -33.7104217    |   |                         |       |  |
| 2.2.3             | 88.3606585    | -33.6978104    |   |                         |       |  |
| 2.3.1             | 88.3599197    | -33.7150017    |   |                         |       |  |
| 2.3.2             | 88.3623173    | -33.7105328    |   |                         |       |  |
| 2.3.3             | 88.3606075    | -33.6977394    |   |                         |       |  |
| 2.4.1             | 88.3601530    | -33.7144632    |   |                         |       |  |
| 2.4.2             | 88.3621588    | -33.7107136    |   |                         |       |  |
| 2.4.3             | 88.3605699    | -33.6976552    |   |                         |       |  |
| 2.5.1             | 88.3601866    | -33.7141458    |   |                         |       |  |

Table 7 continued



Table 7 (continued)

| ID    | R.A.<br>J2000 | Decl.<br>J2000 | $z$   | $z_{spec}$<br>Reference | Notes                                     |
|-------|---------------|----------------|-------|-------------------------|---|
| 2.5.2 | 88.3618676    | -33.7109455    |       |                         |   |
| 2.6.1 | 88.3603537    | -33.7138338    |       |                         |   |
| 2.6.2 | 88.3617713    | -33.7111093    |       |                         |   |
| 2.7.1 | 88.3603793    | -33.7137162    |       |                         |   |
| 2.7.2 | 88.3616833    | -33.7112069    |       |                         |   |
| 3.1.1 | 88.3277452    | -33.7051380    | 1.243 | $^{+0.01}_{-0.01}$      |   |
| 3.1.2 | 88.3273078    | -33.7082501    |       |                         |   |
| 3.1.3 | 88.3274485    | -33.7092172    |       |                         |   |
| 3.2.1 | 88.3273359    | -33.7058549    |       |                         |   |
| 3.2.2 | 88.3269949    | -33.7076049    |       |                         |   |
| 3.2.3 | 88.3272749    | -33.7099219    |       |                         |   |
| 3.3.1 | 88.3274380    | -33.7065044    |       |                         |   |
| 3.3.2 | 88.3272339    | -33.7074439    |       |                         |   |
| 3.4.1 | 88.3264641    | -33.7069933    |       |                         |   |
| 3.4.2 | 88.3264287    | -33.7073152    |       |                         |   |
| 4.1.1 | 88.3280579    | -33.7005219    | 2.947 | $^{+0.04}_{-0.06}$      |   |
| 4.1.2 | 88.3248109    | -33.7084709    |       |                         |   |
| 4.1.3 | 88.3255309    | -33.7127209    |       |                         |   |
| 5.1.1 | 88.3340669    | -33.7085559    | 3.32  |                         | Ebeling et al. (2017) and this work, MUSE |
| 5.1.2 | 88.3330039    | -33.7149389    |       |                         |   |
| 5.1.3 | 88.3344089    | -33.6995059    |       |                         |   |
| 6.1.1 | 88.3392369    | -33.7022729    | 4.249 | $^{+0.07}_{-0.06}$      |   |
| 6.1.2 | 88.3388759    | -33.7060559    |       |                         |   |
| 6.1.3 | 88.3380129    | -33.7185729    |       |                         |   |
| 7.1.1 | 88.3367519    | -33.7082559    | 1.807 | $^{+0.01}_{-0.02}$      |   |
| 7.1.2 | 88.3358289    | -33.7133229    |       |                         |   |
| 7.1.3 | 88.3367729    | -33.7026899    |       |                         |   |
| 8.1.1 | 88.3586698    | -33.7195898    | 5.664 | $^{+0.15}_{-0.12}$      |   |
| 8.1.2 | 88.3623042    | -33.7077196    |       |                         |   |
| 8.1.3 | 88.3593580    | -33.6994796    |       |                         |   |
| 8.2.1 | 88.3588082    | -33.7196386    |       |                         |   |
| 8.2.2 | 88.3624804    | -33.7076777    |       |                         |   |
| 8.2.3 | 88.3596472    | -33.6995774    |       |                         |   |
| 8.3.1 | 88.3591336    | -33.7197891    |       |                         |   |
| 8.3.2 | 88.3628382    | -33.7075288    |       |                         |   |
| 8.3.3 | 88.3602558    | -33.6998207    |       |                         |   |
| 9.1.1 | 88.3430541    | -33.7144931    | 2.997 | $^{+0.04}_{-0.03}$      |   |
| 9.1.2 | 88.3434497    | -33.7096088    |       |                         |   |
| 9.1.3 | 88.3445746    | -33.6989433    |       |                         |   |
| 9.2.1 | 88.3430718    | -33.7143918    |       |                         |   |

Table 7 continued

Table 7 (continued)

| ID     | R.A.<br>J2000 | Decl.<br>J2000 | $z$   | $z_{spec}$<br>Reference | Notes |
|--------|---------------|----------------|-------|-------------------------|-------|
| 9.2.2  | 88.3434399    | -33.7096902    |       |                         |       |
| 9.2.3  | 88.3445769    | -33.6988883    |       |                         |       |
| 9.3.1  | 88.3431052    | -33.7143295    |       |                         |       |
| 9.3.2  | 88.3434448    | -33.7097594    |       |                         |       |
| 9.3.3  | 88.3446123    | -33.6988157    |       |                         |       |
| 9.4.1  | 88.3432159    | -33.7140456    |       |                         |       |
| 9.4.2  | 88.3434595    | -33.7100280    |       |                         |       |
| 9.4.3  | 88.3446996    | -33.6986979    |       |                         |       |
| 10.1.1 | 88.3404779    | -33.7158719    | 3.76  | This work, MUSE         |       |
| 10.1.2 | 88.3424669    | -33.6990669    |       |                         |       |
| 10.1.3 | 88.3410299    | -33.7092889    |       |                         |       |
| 11.1.1 | 88.3243083    | -33.7055700    | 1.910 | $^{+0.02}_{-0.03}$      |       |
| 11.1.2 | 88.3241319    | -33.7067226    |       |                         |       |
| 11.1.3 | 88.3242985    | -33.7112264    |       |                         |       |
| 12.1.1 | 88.3270548    | -33.7131277    | 7.219 | $^{+0.27}_{-0.09}$      |       |
| 12.1.2 | 88.3259715    | -33.7108159    |       |                         |       |
| 12.2.1 | 88.3269715    | -33.7129618    |       |                         |       |
| 12.2.2 | 88.3260084    | -33.7109352    |       |                         |       |
| 13.1.1 | 88.3421014    | -33.7123960    | 3.35  | This work, MUSE         |       |
| 13.1.2 | 88.3423039    | -33.7115470    |       |                         |       |
| 13.2.1 | 88.3420916    | -33.7122700    |       |                         |       |
| 13.2.2 | 88.3422705    | -33.7115781    |       |                         |       |
| 13.3.1 | 88.3421702    | -33.7121866    |       |                         |       |
| 13.3.2 | 88.3423138    | -33.7116370    |       |                         |       |
| 13.4.1 | 88.3422017    | -33.7120132    |       |                         |       |
| 13.4.2 | 88.3422803    | -33.7117351    |       |                         |       |
| 14.1.1 | 88.3692959    | -33.7043710    | 3.363 | $^{+0.10}_{-0.09}$      |       |
| 14.1.2 | 88.3696681    | -33.7057263    |       |                         |       |
| 15.1.1 | 88.3539066    | -33.7034301    |       |                         |       |
| 15.1.2 | 88.3529558    | -33.7065014    | 1.407 | $^{+0.01}_{-0.01}$      |       |
| 15.1.3 | 88.3540589    | -33.7156379    |       |                         |       |
| 16.1.1 | 88.3525536    | -33.6992058    | 4.570 | $^{+0.04}_{-0.03}$      |       |
| 16.1.2 | 88.3505162    | -33.7076583    |       |                         |       |
| 16.1.3 | 88.3523411    | -33.7190047    |       |                         |       |
| 17.1.1 | 88.3491110    | -33.7115478    | 3.485 | $^{+0.05}_{-0.09}$      |       |
| 17.1.2 | 88.3494206    | -33.7139235    |       |                         |       |
| 18.1.1 | 88.3506594    | -33.7107982    | 2.918 | $^{+0.04}_{-0.03}$      |       |
| 18.1.2 | 88.3514718    | -33.7144854    |       |                         |       |
| 18.1.3 | 88.3524087    | -33.6975770    |       |                         |       |
| 19.1.1 | 88.3557794    | -33.7135415    | 1.712 | $^{+0.04}_{-0.03}$      |       |

Table 7 continued

Table 7 (continued)

| ID                | R.A.<br>J2000 | Decl.<br>J2000 | $z$                     | $z_{spec}$<br>Reference | Notes               |
|-------------------|---------------|----------------|-------------------------|-------------------------|---------------------|
| 19.1.2            | 88.3548819    | -33.7103140    |                         |                         |                     |
| 20.1.1            | 88.3256409    | -33.7036986    | $3.045^{+0.05}_{-0.06}$ |                         |                     |
| 20.1.2            | 88.3252609    | -33.7044253    |                         |                         |                     |
| 21.1.1            | 88.3458228    | -33.7177558    | $3.745^{+0.06}_{-0.06}$ |                         |                     |
| 21.1.2            | 88.3449273    | -33.7077872    |                         |                         |                     |
| 21.1.3            | 88.3462092    | -33.6994610    |                         |                         |                     |
| MACS J0358.8–2955 |               |                |                         |                         |                     |
| 1.1.1             | 59.718226     | -29.923243     | 1.261                   | Hsu et al. (2013)       |                     |
| 1.1.2             | 59.728497     | -29.932040     |                         |                         |                     |
| 1.1.3             | 59.723055     | -29.927323     |                         |                         |                     |
| 2.1.1             | 59.719442     | -29.936392     | 3.07                    | Hsu et al. (2013)       |                     |
| 2.1.2             | 59.720636     | -29.936522     |                         |                         |                     |
| 3.1.1             | 59.719362     | -29.936607     | 3.07                    | Hsu et al. (2013)       |                     |
| 3.1.2             | 59.720356     | -29.936713     |                         |                         |                     |
| 4.1.1             | 59.712972     | -29.920461     | $2.437^{+0.06}_{-0.24}$ |                         |                     |
| 4.1.2             | 59.727946     | -29.930851     |                         |                         |                     |
| 4.1.3             | 59.725841     | -29.928688     |                         |                         |                     |
| 5.1.1             | 59.716309     | -29.921720     | $2.107^{+0.11}_{-0.08}$ |                         |                     |
| 5.1.2             | 59.730130     | -29.933371     |                         |                         |                     |
| 5.1.3             | 59.723680     | -29.926972     |                         |                         |                     |
| 6.1.1             | 59.713908     | -29.925562     | $1.570^{+0.08}_{-0.02}$ |                         |                     |
| 6.1.2             | 59.726937     | -29.935757     |                         |                         |                     |
| 6.1.3             | 59.720272     | -29.930026     |                         |                         |                     |
| MACS J1621.4+3810 |               |                |                         |                         |                     |
| 1.1.1             | 245.350738    | 38.168288      | $3.952^{+2.07}_{-1.30}$ |                         |                     |
| 1.1.2             | 245.351432    | 38.168379      |                         |                         |                     |
| 1.2.1             | 245.350885    | 38.168356      | $3.174^{+2.87}_{-0.57}$ |                         |                     |
| 1.2.2             | 245.351300    | 38.168401      |                         |                         |                     |
| 2.1.1             | 245.356333    | 38.166685      | [1.5]                   |                         | fixed at Photo- $z$ |
| 2.1.2             | 245.357710    | 38.173532      |                         |                         |                     |
| 2.1.3             | 245.349166    | 38.171773      |                         |                         |                     |
| 2.1.4             | 245.347364    | 38.165408      |                         |                         |                     |
| 2.2.1             | 245.356242    | 38.166394      |                         |                         |                     |
| 2.2.2             | 245.358219    | 38.173424      |                         |                         |                     |
| 2.2.3             | 245.349084    | 38.171462      |                         |                         |                     |
| 2.2.4             | 245.347807    | 38.165342      |                         |                         |                     |

Table 7 continued



Table 7 (continued)

| ID                       | R.A.<br>J2000 | Decl.<br>J2000 | $z$                                       | $z_{spec}$<br>Reference | Notes           |
|--------------------------|---------------|----------------|---|-------------------------|-----------------|
| 3.1.1                    | 245.360845    | 38.164155      | $1.295^{+0.13}_{-0.06}$                   |                         |                 |
| 3.1.2                    | 245.361585    | 38.164907      |   |                         |                 |
| 4.1.1                    | 245.351723    | 38.170133      | $1.306^{+0.04}_{-0.04}$                   |                         |                 |
| 4.1.2                    | 245.352504    | 38.169623      |   |                         |                 |
| 4.1.3                    | 245.357693    | 38.166126      |   |                         |                 |
| 4.1.4                    | 245.359653    | 38.171317      |   |                         |                 |
| 4.1.5                    | 245.350847    | 38.163867      |   |                         |                 |
| 5.1.1                    | 245.342426    | 38.168324      | $3.152^{+2.62}_{-0.69}$                   |                         |                 |
| 5.1.2                    | 245.342408    | 38.168421      |   |                         |                 |
| 5.1.3                    | 245.342542    | 38.168707      |   |                         |                 |
| RCS2 032727–132623       |               |                |   |                         |                 |
| 1.1                      | 51.867801     | -13.437960     | 1.7010                                    | Sharon et al. (2012)    | (Aa) Giant arc  |
| 1.2                      | 51.864738     | -13.435399     |   |                         | (Ab)            |
| 1.3                      | 51.860701     | -13.437034     |   |                         | (Ac)            |
| 1.4                      | 51.862555     | -13.448303     |   |                         | (counter image) |
| Clumps in the giant arcs |               |                |   |                         |                 |
| 1.01.3                   | 51.860580     | -13.438194     | 1-15: Clumps appearing only in images 3,4 |                         |                 |
| 1.01.4                   | 51.863845     | -13.448153     |   |                         |                 |
| 1.02.3                   | 51.860638     | -13.438243     |   |                         |                 |
| 1.02.4                   | 51.863931     | -13.448169     |   |                         |                 |
| 1.03.3                   | 51.860751     | -13.438207     |   |                         |                 |
| 1.03.4                   | 51.863957     | -13.448234     |   |                         |                 |
| 1.04.3                   | 51.860718     | -13.438137     |   |                         |                 |
| 1.04.4                   | 51.863864     | -13.448239     |   |                         |                 |
| 1.05.3                   | 51.860828     | -13.438147     |   |                         |                 |
| 1.05.4                   | 51.863927     | -13.448288     |   |                         |                 |
| 1.06.3                   | 51.860812     | -13.438045     |   |                         |                 |
| 1.06.4                   | 51.863810     | -13.448301     |   |                         |                 |
| 1.07.3                   | 51.860913     | -13.438025     |   |                         |                 |
| 1.07.4                   | 51.863817     | -13.448358     |   |                         |                 |
| 1.08.3                   | 51.860897     | -13.437855     |   |                         |                 |
| 1.08.4                   | 51.863621     | -13.448371     |   |                         |                 |
| 1.09.3                   | 51.860938     | -13.437870     |   |                         |                 |
| 1.09.4                   | 51.863633     | -13.448398     |   |                         |                 |
| 1.10.3                   | 51.861024     | -13.437777     |   |                         |                 |
| 1.10.4                   | 51.863544     | -13.448455     |   |                         |                 |
| 1.11.3                   | 51.861031     | -13.437717     |   |                         |                 |
| 1.11.4                   | 51.863465     | -13.448459     |   |                         |                 |

Table 7 continued

Table 7 (continued)

| ID     | R.A.<br>J2000 | Decl.<br>J2000 | $z$  | $z_{spec}$<br>Reference | Notes |
|--------|---------------|----------------|--|-------------------------|-------|
| 1.12.3 | 51.861062     | -13.437661     |  |                         |       |
| 1.12.4 | 51.863414     | -13.448484     |  |                         |       |
| 1.13.3 | 51.860945     | -13.437703     |  |                         |       |
| 1.13.4 | 51.863419     | -13.448412     |  |                         |       |
| 1.14.3 | 51.860915     | -13.437671     |  |                         |       |
| 1.14.4 | 51.863366     | -13.448396     |  |                         |       |
| 1.15.3 | 51.861038     | -13.437592     |  |                         |       |
| 1.15.4 | 51.863313     | -13.448479     |  |                         |       |
| 1.16.3 | 51.860867     | -13.437591     | Bright core of the east galaxy                                 |                         |       |
| 1.16.4 | 51.863216     | -13.448378     |  |                         |       |
| 1.16.5 | 51.863261     | -13.439496     | Demagnified central image                                      |                         |       |
| 1.16.6 | 51.860714     | -13.437493     | Added multiplicity in image 3 due to lensing by cluster member |                         |       |
| 1.17.1 | 51.867867     | -13.437154     | 17-19: extremely magnified region, not resolved in images 3,4  |                         |       |
| 1.17.2 | 51.867510     | -13.436689     |  |                         |       |
| 1.18.1 | 51.867995     | -13.437295     |  |                         |       |
| 1.18.2 | 51.867226     | -13.436358     |  |                         |       |
| 1.19.1 | 51.867750     | -13.437152     |  |                         |       |
| 1.19.2 | 51.867089     | -13.436406     |  |                         |       |
| 1.20.1 | 51.868096     | -13.437631     | 20-42: regions appearing in all 4 images                       |                         |       |
| 1.20.2 | 51.866481     | -13.435842     |  |                         |       |
| 1.20.3 | 51.860629     | -13.437397     |  |                         |       |
| 1.20.4 | 51.863030     | -13.448299     |  |                         |       |
| 1.21.1 | 51.868147     | -13.437756     |  |                         |       |
| 1.21.2 | 51.866251     | -13.435691     |  |                         |       |
| 1.21.3 | 51.860591     | -13.437404     |  |                         |       |
| 1.22.1 | 51.867937     | -13.437416     |  |                         |       |
| 1.22.2 | 51.866661     | -13.436025     |  |                         |       |
| 1.22.3 | 51.860705     | -13.437373     |  |                         |       |
| 1.22.4 | 51.863006     | -13.448348     |  |                         |       |
| 1.23.3 | 51.860808     | -13.437330     |  |                         |       |
| 1.23.4 | 51.862961     | -13.448395     |  |                         |       |
| 1.24.1 | 51.868021     | -13.437668     |  |                         |       |
| 1.24.2 | 51.866101     | -13.435692     |  |                         |       |
| 1.24.3 | 51.860662     | -13.437328     |  |                         |       |
| 1.24.4 | 51.862933     | -13.448304     |  |                         |       |
| 1.25.1 | 51.867883     | -13.437576     |  |                         |       |
| 1.25.2 | 51.865914     | -13.435689     |  |                         |       |
| 1.26.1 | 51.867935     | -13.437665     |  |                         |       |
| 1.26.2 | 51.865814     | -13.435631     |  |                         |       |
| 1.27.1 | 51.867799     | -13.437507     |  |                         |       |
| 1.27.2 | 51.865839     | -13.435704     |  |                         |       |

Table 7 continued

Table 7 (continued)

| ID     | R.A.<br>J2000 | Decl.<br>J2000 | $z$                                | $z_{spec}$<br>Reference | Notes |
|--------|---------------|----------------|------------------------------------|-------------------------|-------|
| 1.28.1 | 51.868061     | -13.437781     |                                    |                         |       |
| 1.28.2 | 51.865881     | -13.435573     |                                    |                         |       |
| 1.29.1 | 51.868073     | -13.437862     |                                    |                         |       |
| 1.29.2 | 51.865739     | -13.435504     |                                    |                         |       |
| 1.29.3 | 51.860607     | -13.437296     |                                    |                         |       |
| 1.29.4 | 51.862875     | -13.448266     |                                    |                         |       |
| 1.30.1 | 51.868080     | -13.438011     |                                    |                         |       |
| 1.30.2 | 51.865472     | -13.435394     |                                    |                         |       |
| 1.30.3 | 51.860578     | -13.437239     |                                    |                         |       |
| 1.30.4 | 51.862793     | -13.448231     |                                    |                         |       |
| 1.31.1 | 51.868121     | -13.438107     |                                    |                         |       |
| 1.31.2 | 51.865410     | -13.435331     |                                    |                         |       |
| 1.31.3 | 51.860495     | -13.437240     |                                    |                         |       |
| 1.31.4 | 51.862782     | -13.448193     |                                    |                         |       |
| 1.32.1 | 51.868116     | -13.438156     |                                    |                         |       |
| 1.32.2 | 51.865268     | -13.435287     |                                    |                         |       |
| 1.32.3 | 51.860459     | -13.437220     |                                    |                         |       |
| 1.32.4 | 51.862747     | -13.448176     |                                    |                         |       |
| 1.33.1 | 51.867846     | -13.437799     |                                    |                         |       |
| 1.33.2 | 51.865265     | -13.435503     |                                    |                         |       |
| 1.33.3 | 51.860750     | -13.437136     |                                    |                         |       |
| 1.33.4 | 51.862675     | -13.448327     |                                    |                         |       |
| 1.34.1 | 51.867540     | -13.437481     |                                    |                         |       |
| 1.34.2 | 51.865180     | -13.435649     |                                    |                         |       |
| 1.35.1 | 51.867953     | -13.438014     |                                    |                         |       |
| 1.35.2 | 51.865119     | -13.435373     |                                    |                         |       |
| 1.36.1 | 51.867646     | -13.437689     |                                    |                         |       |
| 1.36.2 | 51.864929     | -13.435546     |                                    |                         |       |
| 1.36.3 | 51.861259     | -13.436656     |                                    |                         |       |
| 1.37.1 | 51.867793     | -13.437957     | Bright red core of the west galaxy |                         |       |
| 1.37.2 | 51.864731     | -13.435403     |                                    |                         |       |
| 1.37.3 | 51.860701     | -13.437034     |                                    |                         |       |
| 1.37.4 | 51.862555     | -13.448303     |                                    |                         |       |
| 1.38.1 | 51.867951     | -13.438194     |                                    |                         |       |
| 1.38.2 | 51.864721     | -13.435261     |                                    |                         |       |
| 1.38.4 | 51.862551     | -13.448193     |                                    |                         |       |
| 1.39.1 | 51.867850     | -13.438161     |                                    |                         |       |
| 1.39.2 | 51.864457     | -13.435286     |                                    |                         |       |
| 1.39.4 | 51.862474     | -13.448229     |                                    |                         |       |
| 1.40.1 | 51.867639     | -13.437946     |                                    |                         |       |
| 1.40.2 | 51.864299     | -13.435427     |                                    |                         |       |

Table 7 continued

Table 7 (continued)

| ID     | R.A.<br>J2000 | Decl.<br>J2000 | $z$                     | $z_{spec}$<br>Reference | Notes                  |
|--------|---------------|----------------|-------------------------|-------------------------|------------------------|
| 1.40.4 | 51.862422     | -13.448343     |                         |                         |                        |
| 1.41.1 | 51.867575     | -13.437964     |                         |                         |                        |
| 1.41.2 | 51.864227     | -13.435429     |                         |                         |                        |
| 1.41.3 | 51.862751     | -13.435661     |                         |                         |                        |
| 1.41.4 | 51.862343     | -13.448359     |                         |                         |                        |
| 1.42.1 | 51.867703     | -13.438238     |                         |                         |                        |
| 1.42.2 | 51.863469     | -13.435318     |                         |                         |                        |
| 1.42.3 | 51.862794     | -13.435476     |                         |                         |                        |
| 1.42.4 | 51.862303     | -13.448218     |                         |                         |                        |
| 2.1.1  | 51.868737     | -13.437357     | 1.7010                  | ...                     | ("A") part of source 1 |
| 2.1.2  | 51.868428     | -13.436829     |                         |                         |                        |
| 3.1.1  | 51.866074     | -13.436360     | 1.7010                  | ...                     | part of source 1       |
| 3.1.2  | 51.864921     | -13.435939     |                         |                         |                        |
| 3.1.3  | 51.863321     | -13.435913     |                         |                         |                        |
| 4.1.1  | 51.871731     | -13.438264     | 2.7300                  | Lopez et al. (2018)     |                        |
| 4.1.2  | 51.870326     | -13.435747     |                         |                         |                        |
| 4.1.3  | 51.859482     | -13.438346     |                         |                         |                        |
| 4.1.4  | 51.864700     | -13.449324     |                         |                         |                        |
| 5.1.1  | 51.872897     | -13.434544     | 5.2000                  | Lopez et al. (2018)     |                        |
| 5.1.2  | 51.859969     | -13.439685     |                         |                         |                        |
| 5.1.3  | 51.871301     | -13.447044     |                         |                         |                        |
| 6.1.1  | 51.861985     | -13.441969     | 3.5180                  | This work; MUSE         |                        |
| 6.1.2  | 51.862410     | -13.441657     |                         |                         |                        |
| 7.1.1  | 51.866110     | -13.441461     | 2.8262                  | Lopez et al. (2018)     | (S7a) Radial arc       |
| 7.1.2  | 51.865888     | -13.441378     |                         |                         | (S7b)                  |
| 7.1.3  | 51.861632     | -13.431357     |                         |                         | (S7c)                  |
| 7.2.1  | 51.866409     | -13.441617     |                         |                         |                        |
| 7.2.2  | 51.865540     | -13.441324     |                         |                         |                        |
| 7.2.3  | 51.861772     | -13.431314     |                         |                         |                        |
| 7.3.1  | 51.866212     | -13.441498     |                         |                         |                        |
| 7.3.2  | 51.865803     | -13.441350     |                         |                         |                        |
| 7.4.1  | 51.866465     | -13.441638     |                         |                         |                        |
| 7.4.2  | 51.865482     | -13.441307     |                         |                         |                        |
| 8.1.1  | 51.861898     | -13.437829     | $3.073^{+1.87}_{-0.52}$ |                         | Radial arc             |
| 8.1.2  | 51.862620     | -13.438543     |                         |                         |                        |
| 9.1.1  | 51.864446     | -13.442833     | $2.772^{+0.35}_{-0.59}$ |                         | Radial arc             |
| 9.1.2  | 51.864118     | -13.442215     |                         |                         |                        |
| 9.2.1  | 51.864374     | -13.442661     | $2.116^{+2.65}_{-0.17}$ |                         |                        |
| 9.2.2  | 51.864187     | -13.442344     |                         |                         |                        |
| 10.1.1 | 51.860746     | -13.442996     | $2.501^{+0.07}_{-0.02}$ |                         | Radial arc             |

Table 7 continued



Table 7 (continued)

| ID     | R.A.<br>J2000 | Decl.<br>J2000 | $z$                       | $z_{spec}$<br>Reference | Notes      |
|--------|---------------|----------------|---------------------------|-------------------------|------------|
| 10.1.2 | 51.863311     | -13.441242     |                           |                         |            |
| 10.1.3 | 51.866801     | -13.430480     |                           |                         |            |
| 11.1.1 | 51.865991     | -13.442196     | $3.348^{+1.87}_{-0.61}$   |                         | Radial arc |
| 11.1.2 | 51.865548     | -13.441816     |                           |                         |            |
| 12.1.1 | 51.861857     | -13.439301     | $2.357^{+1.99}_{-0.11}$   |                         | Radial arc |
| 12.1.2 | 51.8621273    | -13.4393533    |                           |                         |            |
| 13.1.1 | 51.872008     | -13.442422     |                           |                         |            |
| 13.1.2 | 51.869600     | -13.433048     |                           |                         |            |
| 13.3   | 51.858583     | -13.439729     |                           |                         |            |
| 13.1.4 | 51.865692     | -13.448646     | $3.349^{+0.072}_{-0.079}$ |                         |            |
| 14.1.1 | 51.872048     | -13.438578     | $2.658^{+0.03}_{-0.03}$   |                         |            |
| 14.1.2 | 51.870323     | -13.435348     |                           |                         |            |
| 14.1.3 | 51.859465     | -13.438657     |                           |                         |            |
| 14.1.4 | 51.865012     | -13.449137     |                           |                         |            |
| 15.1.1 | 51.872119     | -13.438484     | $2.679^{+0.02}_{-0.05}$   |                         |            |
| 15.1.2 | 51.870544     | -13.435505     |                           |                         |            |
| 15.1.3 | 51.859580     | -13.438727     |                           |                         |            |
| 15.1.4 | 51.865240     | -13.449129     |                           |                         |            |
| 16.1.1 | 51.864756     | -13.446027     | $2.929^{+0.41}_{-0.10}$   |                         |            |
| 16.1.2 | 51.866044     | -13.445628     |                           |                         |            |
| 17.1.1 | 51.856582     | -13.435563     | $3.275^{+0.81}_{-0.56}$   |                         |            |
| 17.1.2 | 51.855895     | -13.436411     |                           |                         |            |
| 18.1.1 | 51.867692     | -13.447883     | $3.447^{+0.52}_{-0.29}$   |                         |            |
| 18.1.2 | 51.868275     | -13.447341     |                           |                         |            |
| 18.1.3 | 51.869144     | -13.446956     |                           |                         |            |
| 19.1.1 | 51.855839     | -13.443733     | $2.790^{+0.41}_{-0.12}$   |                         |            |
| 19.1.2 | 51.856174     | -13.444099     |                           |                         |            |
| 19.1.3 | 51.856763     | -13.445518     |                           |                         |            |
| 20.1.1 | 51.856767     | -13.439523     | $1.829^{+0.03}_{-0.03}$   |                         |            |
| 20.1.2 | 51.857704     | -13.444226     |                           |                         |            |
| 20.1.3 | 51.858988     | -13.445986     |                           |                         |            |
| 21.1.1 | 51.864125     | -13.434071     | $4.074^{+0.15}_{-0.19}$   |                         |            |
| 21.1.2 | 51.863315     | -13.434155     |                           |                         |            |
| 21.1.3 | 51.862592     | -13.434310     |                           |                         |            |
| 22.1.1 | 51.862524     | -13.434692     | $2.247^{+0.01}_{-0.05}$   |                         |            |
| 22.1.2 | 51.860819     | -13.435560     |                           |                         |            |
| 22.1.3 | 51.868483     | -13.438578     |                           |                         |            |
| 23.1.1 | 51.870614     | -13.437170     | $4.328^{+0.01}_{-0.23}$   |                         |            |
| 23.1.2 | 51.868167     | -13.434515     |                           |                         |            |
| 23.1.3 | 51.859952     | -13.435585     |                           |                         |            |

Table 7 continued

Table 7 (continued)

| ID                | R.A.<br>J2000 | Decl.<br>J2000 | $z$                     | $z_{spec}$<br>Reference                     | Notes |
|-------------------|---------------|----------------|-------------------------|---|-------|
| MACS J2129.4–0741 |               |                |                         |   |       |
| 1.1.1             | 322.357970    | -7.685880      | 1.36                    | Caminha et al. (2019); Jauzac et al. (2021) |       |
| 1.1.2             | 322.359661    | -7.690859      |                         |   |       |
| 1.1.3             | 322.359250    | -7.690950      |                         |   |       |
| 1.1.4             | 322.357120    | -7.691090      |                         |   |       |
| 1.1.5             | 322.357640    | -7.691150      |                         |   |       |
| 1.1.6             | 322.358610    | -7.694890      |                         |   |       |
| 2.1.1             | 322.354830    | -7.690700      | 1.048                   | Caminha et al. (2019); Jauzac et al. (2021) |       |
| 2.1.2             | 322.354770    | -7.691600      |                         |   |       |
| 2.1.3             | 322.355380    | -7.693320      |                         |   |       |
| 3.1.1             | 322.350220    | -7.688860      | 2.24                    | Caminha et al. (2019); Jauzac et al. (2021) |       |
| 3.1.2             | 322.350040    | -7.689820      |                         |   |       |
| 3.1.3             | 322.350950    | -7.695770      |                         |   |       |
| 4.1.1             | 322.366420    | -7.686740      | 2.24                    | Caminha et al. (2019); Jauzac et al. (2021) |       |
| 4.1.2             | 322.366930    | -7.688310      |                         |   |       |
| 4.1.3             | 322.366790    | -7.694970      |                         |   |       |
| 5.1.1             | 322.364220    | -7.693870      | $1.733^{+0.03}_{-0.04}$ |   |       |
| 5.1.2             | 322.364600    | -7.691370      |                         |   |       |
| 5.1.3             | 322.362430    | -7.684930      |                         |   |       |
| 6.1.1             | 322.350940    | -7.693330      | 6.85                    | Caminha et al. (2019); Jauzac et al. (2021) |       |
| 6.1.2             | 322.353240    | -7.697440      |                         |   |       |
| 6.1.3             | 322.353940    | -7.681640      |                         |   |       |
| 7.1.1             | 322.357140    | -7.694250      | 1.357                   | Caminha et al. (2019); Jauzac et al. (2021) |       |
| 7.1.2             | 322.356250    | -7.691720      |                         |   |       |
| 7.1.3             | 322.356700    | -7.685540      |                         |   |       |
| 8.1.1             | 322.356980    | -7.689240      | 4.410                   | Caminha et al. (2019); Jauzac et al. (2021) |       |
| 8.1.2             | 322.361670    | -7.688080      |                         |   |       |
| 8.1.3             | 322.358600    | -7.684910      |                         |   |       |
| 8.1.4             | 322.360350    | -7.700940      |                         |   |       |
| 8.1.5             | 322.354186    | -7.688763      |                         |   |       |
| 9.1.1             | 322.366510    | -7.686890      | 2.24                    | Caminha et al. (2019); Jauzac et al. (2021) |       |
| 9.1.2             | 322.366950    | -7.688200      |                         |   |       |
| 9.1.3             | 322.366660    | -7.695250      |                         |   |       |
| 10.1.1            | 322.357618    | -7.684709      | 4.41                    | Caminha et al. (2019); Jauzac et al. (2021) |       |
| 10.1.3            | 322.354988    | -7.688960      |                         |   |       |
| 11.1.1            | 322.363338    | -7.697070      | 3.1081                  | Caminha et al. (2019); Jauzac et al. (2021) |       |
| 11.1.2            | 322.364905    | -7.690096      |                         |   |       |
| 11.1.3            | 322.361673    | -7.683623      |                         |   |       |
| 12.1.1            | 322.354550    | -7.685180      | 3.897                   | Caminha et al. (2019); Jauzac et al. (2021) |       |

Table 7 continued

Table 7 (continued)

| ID                 | R.A.<br>J2000 | Decl.<br>J2000 | $z$                     | $z_{spec}$<br>Reference                     | Notes               |
|--------------------|---------------|----------------|-------------------------|---|---------------------|
| 12.1.2             | 322.352780    | -7.688412      |                         |   |                     |
| 13.1.1             | 322.353304    | -7.691134      | 1.3585                  | Caminha et al. (2019); Jauzac et al. (2021) |                     |
| 13.1.2             | 322.353912    | -7.687584      |                         |   |                     |
| 13.1.3             | 322.354428    | -7.694413      |                         |   |                     |
| 14.1.1             | 322.361311    | -7.685896      | 1.451                   | Caminha et al. (2019); Jauzac et al. (2021) |                     |
| 14.1.3             | 322.362594    | -7.693603      |                         |   |                     |
| 16.1.1             | 322.361637    | -7.690945      | $1.082^{+0.00}_{-0.02}$ |   |                     |
| 16.1.2             | 322.361559    | -7.692262      |                         |   |                     |
| 16.1.3             | 322.361128    | -7.688382      |                         |   |                     |
| 17.1.1             | 322.355734    | -7.694368      | $1.948^{+0.04}_{-0.04}$ |   |                     |
| 17.1.2             | 322.355149    | -7.693848      | $5.528^{+0.47}_{-0.19}$ |   |                     |
| 17.1.3             | 322.355853    | -7.683335      |                         |   |                     |
| 18.1.1             | 322.3513795   | -7.6837914     | $5.528^{+0.47}_{-0.19}$ |   |                     |
| 18.1.2             | 322.3495315   | -7.6864161     |                         |   |                     |
| 18.1.3             | 322.3507339   | -7.6986070     |                         |   |                     |
| PSZ1 G091.83+26.11 |               |                |                         |   |                     |
| 1.1.1              | 277.7869620   | 62.2510888     | [4.4]                   |   | fixed at Photo- $z$ |
| 1.1.2              | 277.7752863   | 62.2501733     |                         |   |                     |
| 1.1.3              | 277.7874961   | 62.2483920     |                         |   |                     |
| 1.1.4              | 277.7994872   | 62.2482763     |                         |   |                     |
| 1.2.1              | 277.7869786   | 62.2511314     |                         |   |                     |
| 1.2.2              | 277.7752793   | 62.2502210     |                         |   |                     |
| 1.2.3              | 277.7875272   | 62.2485160     |                         |   |                     |
| 1.2.4              | 277.7994884   | 62.2483722     |                         |   |                     |
| 1.3.2              | 277.7753932   | 62.2501785     |                         |   |                     |
| 1.3.3              | 277.7874750   | 62.2484214     |                         |   |                     |
| 1.3.4              | 277.7995271   | 62.2482937     |                         |   |                     |
| 1.4.3              | 277.7874305   | 62.2482261     |                         |   |                     |
| 1.4.4              | 277.7994924   | 62.2481162     |                         |   |                     |
| 1.5.1              | 277.7866780   | 62.2511427     |                         |   |                     |
| 1.5.2              | 277.7757413   | 62.2502249     |                         |   |                     |
| 1.5.3              | 277.7874197   | 62.2486210     |                         |   |                     |
| 1.5.4              | 277.7997173   | 62.2483896     |                         |   |                     |
| 1.6.1              | 277.7868386   | 62.2513011     |                         |   |                     |
| 1.6.2              | 277.7755426   | 62.2503851     |                         |   |                     |
| 1.6.4              | 277.7996035   | 62.2487011     |                         |   |                     |
| 1.7.1              | 277.7864894   | 62.2514413     |                         |   |                     |
| 1.7.2              | 277.7759003   | 62.2505153     |                         |   |                     |

Table 7 continued

Table 7 (continued)

| ID     | R.A.<br>J2000 | Decl.<br>J2000 | $z$   | $z_{spec}$<br>Reference | Notes               |
|--------|---------------|----------------|-------|-------------------------|---------------------|
| 1.7.4  | 277.7998018   | 62.2489277     |       |                         |                     |
| 1.8.1  | 277.7865464   | 62.2514870     |       |                         |                     |
| 1.8.2  | 277.7758083   | 62.2505735     |       |                         |                     |
| 1.8.4  | 277.7997376   | 62.2490416     |       |                         |                     |
| 1.9.1  | 277.7865464   | 62.2515431     |       |                         |                     |
| 1.9.2  | 277.7757215   | 62.2506414     |       |                         |                     |
| 1.9.4  | 277.7997091   | 62.2491390     |       |                         |                     |
| 1.10.3 | 277.7874720   | 62.2478191     |       |                         |                     |
| 1.10.4 | 277.7992313   | 62.2476938     |       |                         |                     |
| 1.11.1 | 277.7873344   | 62.2506898     |       |                         |                     |
| 1.11.2 | 277.7746473   | 62.2496752     |       |                         |                     |
| 1.11.3 | 277.7876023   | 62.2475400     |       |                         |                     |
| 1.11.4 | 277.7989422   | 62.2471154     |       |                         |                     |
| 1.12.1 | 277.7873426   | 62.2506048     |       |                         |                     |
| 1.12.2 | 277.7746267   | 62.2495807     |       |                         |                     |
| 1.12.3 | 277.7875963   | 62.2474256     |       |                         |                     |
| 1.12.4 | 277.7988844   | 62.2468949     |       |                         |                     |
| 1.13.2 | 277.7748009   | 62.2493628     |       |                         |                     |
| 1.13.3 | 277.7873677   | 62.2470452     |       |                         |                     |
| 1.13.4 | 277.7988420   | 62.2464807     |       |                         |                     |
| 1.14.2 | 277.7748632   | 62.2493136     |       |                         |                     |
| 1.14.3 | 277.7872827   | 62.2470057     |       |                         |                     |
| 1.14.4 | 277.7988295   | 62.2463978     |       |                         |                     |
| 1.15.1 | 277.7871609   | 62.2502841     |       |                         |                     |
| 1.15.2 | 277.7752217   | 62.2491330     |       |                         |                     |
| 1.15.3 | 277.7870082   | 62.2469761     |       |                         |                     |
| 1.15.4 | 277.7989111   | 62.2462362     |       |                         |                     |
| 1.16.1 | 277.7874079   | 62.2500616     |       |                         |                     |
| 1.16.2 | 277.7750115   | 62.2488523     |       |                         |                     |
| 1.16.3 | 277.7869465   | 62.2467345     |       |                         |                     |
| 1.16.4 | 277.7985826   | 62.2455983     |       |                         |                     |
| 1.17.1 | 277.7870989   | 62.2496455     |       |                         |                     |
| 1.17.2 | 277.7762758   | 62.2485726     |       |                         |                     |
| 1.17.3 | 277.7860480   | 62.2468622     |       |                         |                     |
| 1.17.4 | 277.7990335   | 62.2453401     |       |                         |                     |
| 1.18.2 | 277.7763622   | 62.2481439     |       |                         |                     |
| 1.18.3 | 277.7856997   | 62.2466629     |       |                         |                     |
| 1.18.4 | 277.7987771   | 62.2446211     |       |                         |                     |
| 2.1.1  | 277.7854050   | 62.2493730     | [2.8] |                         | fixed at Photo- $z$ |
| 2.1.2  | 277.7843175   | 62.2491381     |       |                         |                     |
| 2.1.3  | 277.7847487   | 62.2489539     |       |                         |                     |

Table 7 continued



Table 7 (continued)

| ID      | R.A.<br>J2000 | Decl.<br>J2000 | $z$                     | $z_{spec}$<br>Reference | Notes |
|---------|---------------|----------------|-------------------------|-------------------------|-------|
| 2.1.4   | 277.7959287   | 62.2481713     |                         |                         |       |
| 2.1.5   | 277.7854979   | 62.2493044     |                         |                         |       |
| 2.2.2   | 277.7842379   | 62.2491010     |                         |                         |       |
| 2.2.3   | 277.7847361   | 62.2489129     |                         |                         |       |
| 2.3.1   | 277.7854799   | 62.2494749     |                         |                         |       |
| 2.3.2   | 277.7839669   | 62.2492076     |                         |                         |       |
| 2.3.3   | 277.7851582   | 62.2488151     |                         |                         |       |
| 2.3.4   | 277.7957981   | 62.2482003     |                         |                         |       |
| 3.1.1   | 277.7857140   | 62.2505085     | $4.581^{+0.09}_{-0.03}$ |                         |       |
| c3.1.2a | 277.7776959   | 62.2493322     |                         |                         |       |
| c3.1.2b | 277.7770779   | 62.2494257     |                         |                         |       |
| c3.1.2c | 277.7778193   | 62.2498238     |                         |                         |       |
| 3.1.3   | 277.7859491   | 62.2478811     |                         |                         |       |
| 3.1.4   | 277.8004209   | 62.2473581     |                         |                         |       |
| 4.1.1   | 277.7936034   | 62.2525418     | $3.642^{+0.04}_{-0.06}$ |                         |       |
| 4.1.2   | 277.7874089   | 62.2526513     |                         |                         |       |
| 4.1.3   | 277.7789478   | 62.2524631     |                         |                         |       |
| 4.2.1   | 277.7937844   | 62.2525446     | $3.617^{+0.08}_{-0.05}$ |                         |       |
| 4.2.2   | 277.7872413   | 62.2526708     |                         |                         |       |
| 4.2.3   | 277.7791224   | 62.2524891     |                         |                         |       |
| 4.3.1   | 277.7940137   | 62.2524772     | $3.635^{+0.03}_{-0.08}$ |                         |       |
| 4.3.2   | 277.7869577   | 62.2526539     |                         |                         |       |
| 4.3.3   | 277.7793528   | 62.2524485     |                         |                         |       |
| 5.1.1   | 277.7943034   | 62.2533904     | $4.588^{+0.00}_{-0.12}$ |                         |       |
| 5.1.2   | 277.7882075   | 62.2538140     |                         |                         |       |
| 5.1.3   | 277.7750379   | 62.2527944     |                         |                         |       |
| 5.2.1   | 277.7940439   | 62.2533904     | $4.604^{+0.01}_{-0.13}$ |                         |       |
| 5.2.2   | 277.7883483   | 62.2537906     |                         |                         |       |
| 5.2.3   | 277.7747966   | 62.2527522     |                         |                         |       |
| c6.1.1  | 277.7864548   | 62.2563030     | ...                     |                         |       |
| c6.1.2  | 277.7819559   | 62.2558484     |                         |                         |       |
| c6.1.3  | 277.7879239   | 62.2563098     |                         |                         |       |
| c7.1.1  | 277.7900394   | 62.2572796     | ...                     |                         |       |
| c7.1.2  | 277.7886401   | 62.2574043     |                         |                         |       |
| c7.1.3  | 277.7906497   | 62.2573414     |                         |                         |       |
| c8.1.1  | 277.8235233   | 62.2483831     | ...                     |                         |       |
| c8.1.2  | 277.8220189   | 62.2489751     |                         |                         |       |
| c8.1.3  | 277.8210136   | 62.2492630     |                         |                         |       |
| c8.1.4  | 277.8203899   | 62.2481170     |                         |                         |       |
| c9.1.1  | 277.8244726   | 62.2490875     | ...                     |                         |       |

Table 7 continued

Table 7 (continued)

| ID              | R.A.<br>J2000 | Decl.<br>J2000 | $z$                     | $z_{spec}$<br>Reference | Notes |
|-----------------|---------------|----------------|-------------------------|-------------------------|-------|
| c9.1.2          | 277.8233781   | 62.2495567     |                         |                         |       |
| c9.1.3          | 277.8225815   | 62.2498573     |                         |                         |       |
| c9.1.4          | 277.8204873   | 62.2480822     |                         |                         |       |
| c10.1.1         | 277.8182071   | 62.2448778     | ...                     |                         |       |
| c10.1.2         | 277.8157900   | 62.2459444     |                         |                         |       |
| c11.1.1         | 277.8100988   | 62.2374333     | ...                     |                         |       |
| c11.1.2         | 277.8107708   | 62.2370336     |                         |                         |       |
| c12.1.1         | 277.8029047   | 62.2671327     | ...                     |                         |       |
| c12.1.2         | 277.8025794   | 62.2672977     |                         |                         |       |
| RX J0152.7-1357 |               |                |                         |                         |       |
| 1.1.1           | 28.189076     | -13.952246     | 3.93                    | Acebron et al. (2019)   |       |
| 1.1.2           | 28.188361     | -13.951203     |                         |                         |       |
| 1.1.3           | 28.185287     | -13.948941     |                         |                         |       |
| 1.1.4           | 28.187669     | -13.951236     |                         |                         |       |
| 2.1.1           | 28.187278     | -13.954577     | $2.912^{+0.58}_{-0.34}$ |                         |       |
| 2.1.2           | 28.185848     | -13.952977     |                         |                         |       |
| 2.1.3           | 28.183338     | -13.950919     |                         |                         |       |
| 3.1.1           | 28.184894     | -13.956606     | $1.655^{+0.11}_{-0.13}$ |                         |       |
| 3.1.2           | 28.183271     | -13.954315     |                         |                         |       |
| 3.1.3           | 28.181590     | -13.953478     |                         |                         |       |
| 3.2.1           | 28.184576     | -13.956697     |                         |                         |       |
| 3.2.2           | 28.183286     | -13.954600     |                         |                         |       |
| 3.2.3           | 28.181065     | -13.953554     |                         |                         |       |
| 4.1.1           | 28.183443     | -13.956815     | $1.689^{+0.09}_{-0.15}$ |                         |       |
| 4.1.2           | 28.182984     | -13.956555     |                         |                         |       |
| 5.1.1           | 28.182444     | -13.959993     | $2.623^{+0.24}_{-0.66}$ |                         |       |
| 5.1.2           | 28.179475     | -13.958578     |                         |                         |       |
| 5.1.3           | 28.177450     | -13.956018     |                         |                         |       |
| 5.2.1           | 28.182206     | -13.959883     |                         |                         |       |
| 5.2.2           | 28.179661     | -13.958668     |                         |                         |       |
| 5.2.3           | 28.177385     | -13.955889     |                         |                         |       |
| 6.1.1           | 28.181477     | -13.953185     | $4.390^{+0.43}_{-0.46}$ |                         |       |
| 6.1.2           | 28.183328     | -13.954069     |                         |                         |       |
| 6.1.3           | 28.185407     | -13.956885     |                         |                         |       |
| 7.1.1           | 28.164320     | -13.968186     | $4.350^{+0.44}_{-0.47}$ |                         |       |
| 7.1.2           | 28.164454     | -13.968568     |                         |                         |       |
| 8.1.1           | 28.1814770    | -13.9531845    | $1.926^{+0.14}_{-0.18}$ |                         |       |
| 8.1.2           | 28.1833283    | -13.9540692    |                         |                         |       |

Table 7 continued

Table 7 (continued)

| ID                | R.A.<br>J2000 | Decl.<br>J2000 | $z$                     | $z_{spec}$<br>Reference | Notes            |
|-------------------|---------------|----------------|-------------------------|-------------------------|------------------|
| 8.1.3             | 28.1854073    | -13.9568849    |                         |                         |                  |
| 11.1.2            | 28.1643199    | -13.9681861    | $4.450^{+0.20}_{-2.58}$ |                         |                  |
| 11.1.3            | 28.1644544    | -13.9685681    |                         |                         |                  |
| SPT-CL J0516–5755 |               |                |                         |                         |                  |
| 1.1.1             | 79.239337     | -57.919780     | [2,5]                   |                         | fixed at Photo-z |
| 1.1.2             | 79.247988     | -57.918978     |                         |                         |                  |
| 1.1.3             | 79.250781     | -57.917842     |                         |                         |                  |
| 1.2.1             | 79.239299     | -57.919948     |                         |                         |                  |
| 1.2.2             | 79.248751     | -57.918934     |                         |                         |                  |
| 1.2.3             | 79.250289     | -57.918338     |                         |                         |                  |
| 1.3.1             | 79.239342     | -57.919604     |                         |                         |                  |
| 1.3.2             | 79.247563     | -57.918914     |                         |                         |                  |
| 1.3.3             | 79.251129     | -57.917350     |                         |                         |                  |
| 1.3.4             | 79.246525     | -57.917927     |                         |                         |                  |
| 2.1.1             | 79.248980     | -57.916689     | $2.064^{+0.00}_{-0.05}$ |                         |                  |
| 2.1.2             | 79.245068     | -57.917352     |                         |                         |                  |
| 2.1.3             | 79.241400     | -57.918282     |                         |                         |                  |
| 2.2.1             | 79.249042     | -57.916612     | $2.034^{+0.03}_{-0.01}$ |                         |                  |
| 2.2.2             | 79.244889     | -57.917333     |                         |                         |                  |
| 2.2.3             | 79.241380     | -57.918202     |                         |                         |                  |
| 2.3.1             | 79.248876     | -57.916787     | $2.029^{+0.03}_{-0.01}$ |                         |                  |
| 2.3.2             | 79.245349     | -57.917370     |                         |                         |                  |
| 2.3.3             | 79.241403     | -57.918386     |                         |                         |                  |
| 2.4.1             | 79.248892     | -57.916762     | $2.033^{+0.03}_{-0.02}$ |                         |                  |
| 2.4.2             | 79.245289     | -57.917363     |                         |                         |                  |
| 2.4.3             | 79.241397     | -57.918359     |                         |                         |                  |
| 3.1.1             | 79.239419     | -57.921004     | $2.955^{+0.06}_{-0.01}$ |                         |                  |
| 3.1.2             | 79.249568     | -57.920537     |                         |                         |                  |
| 3.1.3             | 79.253018     | -57.919178     |                         |                         |                  |
| 3.2.2             | 79.249666     | -57.920404     | $2.958^{+0.06}_{-0.06}$ |                         |                  |
| 3.2.3             | 79.252866     | -57.919118     |                         |                         |                  |
| 3.3.2             | 79.249485     | -57.920617     | $2.905^{+0.21}_{-0.01}$ |                         |                  |
| 3.3.3             | 79.253124     | -57.919186     |                         |                         |                  |
| 4.1.1             | 79.250914     | -57.914233     | $4.970^{+0.03}_{-0.40}$ |                         |                  |
| 4.1.2             | 79.246614     | -57.914073     |                         |                         |                  |
| 4.1.3             | 79.230979     | -57.917197     |                         |                         |                  |
| 4.2.1             | 79.251128     | -57.914267     | $4.743^{+0.15}_{-0.29}$ |                         |                  |
| 4.2.2             | 79.246450     | -57.914113     |                         |                         |                  |

Table 7 continued

Table 7 (continued)

| ID                | R.A.<br>J2000 | Decl.<br>J2000 | $z$                     | $z_{\text{spec}}$<br>Reference | Notes |
|-------------------|---------------|----------------|-------------------------|--------------------------------|-------|
| 5.1.1             | 79.247830     | -57.914088     | $2.523^{+0.01}_{-0.05}$ |                                |       |
| 5.1.2             | 79.245443     | -57.914160     |                         |                                |       |
| 5.1.3             | 79.236501     | -57.915932     |                         |                                |       |
| 6.1.2             | 79.249938     | -57.919894     | $2.703^{+0.22}_{-0.01}$ |                                |       |
| 6.1.3             | 79.251974     | -57.919098     |                         |                                |       |
| 7.1.1             | 79.243724     | -57.922309     | $3.181^{+0.08}_{-0.06}$ |                                |       |
| 7.1.2             | 79.248277     | -57.922418     |                         |                                |       |
| 7.1.3             | 79.254805     | -57.920349     |                         |                                |       |
| 7.2.1             | 79.242988     | -57.922267     | $3.189^{+0.06}_{-0.08}$ |                                |       |
| 7.2.2             | 79.248711     | -57.922363     |                         |                                |       |
| 7.2.3             | 79.254528     | -57.920457     |                         |                                |       |
| 7.3.1             | 79.242716     | -57.922319     | $3.149^{+0.08}_{-0.06}$ |                                |       |
| 7.3.2             | 79.249178     | -57.922340     |                         |                                |       |
| 7.3.3             | 79.254200     | -57.920678     |                         |                                |       |
| 8.1.1             | 79.248756     | -57.913471     | $2.714^{+0.00}_{-0.08}$ |                                |       |
| 8.1.2             | 79.244291     | -57.913620     |                         |                                |       |
| 8.1.3             | 79.235946     | -57.915279     |                         |                                |       |
| c9.1.2            | 79.239817     | -57.915020     | ...                     |                                |       |
| c9.1.3            | 79.239712     | -57.915060     |                         |                                |       |
| c9.1.1            | 79.250913     | -57.913842     |                         |                                |       |
| c9.2.2            | 79.240678     | -57.914713     |                         |                                |       |
| c9.2.3            | 79.239344     | -57.915166     |                         |                                |       |
| 10.1.2            | 79.243620     | -57.917139     | $2.115^{+0.02}_{-0.06}$ |                                |       |
| 10.1.3            | 79.241795     | -57.917649     |                         |                                |       |
| SPT-CL J2011–5228 |               |                |                         |                                |       |
| 1.1.1             | 302.778750    | -52.468514     | 2.39                    | Collett et al. (2017)          |       |
| 1.1.2             | 302.777304    | -52.473801     |                         |                                |       |
| 1.1.3             | 302.786413    | -52.473878     |                         |                                |       |
| 1.1.4             | 302.788056    | -52.468085     |                         |                                |       |
| 1.1.5             | 302.783401    | -52.470918     |                         |                                |       |
| 1.2.1             | 302.778605    | -52.468359     |                         |                                |       |
| 1.2.2             | 302.776123    | -52.472561     |                         |                                |       |
| 1.2.3             | 302.786457    | -52.473619     |                         |                                |       |
| 1.2.4             | 302.785920    | -52.467308     |                         |                                |       |
| 1.2.5             | 302.784020    | -52.471090     |                         |                                |       |
| 1.3.1             | 302.776720    | -52.469639     |                         |                                |       |
| 1.3.2             | 302.776185    | -52.471744     |                         |                                |       |
| 1.3.3             | 302.785524    | -52.473703     |                         |                                |       |

Table 7 continued



Table 7 (continued)

| ID     | R.A.<br>J2000 | Decl.<br>J2000 | $z$ | $z_{spec}$<br>Reference | Notes |
|--------|---------------|----------------|-----|-------------------------|-------|
| 1.3.4  | 302.786017    | -52.467120     |     |                         |       |
| 1.3.5  | 302.783865    | -52.471347     |     |                         |       |
| 1.4.2  | 302.776110    | -52.472685     |     |                         |       |
| 1.4.3  | 302.786757    | -52.473530     |     |                         |       |
| 1.4.4  | 302.785390    | -52.467269     |     |                         |       |
| 1.4.5  | 302.784113    | -52.471039     |     |                         |       |
| 1.4.6  | 302.776430    | -52.472941     |     |                         |       |
| 1.4.7  | 302.776819    | -52.473485     |     |                         |       |
| 1.5.1  | 302.776974    | -52.469463     |     |                         |       |
| 1.5.2  | 302.776145    | -52.472136     |     |                         |       |
| 1.5.3  | 302.785922    | -52.473689     |     |                         |       |
| 1.5.5  | 302.783920    | -52.471241     |     |                         |       |
| 1.6.2  | 302.776341    | -52.472333     |     |                         |       |
| 1.6.3  | 302.785582    | -52.473885     |     |                         |       |
| 1.6.4  | 302.787028    | -52.467465     |     |                         |       |
| 1.6.5  | 302.783560    | -52.471175     |     |                         |       |
| 1.7.2  | 302.776045    | -52.472627     |     |                         |       |
| 1.7.3  | 302.786759    | -52.473505     |     |                         |       |
| 1.7.4  | 302.784679    | -52.467175     |     |                         |       |
| 1.7.5  | 302.784164    | -52.471059     |     |                         |       |
| 1.7.6  | 302.776532    | -52.473056     |     |                         |       |
| 1.7.7  | 302.776725    | -52.473362     |     |                         |       |
| 1.9.1  | 302.776805    | -52.469752     |     |                         |       |
| 1.9.2  | 302.776376    | -52.471894     |     |                         |       |
| 1.9.3  | 302.785055    | -52.473923     |     |                         |       |
| 1.9.4  | 302.787054    | -52.467369     |     |                         |       |
| 1.9.5  | 302.783347    | -52.471265     |     |                         |       |
| 1.10.1 | 302.777721    | -52.469223     |     |                         |       |
| 1.10.2 | 302.777413    | -52.473786     |     |                         |       |
| 1.10.3 | 302.786022    | -52.474016     |     |                         |       |
| 1.10.4 | 302.788336    | -52.468186     |     |                         |       |
| 1.10.5 | 302.783094    | -52.470933     |     |                         |       |
| 1.12.2 | 302.776112    | -52.472286     |     |                         |       |
| 1.12.3 | 302.786123    | -52.473657     |     |                         |       |
| 1.12.5 | 302.783945    | -52.471186     |     |                         |       |
| 1.13.2 | 302.776257    | -52.471842     |     |                         |       |
| 1.13.3 | 302.785323    | -52.473810     |     |                         |       |
| 1.13.4 | 302.786546    | -52.467242     |     |                         |       |
| 1.13.5 | 302.783662    | -52.471306     |     |                         |       |
| 1.14.2 | 302.775857    | -52.471818     |     |                         |       |
| 1.14.3 | 302.786208    | -52.473365     |     |                         |       |

Table 7 continued

Table 7 (continued)

| ID     | R.A.<br>J2000 | Decl.<br>J2000 | $z$  | $z_{spec}$<br>Reference | Notes |
|--------|---------------|----------------|------|-------------------------|-------|
| 1.14.5 | 302.784478    | -52.471378     |      |                         |       |
| 1.15.1 | 302.778616    | -52.468309     |      |                         |       |
| 1.15.2 | 302.776045    | -52.472465     |      |                         |       |
| 1.15.3 | 302.786459    | -52.473569     |      |                         |       |
| 1.15.4 | 302.785220    | -52.467181     |      |                         |       |
| 1.15.5 | 302.784111    | -52.471128     |      |                         |       |
| 1.16.2 | 302.775965    | -52.472341     |      |                         |       |
| 1.16.3 | 302.786454    | -52.473511     |      |                         |       |
| 1.16.5 | 302.784240    | -52.471178     |      |                         |       |
| 1.17.2 | 302.775978    | -52.472261     |      |                         |       |
| 1.17.3 | 302.786349    | -52.473529     |      |                         |       |
| 1.18.6 | 302.776841    | -52.472824     |      |                         |       |
| 1.18.7 | 302.776973    | -52.472923     |      |                         |       |
| 1.19.6 | 302.776741    | -52.472864     |      |                         |       |
| 1.19.7 | 302.776867    | -52.472969     |      |                         |       |
| 1.20.6 | 302.776563    | -52.472916     |      |                         |       |
| 1.20.7 | 302.776817    | -52.473189     |      |                         |       |
| 1.21.1 | 302.778809    | -52.468405     |      |                         |       |
| 1.21.2 | 302.777113    | -52.473539     |      |                         |       |
| 1.21.3 | 302.786508    | -52.473760     |      |                         |       |
| 1.21.5 | 302.783702    | -52.470964     |      |                         |       |
| 1.22.1 | 302.777476    | -52.469217     |      |                         |       |
| 1.22.2 | 302.777029    | -52.473390     |      |                         |       |
| 1.22.3 | 302.786208    | -52.473807     |      |                         |       |
| 1.22.5 | 302.783634    | -52.471033     |      |                         |       |
| 1.23.2 | 302.776326    | -52.472367     |      |                         |       |
| 1.23.3 | 302.785456    | -52.473916     |      |                         |       |
| 1.23.5 | 302.783502    | -52.471160     |      |                         |       |
| 1.24.2 | 302.777457    | -52.473627     |      |                         |       |
| 1.24.3 | 302.785626    | -52.474100     |      |                         |       |
| 1.24.5 | 302.782845    | -52.470949     |      |                         |       |
| 1.25.2 | 302.777236    | -52.473334     |      |                         |       |
| 1.25.3 | 302.785376    | -52.474010     |      |                         |       |
| 1.25.5 | 302.783207    | -52.471100     |      |                         |       |
| 1.26.2 | 302.777336    | -52.473516     |      |                         |       |
| 1.26.3 | 302.785389    | -52.474069     |      |                         |       |
| 1.26.5 | 302.783106    | -52.471040     |      |                         |       |
| 2.1.2  | 302.776724    | -52.471719     | 2.39 | Collett et al. (2017)   |       |
| 2.1.3  | 302.784262    | -52.474137     |      |                         |       |
| 2.1.4  | 302.787970    | -52.467604     |      |                         |       |
| 2.1.5  | 302.782647    | -52.471186     |      |                         |       |

Table 7 continued

Table 7 (continued)

| ID    | R.A.<br>J2000 | Decl.<br>J2000 | $z$                   | $z_{spec}$<br>Reference | Notes |
|-------|---------------|----------------|-----------------------|-------------------------|-------|
| 2.1.7 | 302.777305    | -52.472830     |                       |                         |       |
| 2.1.8 | 302.777261    | -52.472535     |                       |                         |       |
| 3.1   | 302.773559    | -52.472525     | $2.557^{+0.4}_{-0.3}$ |                         |       |
| 3.2   | 302.788050    | -52.471836     |                       |                         |       |
| 3.3   | 302.786087    | -52.471206     |                       |                         |       |

NOTE—Properties of the multiple images identified in each cluster. The image ID for each multiple image is labeled such that the first number corresponds to the image system, the second number corresponds to the image, and the third number corresponds to a specific substructure clump in the image. The RA and Dec are provided for each image in degrees, where the coordinate frame is aligned to the JWST WCS. The redshift and associated reference for the multiple images in each cluster is also listed, where the redshift either corresponds to a spectroscopic measurement, in which case it does not include error bars, a model redshift estimate, in which case error bars are provided, or a fixed model redshift, which is denoted by brackets. Candidate lensing systems are denoted with the letter c, such that c1.1.1 indicates candidate System #1, Image #1, Clump #1.

## REFERENCES

- Abbott, T. M. C., Abdalla, F. B., Alarcon, A., et al. 2018, *PhRvD*, 98, 043526, doi: [10.1103/PhysRevD.98.043526](https://doi.org/10.1103/PhysRevD.98.043526)
- Acebron, A., Alon, M., Zitrin, A., et al. 2019, *ApJ*, 874, 132, doi: [10.3847/1538-4357/ab0adf](https://doi.org/10.3847/1538-4357/ab0adf)
- Adamo, A., Bradley, L. D., Vanzella, E., et al. 2024, *Nature*, 632, 513, doi: [10.1038/s41586-024-07703-7](https://doi.org/10.1038/s41586-024-07703-7)
- Anderson, M. E., Gaspari, M., White, S. D. M., Wang, W., & Dai, X. 2015, *MNRAS*, 449, 3806, doi: [10.1093/mnras/stv437](https://doi.org/10.1093/mnras/stv437)
- Artis, E., Adam, R., Ade, P., et al. 2022, arXiv e-prints, arXiv:2204.14052, doi: [10.48550/arXiv.2204.14052](https://doi.org/10.48550/arXiv.2204.14052)
- Astropy Collaboration, Robitaille, T. P., Tollerud, E. J., et al. 2013, *A&A*, 558, A33, doi: [10.1051/0004-6361/201322068](https://doi.org/10.1051/0004-6361/201322068)
- Atek, H., Shuntov, M., Furtak, L. J., et al. 2023, *MNRAS*, 519, 1201, doi: [10.1093/mnras/stac3144](https://doi.org/10.1093/mnras/stac3144)
- Bacon, R., Accardo, M., Adjali, L., et al. 2010, in *Society of Photo-Optical Instrumentation Engineers (SPIE) Conference Series*, Vol. 7735, *Ground-based and Airborne Instrumentation for Astronomy III*, ed. I. S. McLean, S. K. Ramsay, & H. Takami, 773508, doi: [10.1117/12.856027](https://doi.org/10.1117/12.856027)
- Bartelmann, M. 2010a, *Classical and Quantum Gravity*, 27, 233001, doi: [10.1088/0264-9381/27/23/233001](https://doi.org/10.1088/0264-9381/27/23/233001)
- . 2010b, *Classical and Quantum Gravity*, 27, 233001, doi: [10.1088/0264-9381/27/23/233001](https://doi.org/10.1088/0264-9381/27/23/233001)
- Bertin, E., & Arnouts, S. 1996a, *A&AS*, 117, 393, doi: [10.1051/aas:1996164](https://doi.org/10.1051/aas:1996164)
- . 1996b, *A&AS*, 117, 393, doi: [10.1051/aas:1996164](https://doi.org/10.1051/aas:1996164)
- Birrer, S., Millon, M., Sluse, D., et al. 2024, *SSRv*, 220, 48, doi: [10.1007/s11214-024-01079-w](https://doi.org/10.1007/s11214-024-01079-w)
- Bocquet, S., Dietrich, J. P., Schrabback, T., et al. 2019, *ApJ*, 878, 55, doi: [10.3847/1538-4357/ab1f10](https://doi.org/10.3847/1538-4357/ab1f10)
- Bordoloi, R., Rigby, J. R., Tumlinson, J., et al. 2016, *MNRAS*, 458, 1891, doi: [10.1093/mnras/stw449](https://doi.org/10.1093/mnras/stw449)
- Bradač, M., Strait, V., Mowla, L., et al. 2024, *ApJL*, 961, L21, doi: [10.3847/2041-8213/ad0e73](https://doi.org/10.3847/2041-8213/ad0e73)
- Calzetti, D., Armus, L., Bohlin, R. C., et al. 2000, *ApJ*, 533, 682, doi: [10.1086/308692](https://doi.org/10.1086/308692)
- Caminha, G. B., Rosati, P., Grillo, C., et al. 2019, *A&A*, 632, A36, doi: [10.1051/0004-6361/201935454](https://doi.org/10.1051/0004-6361/201935454)
- Caputi, K. I., Caminha, G. B., Fujimoto, S., et al. 2021, *ApJ*, 908, 146, doi: [10.3847/1538-4357/abd4d0](https://doi.org/10.3847/1538-4357/abd4d0)
- Cerny, C., Sharon, K., Andrade-Santos, F., et al. 2018, *ApJ*, 859, 159, doi: [10.3847/1538-4357/aabe7b](https://doi.org/10.3847/1538-4357/aabe7b)
- Claeysens, A., Adamo, A., Messa, M., et al. 2024, arXiv e-prints, arXiv:2410.10974, doi: [10.48550/arXiv.2410.10974](https://doi.org/10.48550/arXiv.2410.10974)
- . 2025, *MNRAS*, 537, 2535, doi: [10.1093/mnras/staf058](https://doi.org/10.1093/mnras/staf058)
- Claeysens, A., Adamo, A., Richard, J., et al. 2023, *MNRAS*, 520, 2180, doi: [10.1093/mnras/stac3791](https://doi.org/10.1093/mnras/stac3791)
- Coe, D., Zitrin, A., Carrasco, M., et al. 2013, *ApJ*, 762, 32, doi: [10.1088/0004-637X/762/1/32](https://doi.org/10.1088/0004-637X/762/1/32)

- Coe, D., Salmon, B., Bradač, M., et al. 2019, *ApJ*, 884, 85, doi: [10.3847/1538-4357/ab412b](https://doi.org/10.3847/1538-4357/ab412b)
- Collett, T. E., Buckley-Geer, E., Lin, H., et al. 2017, *ApJ*, 843, 148, doi: [10.3847/1538-4357/aa76e6](https://doi.org/10.3847/1538-4357/aa76e6)
- Di Gennaro, G., Brüggén, M., van Weeren, R. J., et al. 2023, *A&A*, 675, A51, doi: [10.1051/0004-6361/202345905](https://doi.org/10.1051/0004-6361/202345905)
- Diego, J. M., Broadhurst, T., Wong, J., et al. 2016, *MNRAS*, 459, 3447, doi: [10.1093/mnras/stw865](https://doi.org/10.1093/mnras/stw865)
- Diego, J. M., Protopapas, P., Sandvik, H. B., & Tegmark, M. 2005, *MNRAS*, 360, 477, doi: [10.1111/j.1365-2966.2005.09021.x](https://doi.org/10.1111/j.1365-2966.2005.09021.x)
- Diego, J. M., Tegmark, M., Protopapas, P., & Sandvik, H. B. 2007, *MNRAS*, 375, 958, doi: [10.1111/j.1365-2966.2007.11380.x](https://doi.org/10.1111/j.1365-2966.2007.11380.x)
- Diego, J. M., Pascale, M., Frye, B., et al. 2023a, *A&A*, 679, A159, doi: [10.1051/0004-6361/202345868](https://doi.org/10.1051/0004-6361/202345868)
- Diego, J. M., Meena, A. K., Adams, N. J., et al. 2023b, *A&A*, 672, A3, doi: [10.1051/0004-6361/202245238](https://doi.org/10.1051/0004-6361/202245238)
- Ebeling, H., Qi, J., & Richard, J. 2017, *MNRAS*, 471, 3305, doi: [10.1093/mnras/stx1636](https://doi.org/10.1093/mnras/stx1636)
- Ebeling, H., White, D. A., & Rangarajan, F. V. N. 2006, *MNRAS*, 368, 65, doi: [10.1111/j.1365-2966.2006.10135.x](https://doi.org/10.1111/j.1365-2966.2006.10135.x)
- Elíasdóttir, Á., Limousin, M., Richard, J., et al. 2007, arXiv e-prints, arXiv:0710.5636, doi: [10.48550/arXiv.0710.5636](https://doi.org/10.48550/arXiv.0710.5636)
- Forbes, D. A., & Romanowsky, A. J. 2023, *MNRAS*, 520, L58, doi: [10.1093/mnrasl/slac162](https://doi.org/10.1093/mnrasl/slac162)
- Fox, C., Mahler, G., Sharon, K., & Remolina González, J. D. 2022, *ApJ*, 928, 87, doi: [10.3847/1538-4357/ac5024](https://doi.org/10.3847/1538-4357/ac5024)
- Freeman, P. E., Kashyap, V., Rosner, R., & Lamb, D. Q. 2002, *ApJS*, 138, 185, doi: [10.1086/324017](https://doi.org/10.1086/324017)
- Fruscione, A., McDowell, J. C., Allen, G. E., et al. 2006, in *Society of Photo-Optical Instrumentation Engineers (SPIE) Conference Series*, Vol. 6270, Society of Photo-Optical Instrumentation Engineers (SPIE) Conference Series, ed. D. R. Silva & R. E. Doxsey, 62701V, doi: [10.1117/12.671760](https://doi.org/10.1117/12.671760)
- Furtak, L. J., Plat, A., Zitrin, A., et al. 2022, *MNRAS*, 516, 1373, doi: [10.1093/mnras/stac2169](https://doi.org/10.1093/mnras/stac2169)
- Furtak, L. J., Zitrin, A., Weaver, J. R., et al. 2023, *MNRAS*, 523, 4568, doi: [10.1093/mnras/stad1627](https://doi.org/10.1093/mnras/stad1627)
- Furtak, L. J., Zitrin, A., Richard, J., et al. 2024, *MNRAS*, 533, 2242, doi: [10.1093/mnras/stae1943](https://doi.org/10.1093/mnras/stae1943)
- Gladders, M. D., & Yee, H. K. C. 2000, *AJ*, 120, 2148, doi: [10.1086/301557](https://doi.org/10.1086/301557)
- Hilton, M., Sifón, C., Naess, S., et al. 2021, *ApJS*, 253, 3, doi: [10.3847/1538-4365/abd023](https://doi.org/10.3847/1538-4365/abd023)
- Hsu, L.-Y., Ebeling, H., & Richard, J. 2013, *MNRAS*, 429, 833, doi: [10.1093/mnras/sts379](https://doi.org/10.1093/mnras/sts379)
- Jauzac, M., Klein, B., Kneib, J.-P., et al. 2021, *MNRAS*, 508, 1206, doi: [10.1093/mnras/stab2270](https://doi.org/10.1093/mnras/stab2270)
- Jauzac, M., Richard, J., Jullo, E., et al. 2015, *MNRAS*, 452, 1437, doi: [10.1093/mnras/stv1402](https://doi.org/10.1093/mnras/stv1402)
- Johnson, B. D., Leja, J., Conroy, C., & Speagle, J. S. 2021, *ApJS*, 254, 22, doi: [10.3847/1538-4365/abef67](https://doi.org/10.3847/1538-4365/abef67)
- Johnson, T. L., & Sharon, K. 2016, *ApJ*, 832, 82, doi: [10.3847/0004-637X/832/1/82](https://doi.org/10.3847/0004-637X/832/1/82)
- Johnson, T. L., Sharon, K., Bayliss, M. B., et al. 2014, *ApJ*, 797, 48, doi: [10.1088/0004-637X/797/1/48](https://doi.org/10.1088/0004-637X/797/1/48)
- Jullo, E., Kneib, J. P., Limousin, M., et al. 2007, *New Journal of Physics*, 9, 447, doi: [10.1088/1367-2630/9/12/447](https://doi.org/10.1088/1367-2630/9/12/447)
- Kale, R., Shende, K. M., & Parekh, V. 2019, *MNRAS*, 486, L80, doi: [10.1093/mnrasl/slz061](https://doi.org/10.1093/mnrasl/slz061)
- Kelly, P. L., Rodney, S., Treu, T., et al. 2023, *Science*, 380, abh1322, doi: [10.1126/science.abh1322](https://doi.org/10.1126/science.abh1322)
- Khullar, G., Bayliss, M. B., Gladders, M. D., et al. 2022, *ApJ*, 934, 177, doi: [10.3847/1538-4357/ac7c0c](https://doi.org/10.3847/1538-4357/ac7c0c)
- Kneib, J.-P., & Natarajan, P. 2011, *A&A Rv*, 19, 47, doi: [10.1007/s00159-011-0047-3](https://doi.org/10.1007/s00159-011-0047-3)
- Ko, Y., Hwang, H. S., Lee, M. G., et al. 2017, *ApJ*, 835, 212, doi: [10.3847/1538-4357/835/2/212](https://doi.org/10.3847/1538-4357/835/2/212)
- Lahén, N., Naab, T., & Szécsi, D. 2024, *MNRAS*, 530, 645, doi: [10.1093/mnras/stae904](https://doi.org/10.1093/mnras/stae904)
- Laporte, N., Zitrin, A., Dole, H., et al. 2022, *A&A*, 667, L3, doi: [10.1051/0004-6361/202244719](https://doi.org/10.1051/0004-6361/202244719)
- Lee, M. G., Park, H. S., & Hwang, H. S. 2010, *Science*, 328, 334, doi: [10.1126/science.1186496](https://doi.org/10.1126/science.1186496)
- Limousin, M., Richard, J., Jullo, E., et al. 2016, *A&A*, 588, A99, doi: [10.1051/0004-6361/201527638](https://doi.org/10.1051/0004-6361/201527638)
- Lopez, S., Tejos, N., Ledoux, C., et al. 2018, *Nature*, 554, 493, doi: [10.1038/nature25436](https://doi.org/10.1038/nature25436)
- Lotz, J. M., Koekemoer, A., Coe, D., et al. 2017, *ApJ*, 837, 97, doi: [10.3847/1538-4357/837/1/97](https://doi.org/10.3847/1538-4357/837/1/97)
- Lucia, G. D., Fontanot, F., Hirschmann, M., & Xie, L. 2025, *Cosmic quenching*. <https://arxiv.org/abs/2502.01724>
- Madau, P., & Dickinson, M. 2014, *ARA&A*, 52, 415, doi: [10.1146/annurev-astro-081811-125615](https://doi.org/10.1146/annurev-astro-081811-125615)
- Mahler, G., Jauzac, M., Richard, J., et al. 2023, *ApJ*, 945, 49, doi: [10.3847/1538-4357/acaea9](https://doi.org/10.3847/1538-4357/acaea9)
- Mainali, R. 2019, PhD thesis, University of Arizona
- Martis, N. S., Sarrouh, G. T. E., Willott, C. J., et al. 2024, *ApJ*, 975, 76, doi: [10.3847/1538-4357/ad7735](https://doi.org/10.3847/1538-4357/ad7735)
- Meena, A. K., Zitrin, A., Jiménez-Teja, Y., et al. 2023, *ApJL*, 944, L6, doi: [10.3847/2041-8213/acb645](https://doi.org/10.3847/2041-8213/acb645)
- Meneghetti, M., Natarajan, P., Coe, D., et al. 2017, *MNRAS*, 472, 3177, doi: [10.1093/mnras/stx2064](https://doi.org/10.1093/mnras/stx2064)
- Montes, M., & Trujillo, I. 2022, *ApJL*, 940, L51, doi: [10.3847/2041-8213/ac98c5](https://doi.org/10.3847/2041-8213/ac98c5)
- Morishita, T., Roberts-Borsani, G., Treu, T., et al. 2023, *ApJL*, 947, L24, doi: [10.3847/2041-8213/acb99e](https://doi.org/10.3847/2041-8213/acb99e)



- Mowla, L., Iyer, K. G., Desprez, G., et al. 2022, *ApJL*, 937, L35, doi: [10.3847/2041-8213/ac90ca](https://doi.org/10.3847/2041-8213/ac90ca)
- Mowla, L., Iyer, K., Asada, Y., et al. 2024, arXiv e-prints, arXiv:2402.08696, doi: [10.48550/arXiv.2402.08696](https://doi.org/10.48550/arXiv.2402.08696)
- Natarajan, P., Williams, L. L. R., Bradač, M., et al. 2024, *SSRv*, 220, 19, doi: [10.1007/s11214-024-01051-8](https://doi.org/10.1007/s11214-024-01051-8)
- Natarajan, P., Chadayammuri, U., Jauzac, M., et al. 2017, *MNRAS*, 468, 1962, doi: [10.1093/mnras/stw3385](https://doi.org/10.1093/mnras/stw3385)
- Noirot, G., Desprez, G., Asada, Y., et al. 2023, *Monthly Notices of the Royal Astronomical Society*, 525, 1867–1884, doi: [10.1093/mnras/stad1019](https://doi.org/10.1093/mnras/stad1019)
- Pascale, M., Frye, B. L., Diego, J., et al. 2022, *ApJL*, 938, L6, doi: [10.3847/2041-8213/ac9316](https://doi.org/10.3847/2041-8213/ac9316)
- Pascale, M., Frye, B. L., Pierel, J. D. R., et al. 2024, arXiv e-prints, arXiv:2403.18902, doi: [10.48550/arXiv.2403.18902](https://doi.org/10.48550/arXiv.2403.18902)
- Pérez-González, P. G., Barro, G., Annunziatella, M., et al. 2023, *ApJL*, 946, L16, doi: [10.3847/2041-8213/acb3a5](https://doi.org/10.3847/2041-8213/acb3a5)
- Perivolaropoulos, L., & Skara, F. 2022, *NewAR*, 95, 101659, doi: [10.1016/j.newar.2022.101659](https://doi.org/10.1016/j.newar.2022.101659)
- Pfeffer, J., Forbes, D. A., Romanowsky, A. J., et al. 2025, *MNRAS*, 536, 1878, doi: [10.1093/mnras/stae2665](https://doi.org/10.1093/mnras/stae2665)
- Planck Collaboration, Ade, P. A. R., Aghanim, N., et al. 2016a, *A&A*, 594, A27, doi: [10.1051/0004-6361/201525823](https://doi.org/10.1051/0004-6361/201525823)
- . 2016b, *A&A*, 594, A27, doi: [10.1051/0004-6361/201525823](https://doi.org/10.1051/0004-6361/201525823)
- Planck Collaboration, Aghanim, N., Akrami, Y., et al. 2020, *A&A*, 641, A6, doi: [10.1051/0004-6361/201833910](https://doi.org/10.1051/0004-6361/201833910)
- Postman, M., Coe, D., Benítez, N., et al. 2012, *ApJS*, 199, 25, doi: [10.1088/0067-0049/199/2/25](https://doi.org/10.1088/0067-0049/199/2/25)
- Priewe, J., Williams, L. L. R., Liesenborgs, J., Coe, D., & Rodney, S. A. 2017, *MNRAS*, 465, 1030, doi: [10.1093/mnras/stw2785](https://doi.org/10.1093/mnras/stw2785)
- Remolina González, J. D., Sharon, K., & Mahler, G. 2018, *ApJ*, 863, 60, doi: [10.3847/1538-4357/aac8e](https://doi.org/10.3847/1538-4357/aac8e)
- Repp, A., & Ebeling, H. 2018, *MNRAS*, 479, 844, doi: [10.1093/mnras/sty1489](https://doi.org/10.1093/mnras/sty1489)
- Richard, J., Kneib, J.-P., Jullo, E., et al. 2007, *ApJ*, 662, 781, doi: [10.1086/517875](https://doi.org/10.1086/517875)
- Richard, J., Jauzac, M., Limousin, M., et al. 2014, *MNRAS*, 444, 268, doi: [10.1093/mnras/stu1395](https://doi.org/10.1093/mnras/stu1395)
- Richard, J., Claeysens, A., Lagattuta, D., et al. 2021, *A&A*, 646, A83, doi: [10.1051/0004-6361/202039462](https://doi.org/10.1051/0004-6361/202039462)
- Rigby, J. R., Johnson, T. L., Sharon, K., et al. 2017, *ApJ*, 843, 79, doi: [10.3847/1538-4357/aa775e](https://doi.org/10.3847/1538-4357/aa775e)
- Rigby, J. R., Vieira, J. D., Phadke, K. A., et al. 2023a, arXiv e-prints, arXiv:2312.10465, doi: [10.48550/arXiv.2312.10465](https://doi.org/10.48550/arXiv.2312.10465)
- . 2023b, arXiv e-prints, arXiv:2312.10465, doi: [10.48550/arXiv.2312.10465](https://doi.org/10.48550/arXiv.2312.10465)
- . 2025, *ApJ*, 978, 108, doi: [10.3847/1538-4357/ad7501](https://doi.org/10.3847/1538-4357/ad7501)
- Rihtaršič, G., Bradač, M., Desprez, G., et al. 2024, arXiv e-prints, arXiv:2406.10332, doi: [10.48550/arXiv.2406.10332](https://doi.org/10.48550/arXiv.2406.10332)
- Rivera-Thorsen, T. E., Chisholm, J., Welch, B., et al. 2024, *A&A*, 690, A269, doi: [10.1051/0004-6361/202450359](https://doi.org/10.1051/0004-6361/202450359)
- Salmon, B., Coe, D., Bradley, L., et al. 2018, *ApJL*, 864, L22, doi: [10.3847/2041-8213/aadc10](https://doi.org/10.3847/2041-8213/aadc10)
- Sendra, I., Diego, J. M., Broadhurst, T., & Lazkoz, R. 2014, *MNRAS*, 437, 2642, doi: [10.1093/mnras/stt2076](https://doi.org/10.1093/mnras/stt2076)
- Sharon, K., Gladders, M. D., Rigby, J. R., et al. 2012, *ApJ*, 746, 161, doi: [10.1088/0004-637X/746/2/161](https://doi.org/10.1088/0004-637X/746/2/161)
- Sharon, K., & Johnson, T. L. 2015, *ApJL*, 800, L26, doi: [10.1088/2041-8205/800/2/L26](https://doi.org/10.1088/2041-8205/800/2/L26)
- Sharon, K., Mahler, G., Rivera-Thorsen, T. E., et al. 2022, *ApJ*, 941, 203, doi: [10.3847/1538-4357/ac927a](https://doi.org/10.3847/1538-4357/ac927a)
- Umehata, H., Kubo, M., Smail, I., et al. 2025, arXiv e-prints, arXiv:2502.01868, doi: [10.48550/arXiv.2502.01868](https://doi.org/10.48550/arXiv.2502.01868)
- Weaver, J. R., Davidzon, I., Toft, S., et al. 2023, *A&A*, 677, A184, doi: [10.1051/0004-6361/202245581](https://doi.org/10.1051/0004-6361/202245581)
- Weinberg, D. H., Mortonson, M. J., Eisenstein, D. J., et al. 2013, *PhR*, 530, 87, doi: [10.1016/j.physrep.2013.05.001](https://doi.org/10.1016/j.physrep.2013.05.001)
- Wuyts, E., Rigby, J. R., Gladders, M. D., & Sharon, K. 2014, *ApJ*, 781, 61, doi: [10.1088/0004-637X/781/2/61](https://doi.org/10.1088/0004-637X/781/2/61)
- Zheng, W., Postman, M., Zitrin, A., et al. 2012, *Nature*, 489, 406, doi: [10.1038/nature11446](https://doi.org/10.1038/nature11446)
- Zheng, W., Shu, X., Moustakas, J., et al. 2014, *ApJ*, 795, 93, doi: [10.1088/0004-637X/795/1/93](https://doi.org/10.1088/0004-637X/795/1/93)
- Zitrin, A., Zheng, W., Broadhurst, T., et al. 2014, *ApJL*, 793, L12, doi: [10.1088/2041-8205/793/1/L12](https://doi.org/10.1088/2041-8205/793/1/L12)
- Zitrin, A., Fabris, A., Merten, J., et al. 2015, *ApJ*, 801, 44, doi: [10.1088/0004-637X/801/1/44](https://doi.org/10.1088/0004-637X/801/1/44)